Top quark pair production and calorimeter energy resolution studies at a future collider experiment

Katja Seidel

München 2012

Top quark pair production and calorimeter energy resolution studies at a future collider experiment

Katja Seidel

Dissertation
an der Fakultät für Physik
der Ludwig–Maximilians–Universität
München

vorgelegt von
Katja Seidel
aus Dinslaken

München, den 30. Januar 2012

Erstgutachter: Prof. Dr. Christian Kiesling

Zweitgutachter: Prof. Dr. Jochen Schieck

Tag der mündlichen Prüfung: 27. März 2012

Zusammenfassung

Diese Dissertation beschäftigt sich mit Detektorkonzepten, Daten- sowie Simulationsanalysen für Studien zu einem zukünftigen linearen Elektron-Positron-Beschleuniger. Um Präzisionsmessungen an solch einem Beschleuniger durchzuführen, hat die CALICE Kollaboration bildgebende Kalorimeter entwickelt, welche sich durch eine feine Granularität auszeichnen. CALICE hat Prototypen für elektromagnetische und hadronische Kalorimeter mit unterschiedlichen Technologien konstruiert und in verschiedenen Strahlzeiten am DESY, CERN und Fermilab erfolgreich getestet.

Zur Verbesserung der hadronischen Energieauflösung eines analog ausgelesenen hadronischen Kalorimeterprototypen wurden in dieser Arbeit drei Softwarekompensationtechniken entwickelt. Es handelt sich um eine lokale und zwei globale Softwarekompensationsmethoden, wobei eine der Methoden ein neuronales Netz zur Optimierung der Energierekonstruktion verwendet und zwei auf einer Gewichtungsmethode, abhängig von der Energiedichte, basieren. Gewichtungsfaktoren werden aus simulierten, sowie aus Teststrahldaten extrahiert und auf verschiedene Datensätze angewendet. Die hier entwickelten Methoden resultierten in einer Verbesserung der hadronischen Energieauflösung von 15 – 25 % im Vergleich zu einer Energierekonstruktion ohne Softwarekompensation.

Ob sich Softwarekompensationstechniken auch erfolgreich bei einem Detektor an einem linearen Elektron-Positron-Beschleuniger anwenden lassen, wird im zweiten Teil dieser Arbeit anhand von Simulationsstudien mit zwei verschiedenen Detektorkonzepten und der lokalen Gewichtungsmethode untersucht. Die Energieauflösungen für einzelne Hadronen sowie für Jets mit und ohne Softwarekompensation werden präsentiert.

Im dritten Teil dieser Dissertation wird eine Top-Quark-Paar-Simulationsstudie am geplanten CLIC Beschleuniger bei einer Schwerpunktsenergie von 500 GeV vorgestellt. Die Analyse basiert auf einer detaillierten Detektorsimulation. Zweiphotonen-Hintergrundprozesse sind realistisch miteinbezogen, so dass die Studie geeignet ist, die Möglichkeit von Präzisionstudien unter den gegebenen Bedingungen zu testen. Für eine integrierte Luminosität von 100 fb^{-1} und unter Betrachtung des Signals sowie von Standardmodell-Hintergrundprozessen wird die Top-Quark-Masse und Breite im voll-hadronischen und im halb-leptonischen Zerfallskanal bestimmt. Die Analyse erreicht als Ergebnis eine statistische Ungenauigkeit für die Top-Quark-Masse von 0.08 GeV im voll-hadronischen und 0.09 GeV im halb-leptonischen Zerfallskanal.

Abstract

This thesis is focused on detector concepts and analyses investigated at a future linear electron positron collider. For precision measurements at such a collider, the CALICE collaboration develops imaging calorimeters, which are characterized by a fine granularity. CALICE has constructed prototypes of several design options for electromagnetic and hadronic calorimeters and has successfully operated these detectors during combined test beam programs at DESY, CERN and Fermilab.

To improve the hadronic energy reconstruction and energy resolution of a hadron calorimeter prototype with analog readout three software compensation techniques are presented in this thesis, of which one is a local and two are global software compensation approaches. One method is based on a neural network to optimize the energy reconstruction, while two are energy weighting techniques, depending on the energy density. Weight factors are extracted from and applied to simulated and test beam data and result in an average energy resolution improvement of 15 – 25 % compared to a reconstruction without software compensation.

Whether such software compensation techniques are also applicable to a detector concept for a future linear electron positron collider is studied in the second part of this thesis. Simulated data, two different hadronic detector models and a local software compensation technique are used for this study. The energy resolutions for single hadrons and for jets are presented with and without software compensation.

In the third part of this thesis, a study on top quark pair production at a center-of-mass energy of 500 GeV at the proposed electron positron collider CLIC is presented. The analysis is based on full detector simulations, including realistic background contributions dominated by two photon processes. The mass and width of the top quark are studied in fully-hadronic and semi-leptonic decays of top quark pairs using event samples of signal and Standard Model background processes, corresponding to an integrated luminosity of $100\,\mathrm{fb}^{-1}$. Statistical uncertainties of the top mass of 0.08 GeV and 0.09 GeV are obtained for the fully-hadronic and the semi-leptonic channels, respectively.

Contents

Chapter 1

Introduction

The central question of particle physics today is how the Standard Model has to be extended or can be succeeded by a theory that explains open questions and possible new phenomena of past, current and future experiments.
The Standard Model has been the accepted theoretical model of high energy particle physics since the 1970s [1–3]. It is the model which describes the observed elementary particle spectra as well as three of the known existing fundamental forces: the electromagnetic, the weak and the strong force. The basis of the Standard Model are its fundamental particles: the quarks and leptons, of which all matter is built, and the gauge bosons, which are the mediator particles of the different forces. The Standard Model did not only explain the experimental observations at the time it was developed, it also predicted the existence of the W and Z bosons, the c, b and the t quarks and the ν_τ. Eventually all of these particles have been observed experimentally. Although the Standard Model is very successful, it has unresolved issues and flaws. These problems include predictions that have yet to be confirmed, failures to explain observed phenomena and overall fine-tuning or construction issues. In the following, examples for these shortcomings of the Standard Model are discussed.

The most prominent open question of the Standard Model is the existence of the Higgs boson, which is responsible for the so called electroweak symmetry breaking. It is not only a missing particle of the Standard Model, but it is the gauge boson which generates massless photons and massive W and Z bosons as well as the masses of all elementary particles. Electroweak symmetry breaking via the Higgs mechanism [4–8] in the Standard Model can shortly be described as follows: Electroweak symmetries are constructed by gauge field theory based on the $SU(2)_L \times U(1)_Y$ symmetry group. A complex scalar $SU(2)$ doublet, the Higgs doublet, couples to these gauge fields and renormalizable interactions are arranged such that the neutral component of the scalar doublet acquires a non-zero vacuum expectation value. Thus, the electroweak symmetry is broken and results in a physical real scalar field h, massive W and Z fields, and a massless photon [9]. The masses of the fermions are generated in a similar manner via electroweak symmetry breaking since the Higgs doublet is postulated to couple to the fermions through Yukawa interactions with couplings strengths proportional to the fermion masses. The underlying dynamics of the electroweak symmetry breaking, i.e. the reason for the Higgs potential shape, is not known in the Standard Model.
The electroweak symmetry breaking via the Higgs mechanism and the Higgs particle were predicted in 1964, but the existence of the particle has not yet been proven. The size of its

mass, like that of the elementary particles, is not postulated by the Standard Model. However, indirect experimental limits for the Higgs boson mass are obtained from precision measurements of electroweak parameters, since they depend logarithmically on the Higgs mass through radiative corrections. These measurements indicate that the Higgs boson mass[1] is lighter than approximately 250 GeV [9]. Other theoretical calculations predict the scale λ, at which new physics can occur, depending on the Standard Model Higgs mass. A lower limit of 70 GeV on its mass would require the Standard Model to be valid only up to 1 TeV. If its mass is between 130 GeV and 180 GeV the Standard model could be valid up to $\lambda = 10^{16}$ GeV. A Higgs mass above these limits could be explained by extensions of the Standard Model and would require new physics at the TeV scale. The Large Hadron Collider (LHC) [10] experiments ATLAS [11] and CMS [12] at CERN[2] have been specially designed and build to find the Higgs boson. It is currently well accepted that, if it exists, ATLAS or CMS must find it with sufficient data. If data taking continues with the current rate, it is expected to find or exclude the Standard Model Higgs until the end of 2012. However, even if the Higgs boson is found, the experiments at the LHC will not be able to determine all its quantum numbers. A different machine, a precision machine, would be necessary for that.

One of the problems of the Standard Model is its failure to explain Dark Matter. From measurements of the rotational speeds of galaxies and gravitational lensing of background objects by galaxy clusters, we know that Dark Matter exists. Only 5 % of the mass of our universe consists of atoms, 23 % is made of Dark Matter and 72 % of Dark Energy. The Standard Model does not include any particle that could account for Dark Matter. However, models beyond the Standard Model, like supersymmetry models (SUSY) [13], can provide an answer for Dark Matter. In SUSY models, all known elementary particles get superpartners, which have a spin that differs by 1/2 from that of their Standard Model partners. SUSY has to be a broken symmetry in order to separate the masses of the superpartners from the masses of the known elementary particle. The lightest supersymmetric particle in SUSY models can be constructed to be neutral and stable, and therefore would be a suitable candidate for Dark Matter [14, 15]. However, SUSY models are not the only models providing candidates for Dark Matter. The masses of candidates range from a 10^{-5} eV to 10^{-5} solar masses, depending on the model. One future task of particle and astroparticle physics is to pin down the correct model.
The Standard Model also does not explain the baryon asymmetry in our universe, since the size of CP-violation in weak interactions is not large enough. Ideas like electroweak baryogenesis in Minimal Super Symmetric Models [16, 17] or leptogenesis [18] try to address this open question.
Another indication for the existence of physics beyond the Standard Model is provided by neutrinos. The Standard Model predicts three types of neutrinos, which are massless in the

[1] Here and in the following $h = c = 1$ is used.
[2] Conseil Européenne pour la Recherche Nucléaire, Geneva, Switzerland

model. This assumption is valid in many cases so that precision calculations are not affected. However, since the discovery of neutrino oscillations in 1998 [19, 20], it is known that at least two of the three neutrino flavors have non-zero masses.

So far the missing piece as well as unresolved problems of the Standard Model have been discussed. Other, more theoretically driven issues are related to the fine-tuning problems in the Standard Model, which are often addressed by the "naturalness" problem. Naturalness in physics describes the common belief that all coefficients in a theory should be of order one [21]. In particle physics, this implies that all terms in the effective action which preserve required symmetries should appear with natural coefficients. Three parameters in the Standard Model do not follow naturalness. First, the non-existence of strong CP-violation, which is based on the very small, almost zero value of the angle θ in the QCD Lagrangian [22]. The angle θ is required to be $< 10^{-9}$, since a CP-violating term in QCD would contribute to a measurable neutron electric dipole moment, which has not been measured [23]. Secondly, the hierarchy problem [24–27] is another aspect of naturalness discrepancies. It addresses the fact that the weak force is 10^{32} times stronger than gravity or in other words, that the Higgs mass is so much lighter than the Planck mass. Calculations of loop corrections to the Higgs mass lead to quadratic divergences. The Higgs mass would be computed to the largest scale in which the Standard Model is still valid of $\mathcal{O}(10^{16}\,\text{GeV})$. On the other hand, it is expected that the physical Higgs boson mass is less than 1 TeV, since otherwise the WW scattering cross section would violate unitarity. This discrepancy is renormalized away in the theory, but due to the scale of this fine-tuning, it is not believed to be an accident. The third aspect is the size of the cosmological constant [28]. It is an open question why the zero-point energy of the vacuum cannot be interpreted as cosmological constant. Quantum field theory predicts the cosmological constant to be of the order of the fourth power of the Planck mass but measurements indicate a value that is a factor 10^{120} smaller [29].

Physicists hope that new models or extensions to the Standard Model can provide explanations for the described shortcomings of the Standard Model. A very natural extension of the Standard Model is, as already mentioned, supersymmetry. Besides the prediction of a possible candidate for a Dark Matter particle, SUSY models can explain Higgs masses up to 1 TeV, with a natural mechanism for electroweak symmetry breaking. Furthermore, they can solve the hierarchy problem, since a supersymmetry relating fermions and bosons enables the cancellation of divergences in loop corrections to the Higgs mass. SUSY models can also lead to a unification of the weak, strong, and electromagnetic forces at a scale around 10^{16} GeV. SUSY is not the only possible extension of the Standard Model. Physicists have to bear in mind that an obvious answer or model at a certain time might be a suitable solution, only until new phenomena might be found and shed a different light on Nature. Thus, other theories like extra dimensions [30] or string theory [31] are studied as well. Future experiments and experimental data will hopefully help to reveal suitable theories.

Besides direct searches for new physics, like Dark Matter and SUSY particle searches, physicists have another possibility to test the Standard Model and indirectly search for physics beyond the Standard Model, namely precision measurements. In the past, precision measurements mostly focused on the weak gauge bosons and on flavor physics. Higher accelerator energies and detailed theoretical calculations make it possible to also study the top quark properties with high precision.

The existence of a third quark generation, consisting of the bottom and the top quark, was postulated in 1973 by M. Kobayashi and T. Maskawa to explain the observed CP-violations in kaon decays [32]. The top quark was discovered in 1995 by the CDF [33] and the DØ [34] experiments at Fermilab and with the start of the LHC, it was also found by the ATLAS [35] and CMS [36] experiments. The top quark is unique compared to the other quarks of the Standard Model because of its very large mass and, consequently, of its short lifetime. Its lifetime, which the Standard Model predicts to be 5×10^{-25} s, is shorter than the timescale of the strong interaction. Hence, the top quark does not form bound states (hadrons). Instead, the properties of a single quark can be studied. Confinement prohibits this for the lighter quarks. The top quark decays via the weak force almost exclusively into a W boson and a b quark, the weak isospin partner of the top quark.

The large value of the top quark mass results in a large coupling between the top quark and the Higgs boson and is furthermore important for flavor physics. Therefore, it is a very useful tool to test the Standard Model and possible Standard Model extensions. In many extensions to the Standard Model in which the Higgs boson mass can be calculated, the theoretical prediction for the Higgs mass depends sensitively on the top mass [37]. Therefore, if a Higgs would be found at the LHC, its nature could be additionally probed by the top quark Yukawa coupling.

At the Tevatron [38] and LHC, top quark mass measurements are done by comparing experimental data with generated Monte-Carlo distributions, with a precision of $\delta m_t \sim$1-2 GeV. Using this determination, the Monte Carlo top mass parameter is measured or, from a theoretical point of view, the peak position of the pole mass. This generated top mass does not have a sensible meaning in theory. In the description of QCD different mass definitions are used, depending on the chosen renormalization scheme. The relation between the experimental and theoretical QCD scale is not known. However, two different techniques are proposed to determine or measure the top mass used in theory. Both methods require a special experimental environment, which would be feasible at a future high energy e^+e^- collider. One technique proposes a mass scan around the top pair production threshold [39, 40]. For such scans, it must be possible to adjust the beam energy precisely and change it in small steps. Another possibility involves new theoretical developments [41], which make factorization predictions of the top invariant mass in e^+e^--annihilation for centre-of-mass energies much larger than the top pair production threshold. Here perturbation theory and a non-perturbative distribution function, which is extracted from massless quark initiated event-shape distributions, such as thrust, allows the determination of the top quark mass. The advantage of such a method is that

it is not restricted to a certain energy range. Both methods, the extraction of the top mass using a threshold scan and from event shapes, claim that a top mass precision of $\delta m_t < 100\,\mathrm{MeV}$ can be reached.
Once the top mass and the Higgs mass are measured with an adequate accuracy, it would be useful to determine the value of the effective leptonic weak mixing angle $\sin^2\theta^l_{\mathrm{eff}}$ and the W boson mass. These variables provide an extremely sensitive probe of quantum effects of new physics [42] and therefore, they study the consistency of a model in an unambiguous way. Also, the precise knowledge of the strong coupling constant α_S is desirable. Currently, its error is on the percent level, which is worse than for the electromagnetic and weak couplings. A higher accuracy on α_S would help to determine the possible scale of grand unification [43].

Nowadays, particle physics is driven by the LHC and its collider experiments ATLAS and CMS. The data, which is currently being collected, helps to test the predictions of the Standard Model of particle physics but also to search for hints of physics beyond the Standard Model. In case new physics is discovered at the LHC, a lepton-lepton collider would help to provide precision measurements of this physics. The reasons for this are: The usage of elementary particles as collision partners gives reduced theoretical uncertainties in order to perform precision measurements. A much smaller range in production cross sections allows higher sensitivity to weakly interacting particles and therefore might even lead to new discoveries. The energy regime of such a collider will be specified by the LHC results.
The most advanced future collider projects are linear e^+e^--colliders, which are discussed in this thesis. The reason for building a linear e^+e^--collider, the status of other lepton colliders and the two options for a linear e^+e^--collider, namely ILC and CLIC, together with their detector concepts, are described in Chapter 2. Since CLIC and ILC differ from each other in energy reach, the physics potentials at the different center-of-mass energies are also reviewed in Chapter 2.
The detector concepts of both ILC and CLIC are based on typical high energy 4π detectors, with tracking and calorimeter sections. Parts of this thesis focus on one sub-detector of the detector concepts, the hadronic calorimeter. Therefore, a recap on the interactions of different particles with matter and the basics of calorimetry are given in Chapter 3.
The CAlorimeter for a future LInear Collider Experiment (CALICE) collaboration investigates imaging calorimeters optimized for the ILC and CLIC detector concepts. This thesis focuses on one prototype of a hadronic calorimeter proposed by CALICE. In Chapter 4 details about the detector layout, detector calibration, event reconstruction as well as simulation are given. The data which is presented in this thesis, was taken with the calorimeter prototype at CERN in 2007. The setup, run and event selections for the following analysis on pion data is explained. The main goal of a calorimeter is the energy measurement, which can be improved using software compensation techniques. Such techniques, namely local and global software compensation techniques, have been developed for the hadronic prototype detector. The motivation for these techniques, their implementation details, and their results for test

beam and simulated data, are also presented in Chapter 4.
Such methods can, in principle, also be applied to the 4π detectors of ILC or CLIC. A proof of principle for the success of such a technique in a large scale environment is given in Chapter 5. In a first part the simulation study investigates, whether software compensation is feasible in the different hadronic calorimeters of ILC and CLIC. The second part shows the energy resolution improvement for single hadrons and jets in the hadronic calorimeter of ILC.
As explained, the top quark is an important tool for future precision tests in particle physics. To study the ability to do precision measurements is mandatory at such a future machine like ILC and CLIC. Besides the explained theory driven top mass measurements from threshold scans and event shape variables, at first stage a kinematic top mass measurements would be performed. The top mass determination in such a physics analysis with the CLIC collider is presented in Chapter 6. Chapter 7 gives a summary of this thesis and discusses the outlook for future work in this field.

Chapter 2

A Future Linear Collider

A precision machine, as explained in the previous chapter, is needed beyond the LHC in high energy particle physics studies. The required energy range for such a machine needs to be higher than 200 GeV, the maximum energy reached by the last e^+e^--machine, LEP [44]. How much higher will depend strongly on the results of the LHC.
The LHC is a discovery machine, which uses protons, and thus sub-structured particles, to collide. It is a discovery machine since very high energies and collision rates can be reached, but the presence of high QCD background, due to the use of sub-structured protons, is a drawback. The actually wanted physics interaction at a collision of two protons is the one of two quarks, two elementary particles. Therefore, it is widely believed that a future precision machine would use elementary particles for collisions, namely leptons. Furthermore, it has been seen in the past that complementary measurements of hadron-hadron and lepton-lepton colliders provide a much bigger insight into the open questions of particle physics. For example, the W and Z bosons were discovered at the proton-antiporton synchrotron SPS, but precise measurements of their masses and couplings were done at the electron-positron collider LEP.
From the acceleration point of view it would be best to use a ring accelerator, because a circular accelerator has many advantages compared to a linear one. The particles are accelerated during many circulations, thus the accelerator structure is used multiple times per particle and the requirements on the acceleration gradient are easier to realize. Furthermore, since during each collision only a very small fraction of particles actually interact with each other, the other particles can be focused again and used for further collisions, reaching a higher collision rate.
However, acceleration of particles in a ring is limited by two factors: synchrotron radiation and magnet strength. The currently strongest bending magnets in an accelerator, the superconducting dipole magnets of the LHC, reach a field strength of 8.36 T. The superconducting materials limit the maximum achievable magnetic field strength. Thus, Research and Development (R&D) programs take place to reach much higher field strength (>20 TeV) [45].
Bending charged particles in a magnetic field causes synchrotron radiation. The energy loss ΔE per cycle due to this radiation depends mainly on the particle mass m_0 and particle energy E:

$$\Delta E = \frac{(Ze)^2 \cdot E^4}{\varepsilon_0 \cdot 3R \cdot (m_0 c^2)^4}, \tag{2.1}$$

where Ze is the charge of the accelerated particle, ε_0 is the electric field constant and R is the radius of the circle. Thus, from the point of view of acceleration to very high energies, out of the three lepton generations, the use of the heaviest lepton would be favorable, because they could be accelerated in a ring, like protons.
The heaviest lepton is the τ lepton, with a mass of 1777 MeV. But the τ lepton is difficult to produce and with its short lifetime of only $2.9{\cdot}10^{-13}$ s, it decays too fast for acceleration. Also, the muon mass of 106 MeV would be large enough for a circular particle acceleration. Present ideas of a muon collider [46,47] face very challenging issues, like the required fast production, acceleration and collision of muons, again due to their short lifetime ($\tau_\mu = 2.2{\cdot}10^{-6}$ s). The proof of principle for this concept does not exist yet.
This leaves the lightest charged lepton, the electron. The electron is, not only since LEP, a very suitable acceleration particle. It does not decay, but its small mass of 0.51 MeV requires the use of a linear acceleration. If higher collision energies than at LEP are to be achieved the electron would loose, in a circular acceleration, too much energy due to bremsstrahlung radiation. Linear acceleration of particles to energies close to the TeV range requires very long acceleration paths, which correlates with the costs of a project, or very high acceleration gradients. The latter solution is investigated by plasma wakefield acceleration, which aims for acceleration gradients of 10 – 100 GV/m. It is studied by a number of groups [48], but to show the feasibility of such a project many years of R&D work are necessary in the future. Therefore, only a linear e^+e^- collider, with a rather long acceleration path, can be used for a high energy particle physics collider in the near future.

2.1 Physics potential

The physics potential of a future linear collider will, of course, depend on its center-of-mass energy. The different accelerator options, described in Section 2.2, focus mainly on the center-of-mass energies of 3 TeV and 500 GeV, therefore slight distinctions will be made for the discussion of the physics potential of the two regimes.
One main project will be precise Higgs physics. Depending on the mass range in which the Higgs will be found by the LHC, the possible analyses are different. Currently the exclusion limits of LEP, Tevatron and LHC require a Higgs mass between 115 – 128 GeV or above 525 GeV [49, 50]. At a center-of-mass energy of 500 GeV and for a mass less than 400 GeV a Standard Model Higgs can be measured in a model independent way with the golden channel $e^+e^- \to (Z^*) \to ZH \to l^+l^-X$, from the Higgs recoil of the Z boson. The other main production channels are: WW fusion ($e^+e^- \to WW \to \nu\nu H$) and ZZ fusion ($e^+e^- \to ZZ \to e^+e^-H$). For a higher center-of-mass energy, the cross sections of this production channels change and a Higgs mass can also be measured, at a suitable collider, via associated production with top quarks ($e^+e^- \to t\bar{t}H$) and via the double Higgs production channels Higgsstrahlung $e^+e^- \to HHZ$ and fusion $e^+e^- \to \nu\nu HH$. These processes, besides having a lower cross section, give the additional advantage of the possibility to measure the

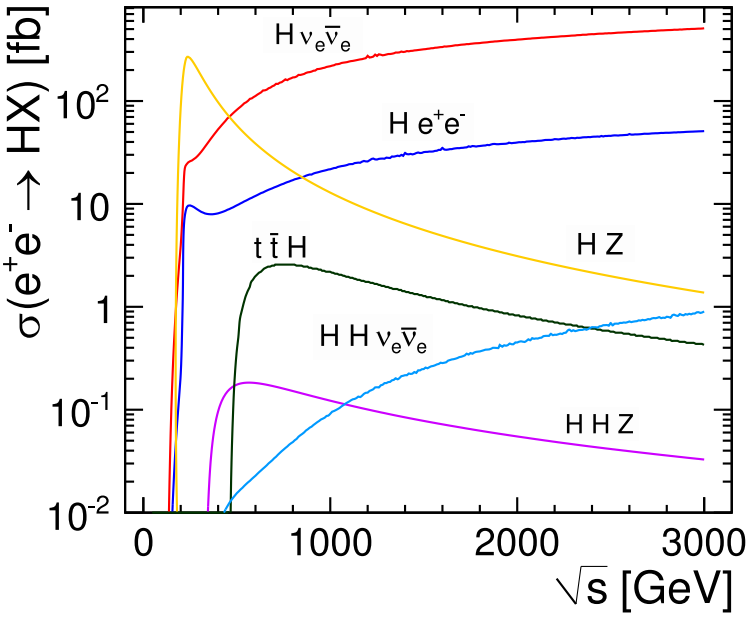

Figure 2.1: SM-Higgs production cross sections as a function of the center-of-mass energy for a Higgs mass of 120 GeV. Figure taken from [51].

Higgs Yukawa and self-couplings. The cross sections of Standard Model Higgs production for a 500 GeV and 3 TeV center-of-mass machine are shown in Figure 2.1.
If a Higgs bosons is found, and it is not the Standard Model Higgs boson, namely for example one Higgs boson of a SUSY theory or a composite bound state of new strongly interacting dynamics at the TeV scale, then it is even more necessary to measure its production mechanisms and couplings.
Precision measurements of the Standard Model are in general of big interest at $\sqrt{s}$ =500 GeV. In particular top quark measurements (mass, width, forward-backward asymmetry), already discussed in the first chapter of this thesis, or the measurement of the effective leptonic weak mixing angle $\sin^2\theta^l_{\text{eff}}$ and the W boson mass can be used to test more precisely their quantum corrections and the consistency of the model. The possibility of threshold scans, specially for the top mass production, provides a strong mechanism to test theoretical mass scales.
The main interest, though, will be precision measurements of physics beyond the Standard Model. For example, virtual effects of physics beyond the Standard Model can be probed, if the LHC measured a Z' boson that is predicted in many Standard Model extensions. A lepton-lepton collider would be sensitive to it and could measure its couplings and distinguish between theory models with much higher precision. Or, if a SUSY particle exists at the weak scale the most adequate theoretical SUSY model has to be found. The LHC can

easily discover SUSY particles at that scale, but heavy sleptons, neutralinos and charginos can only be produced copiously at the LHC through decay chains of strongly interacting supersymmetric particles. In some cases, these chains do not access all states, which would be of great help to find the most precise SUSY model. A lepton-lepton collider in the TeV range can very efficiently investigate that region, looking for any new particles with electroweak charges. To reveal the full theory of SUSY, it is necessary to measure accurately the complete sparticle spectrum, just as the measurements of the Higgs boson properties are necessary to complete the SM. This means that all the masses, mixing angles, couplings, spins, etc., of the new particles will have to be determined.

2.2 Accelerator

Two accelerator options with different energy ranges are currently under investigation: The International Linear Collider (ILC) with a design center-of-mass energy of $\sqrt{s}$ =500 GeV and a possible upgrade to 1 TeV and the Compact LInear Collider (CLIC) with $\sqrt{s}$ =3 TeV, which would be built in staged approach, starting around $\sqrt{s}$ =500 GeV. A CLIC machine at $\sqrt{s}$ =500 GeV is able to measure the same physics as the ILC. One example of the feasibility of a $\sqrt{s}$ =500 GeV CLIC machine is the top analysis, presented in this thesis in Chapter 6. However, if it is decided that the main answers to the present questions in particle physics can be answered with a machine at $\sqrt{s}$ <1 TeV, it is most likely that the ILC will be build, because it is based on well known and stable acceleration techniques. The main reason to built CLIC is the high energy option. At $\sqrt{s}$ =3 TeV, particle energies even higher than in present measurements at LHC can be studied. In the following, the two acceleration concepts for the low and the high energy option are introduced.

2.2.1 International Linear Collider

The low energy concept with a design energy of $\sqrt{s}$ =500 GeV and a peak luminosity of $2 \cdot 10^{34}\,\mathrm{cm}^{-2}\mathrm{s}^{-1}$ is called ILC. The layout of the accelerator is shown in Figure 2.2.
Polarized electrons are produced by the illumination of photocathodes by two drive laser beams in a DC gun. The electron bunch train is created and accelerated over several stages before it is injected into the superconducting booster linac for the acceleration to 5 GeV. Afterwards, the electron beam travels through a 6.7 km long damping ring, whose main purpose is to reduce the beam emittance. Additionally, the beam is accelerated from 5 GeV to 15 GeV. The final acceleration to an energy of 250 GeV, over a distance of 12 km, is done in the main linac.
At an energy of 150 GeV, the electron beam is used to produce the positron beam in an undulator-based source, which is a periodic structure of dipole magnets. Electrons traversing this undulator are forced to undergo oscillations and thus, emit polarized photons of an energy of ∼10 MeV. The polarized photons are focused on a thin titanium foil to produce polarized

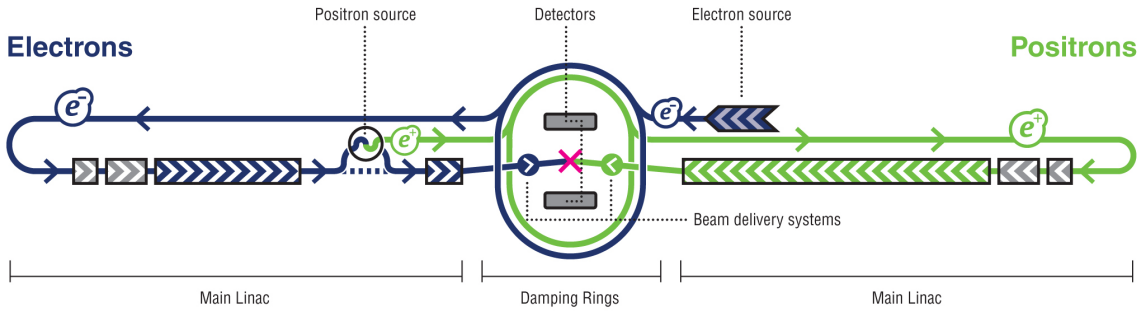

Figure 2.2: Layout of the International Linear Collider (ILC).

positrons by pair production. Further positron acceleration happens analog to the electron acceleration in a second damping ring and main linac.
Before colliding with a crossing angle of 14 mrad, which is needed to reduce beam induced backgrounds at the interaction point, the beams are transported by a 4.5 km long beam delivering system from the main linac to the interaction point.
The key element of the accelerator are the two main linacs with their 1.3 GHz superconducting radio-frequency accelerating cavities, which are operated at a gradient of 31.5 MV/m. The total length of the accelerator is about 31 km.
Physics runs are possible for every energy above $\sqrt{s}$ =200 GeV and calibration runs with limited luminosity are possible at $\sqrt{s}$ =91 GeV. In order to perform mass and spin measurement via threshold scans, the beam energy can be changed in small steps. The electron beam should have a polarization higher than 80 % and the positron beam should have an upgradable polarization of up to 50 %.
The design beam parameters would give approximately 2600 bunches per pulse with a length of $\sim$ 1.6 ms at a pulse rate of 5.0 Hz. Design and technology of the ILC are advanced and ready to be build [52].

2.2.2 Compact LInear Collider

The Compact Linear Collider is the high energy option of an e^+e^--collider and would be operated at a nominal center-of-mass energy of 3 TeV. In the CLIC design, the electrons and positrons have to be accelerated from 9 GeV to 1.5 TeV in one pass. To achieve this goal in a cost efficient and realistic way, an accelerating gradient of 100 MV/m has to be reached. For this gradient, wave structures have to be produced, which propagate at room temperature with a frequency of about 12 GHz. Superconducting accelerating cavities are not applicable for this, due to their intrinsic maximum field limitation. To avoid the use of an immense number of individual radio frequency power sources (klystrons), the accelerator design uses a two beam structure shown in Figure 2.3.
The two beams are called drive beam and main beam. The beam power of the drive beam,

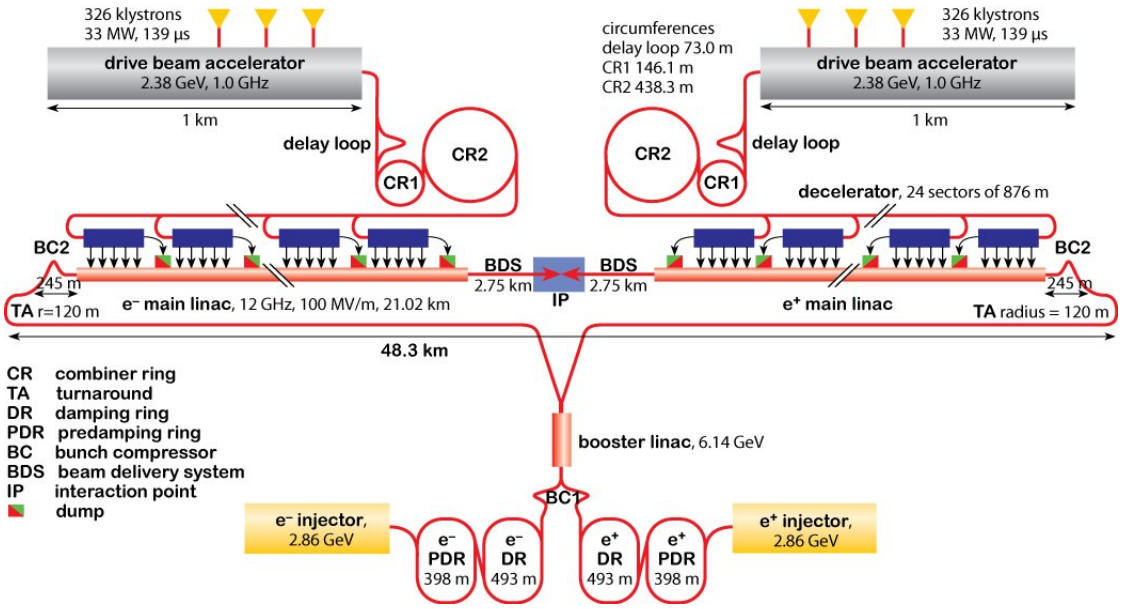

Figure 2.3: Layout of the Compact LInear Collider (CLIC). Figure taken from [51].

which runs parallel to the main beam, is extracted and converted to radio frequency power in radio frequency devices called PETS (Power Extraction and Transfer Structure) and is then transported to the acceleration structure of the main beam. The drive beam runs at a relatively low energy of 2.37 GeV, but with a high peak current of 100 A. Both beams are placed in a single tunnel. Specific parameters for the CLIC accelerator, listed in Table 2.1, are a trade-off between costs and the requirement of a high radio frequency and a high luminosity. For example, short bunches are favored by the radio frequency efficiency, but a bunch separation of 0.5 ns is challenging for the detector design and event reconstruction, see Section 2.3 to 2.5.

It should be noted that the feasibility of the novel CLIC scheme and technology, i.e. the realization of a large part the critical parameters required, was demonstrated in the CLIC Test Facility [51], but a lot of issues, for example concerning power consumption, cost and stability, have to the solved before a multi-TeV linear collider based on the CLIC technology can be envisaged.

2.3 Detector Concepts for a Linear Collider

Detectors for ILC and CLIC have to account for the accelerator specifications, such as radiation and beam related background discussed in more detail in Section 2.4, and have to be optimized to reach the performance requirements of the physics goals. The golden Standard Model Higgs production channel, shown in Section 2.1, can be measured most precisely

Table 2.1: Main parameters of ILC and CLIC. Beam parameters for ILC are based on the ILC Reference Design Report published in 2007 [53]. For CLIC the numbers are based on the Conceptual Design Report to be published in 2012 [51].

Accelerator	ILC	CLIC	CLIC
Center-of-mass energy	500 GeV	500 GeV	3 TeV
Total (Peak 1 %) luminosity ($cm^{-2}s^{-1}$)	$2.0(1.5)\cdot10^{34}$	$2.3(1.4)\cdot10^{34}$	$5.9(2.0)\cdot10^{34}$
Total side length (km)	31	13.0	48.3
Accel. gradient (MV/m)	31.5	80	100
Bunch separation (ns)	369	0.5	
Repetition rate (Hz)	5	50	
Beam pulse duration (ns)	1000	177	156
Bunch charge ($10^9 e^{+/-}$)	20	6.8	3.72
Total power consumption (MW)	230	240	560

in case of the Z decaying into muons. An excellent muon resolution is therefore necessary. Precise flavor tagging for the identification and separation of b and c bosons requires a tracking resolution better than $\sigma_{p_T/p_T^2} \sim 3\cdot10^{-5}\,\mathrm{GeV}^{-1}$. Many precision measurements involve multi jet final states. For such analyses it is necessary to separate W and Z bosons. Figure 2.7 shows that this goal can be achieved with a jet energy resolution which is around 3 %. In case of CLIC, the track momentum and the jet energy resolution also need to have this precision, since other analysis techniques, like beam energy constraints, cannot be used.
Both the ILC and the CLIC accelerator design contain only one interaction region, where the two beams collide. To have two independent experiments, it is planned that two detector systems share the same interaction region. They would operate in a push-pull scenario, i.e. they can be exchanged and therefore would share beam time in regular intervals. Two detector concepts for the ILC exist, namely the Silicon Detector (SiD) and the International Large Detector (ILD). The detector concepts are designed for particle flow reconstruction, see Section 2.5, and are therefore designed to fulfill the particle flow requirements of excellent efficiency and track resolution of the tracking detectors, and high granularity of the calorimeter system. SiD is a compact detector with its main tracking detector entirely made out of silicon. The ILD detector concept is a larger system with a time projection chamber (TPC) used as the main tracking device. Both detector concepts were first designed and optimized for the ILC. In 2009, their Letters of Intent [54, 55] were validated by an international review committee. The detector concepts for CLIC use the ILC detector designs as a baseline. Some changes had to be made in order to adjust for the CLIC conditions, like high beam energy and high beam background. The CLIC_ILD detector concept is described in more detail in the following Subsection 2.3.1, since the physics analysis, described in Chapter 6, was done with the CLIC_ILD detector. The main differences between the ILD detector design of ILC and CLIC

involve the radius of the innermost vertex detector layer, the choice of absorber material for the hadronic calorimeter, the design of the detector in the forward region and the capability of time-stamping.

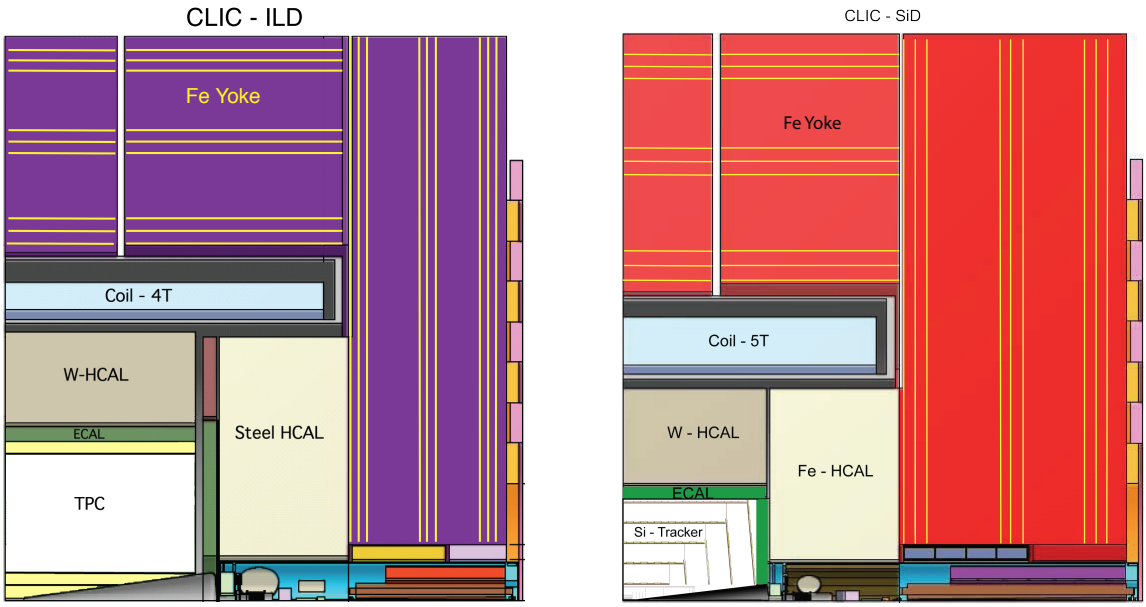

Figure 2.4: Layout of the CLIC_ILD and CLIC_SiD detector concepts. Figures taken from [51].

2.3.1 International Large Detector for CLIC (CLIC_ILD)

In this subsection, the main sub-detectors of the CLIC_ILD detector concept are described, starting with the detector closest to the interaction point. More details can be found in [51].

Tracking

- **Vertex Detectors** The vertex detector is the innermost part of the tracking system. The purpose of the tracking system is to measure three-dimensional space points of positions along the particles' paths. All sub-detectors are placed in a magnetic field, charged particles are therefore deflected according to the Lorentz force. The momentum of charged particles is measured by the curvature of their tracks. With an inner radius of 31 mm, the vertex detector is closest to the interaction point and will mainly be used to measure vertices of long lived particles like b and c hadrons. The detector design consists of three double layers arranged in a barrel configuration. The goal is to reach a single point resolution of 2.8 µm.

- **Time Projection Chamber** The TPC is the main tracker of the ILD tracking system. Its barrel design covers a large volume (inner radius 329 mm, outer radius 2248 mm, length 2248 mm), in which tracks can be measured with a large number of three-dimensional space points.

- **Silicon Tracking** Supplementary to the silicon vertex detector, silicon detector layers outside the TPC are necessary for precise timing information. The silicon detector is designed out of silicon strip sensors. It covers the forward region down to very small angles (7 °) and the region between vertex detector and TPC.

The main purpose and challenge of the CLIC_ILD TPC is the track separation in high energy jets and the ability of event identification in 150 ns in a collection of 300 bunch crossings, which can only be reached with the timing and additional position information of the vertex detector and the outer silicon tracking layer.

Calorimeter System

- **Electromagnetic Calorimeter** The electromagnetic calorimeter is a sampling calorimeter based on 30 active silicon layers and tungsten absorber plates. The total radiation length sums up to $24\,X_0$. Tungsten was chosen as an absorber material (radiation length X_0 =3.5 mm, Molière radius R_M=9 mm, hadronic interaction length λ_I =99 mm) to reach a compact design and a better separation of nearby electromagnetic showers compared to lead, because of the smaller Molière radius. For the first 20 layers, the absorber thickness is chosen to be 2.1 mm, while for the last ten layers, it will be 4.1 mm. For the active layers different sensor concepts exist like silicon pads or silicon strips coupled to photon sensors. For the simulation model of CLIC_ILD silicon pads with a transverse granularity of 5.1×5.1 cm^2 were chosen.

- **Hadronic Calorimeter** The analog hadronic calorimeter of CLIC_ILD is a sampling calorimeter, which uses a tungsten alloy as absorber material in the barrel and will have a total thickness of $7.5\,\lambda$. The tungsten alloy is non-magnetic and can therefore be installed inside the magnetic field of the experiment. Due to its high density, high energetic hadronic showers should typically be absorbed in the calorimeter system. As in the case of the electromagnetic calorimeter the final design of the active layers is not decided yet. Different technologies are under discussion, for example an analog calorimeter of scintillator tiles with Silicon-Photomultiplier (SiPM) readout or gaseous resistive plate chamber (RPC) detectors with digital or semi-digital readout as well as gaseous (Micromegas and GEM) detectors. In the following, only the analog option will be presented, since it was chosen for the simulation model of CLIC_ILD.
  The transverse segmentation of the hadronic calorimeters reaches a fine granularity due to the use of scintillator cells of 3×3 cm^2 in case of the analog option. Longitudinally, the barrel is segmented into 77 layers. Each absorber layer has a thickness of 1 cm and

is followed by an 6.5 mm thick active layer of scintillator tiles and readout electronics. The light of the scintillator is either mediated via a wavelength shifting fiber to a SiPM or is read out via direct coupling to a SiPM, with a special tile shape [56]. For the endcap, the absorber material is changed to steel. The advantage of using steel is the faster shower development of hadron showers and the lower cost.

Magnet System

- **Solenoid** A strong magnetic field is necessary to bend charged particles along their path and therefore to measure their momenta. Furthermore a magnetic field in the calorimeter systems helps for the particle identification in the reconstruction using particle flow, which is described in Section 2.5. Thus all described detector components around the interaction point are overlaid with a magnetic field, which is created by a superconducting coil and will have a strength of 4 T. The final design of the solenoid is not decided yet.

- **Magnet Yoke and Muon Chambers** An iron yoke will be used to return the magnetic flux. Further studies have to be done to finally decide on the iron thickness, which depends on mechanical stability requirements of the magnetic field and on the tolerable fringe field of the detector concept.
  The iron will be instrumented with either glass RPCs or scintillators, to enhance the muon identification capability of the detector and to be used as a tail catcher for hadronic showers developing late in the calorimeters. In total, nine layers of iron with different radii will be used as muon chambers.

Very Forward Region Detectors

- These detectors are called **LumiCal** and **BeamCal**. They cover the very forward region close to the beam pipes and therefore have to be extremely radiation hard. The LumiCal is positioned around the outgoing beam pipe and its purpose is to measure the luminosity with an accuracy better than 10^{-3}, by Bhabba scattering. In front of the final focusing magnet the BeamCal is placed to give a fast luminosity estimate by beamstrahlung radiation measurements. Both LumiCal and BeamCal are cylindrical electromagnetic detectors and need to handle several MGy of radiation dose a year.

2.4 Machine Background

2.4.1 Background at ILC

Machine induced backgrounds were studied for the ILC detector designs. Electron-positron pairs from beamstrahlung were identified as the largest source of relevant background. The

rate and the energies of these background particles were found to be uncritical for most sub-detectors. However the vertex detector is affected by background. To have an affordable hit rate in the sensitive layers of the vertex detector the position of its inner radius is determined to 16 mm in the ILD design at $\sqrt{s}$ =500 GeV.

2.4.2 Background at CLIC

The background levels at CLIC play a major role for the design of the different sub-detectors, the event reconstruction and physics reach of the machine. The reasons for the critical background conditions, compared to the ILC, are the higher bunch energy at CLIC, the high bunch charge density and the small bunch-to-bunch spacing inside of one bunch train.
The reason for the bunch design is to obtain a high luminosity, for which the bunches have to be focused at the interaction point to a high charge density. The small beam size leads to photon radiation of the electrons and positrons inside the electromagnetic field of the other beam and therefore to a beam energy loss.

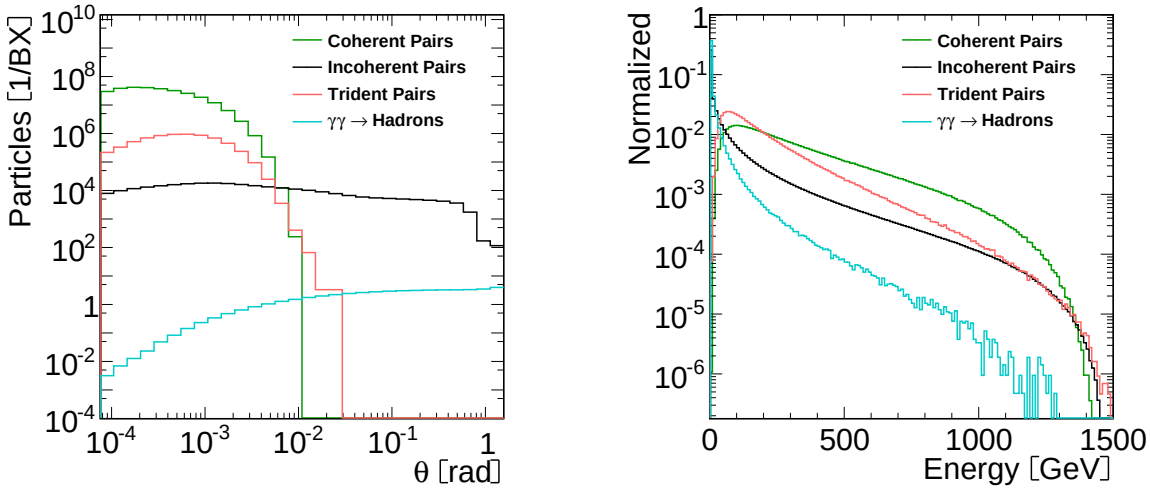

Figure 2.5: The distributions of the beam related backgrounds: (*left*) Fraction of energies for the particles of each background source. (*right*) Angular distributions of the produced background particles. Both plots are for CLIC at $\sqrt{s}$ =3 TeV. Figures taken from [51].

Beam related backgrounds at CLIC consist mostly of coherent and incoherent e^+e^--pairs and $\gamma\gamma \rightarrow$ hadron pairs. Coherent e^+e^--pairs are produced by the interaction of real beamstrahlung photons with the electromagnetic field of the opposite beam. Since most of these pairs are produced with very small beam angles, see Figure 2.5, they affect only the design of the area close to the interaction point. A beam exit line with a 10 mrad opening hole was designed in a way that most of the coherent pairs disappear in the beampipe, along with the outgoing

beams. The incoherent e^+e^--pairs on the other hand, created by the interaction of real and virtual photons with individual particles of the other beam, can be produced with much larger angles, see Figure 2.5. This drives the design of the forward region and the vertex detector. A major redesign of the forward region compared to the ILD design of ILC was performed, described in detail in [57]. The position of the innermost layer of the vertex detector had to be increased to 25 mm for 500 GeV and to 31 mm for 3 TeV at CLIC_ILD.
Another background source are the two-photon interactions. Real or virtual photons of the colliding beams can produce hadronic final states. The number and visible energy of these $\gamma\gamma \rightarrow$ hadron events is shown in Figure 2.6 for $\sqrt{s}$ =500 GeV and $\sqrt{s}$ =3 TeV. Since these particles can also be created with large angles, see Figure 2.5, they account for the main background in the calorimeters and central trackers.
The bunch-to-bunch spacing at CLIC is chosen to be 0.5 ns long. The value has to be small, since the breakdown rate of the fields inside the cavities increases for longer times between two bunches in a bunch train. This leads to the inevitable situation that the detectors have to integrate over several bunches during the data taking. To separate off-line hits of different bunch crossings and physics from background, a fast readout of all detector elements and time stamping capabilities for an excellent time resolution are necessary.

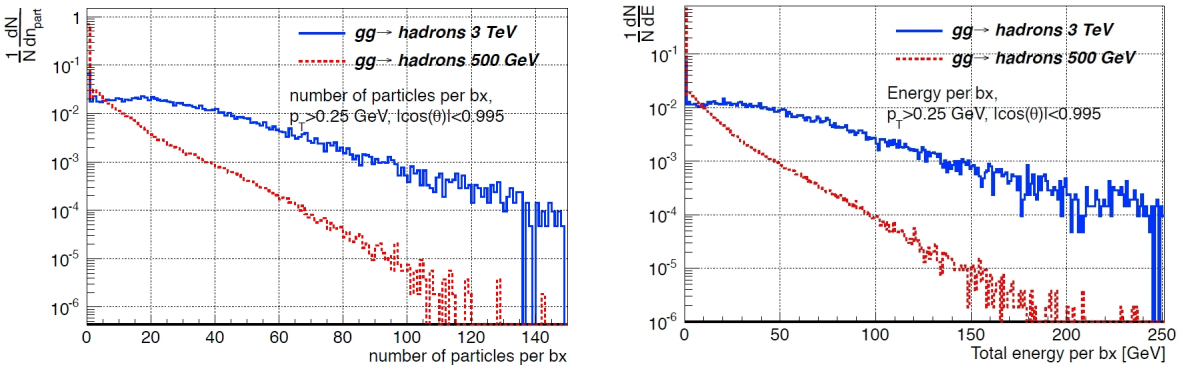

Figure 2.6: Number of particles (*left*) and visible energy (*right*) for the beam induced background through $\gamma\gamma \rightarrow$ hadrons at 3 TeV and 500 GeV at CLIC. Figures taken from [51].

2.5 Event Reconstruction

2.5.1 Particle Flow

Particle Flow is a reconstruction method to reach high jet energy resolution. The method used for the future linear collider is PandoraPFA [58], which aims for a jet energy resolution of roughly 3 %. In a typical event, approximately 60 % of the jet energy is carried by

charged particles, 27 % is carried by photons, 10 % by neutral hadrons and the rest by neutrinos. The charged particles are mainly hadrons, thus, their energy is measured with the calorimeter system in the traditional jet energy reconstruction approach. However, since a typical calorimeter resolution is around $55\,\%/\sqrt{E}$, clearly PandoraPFA has to use new techniques to gain the required jet energy resolution.
PandoraPFA is based on algorithms which reconstruct the four-vectors of all produced particles in each event. The energy of each particle is measured with the sub-detectors that give the best energy estimate for a given particle type. Hence, the momenta of all charged particles are measured with the tracking detectors. Together with particle identification, this yields the energy of the reconstructed particle. Photons energies are measured in the electromagnetic calorimeter and the energy of neutral hadrons is measured in the hadronic calorimeter. Like this, only 10 % of the jet energy is measured with the hadronic calorimeter. For a perfect particle identification, an energy resolution better than the required 3 % could be achieved. In practice, though, a perfect cluster and track to particle matching cannot be reached. Thus, it is essential for the particle flow algorithm to correctly distinguish between nearby clusters or tracks of two particles. For example, if parts of a cluster in the hadronic calorimeter are not associated with the correct track in the tracking system, the cluster part in the hadronic calorimeter will be classified as a cluster of a neutral particle. Up to twice of this particles' energy is then added twofold to the event and the so-called confusion is increased. If all sub-detectors have a high spatial resolution, the confusion can be minimized. Hence, the tracking system needs to have very high spatial resolution and the calorimeters need very high granularity. For this reason, they are often called imaging calorimeters.
The PandoraPFA jet energy resolution composition is summarized in Figure 2.7, which shows the pure calorimetric energy resolution (blue dot-dashed line), the contribution of confusion (black dotted line) and the resulting jet energy resolution using PandoraPFA (black solid line), compared to the traditional jet energy reconstruction approach (red dashed line). More details about the particle flow framework and algorithms of PandoraPFA can be found in the Appendix B.1.

2.5.2 Timestamping

As described in Section 2.4, the beam induced background energies and rates are high at a CLIC collider. Therefore, the event reconstruction does not only include the particle flow techniques but also requires a background suppression. The background suppression is applied after the particle flow event reconstruction to use information of the particle flow reconstruction. It is based on a combination of timing and p_{T} cuts. Timing cuts alone cannot be applied with a significant strength, since the propagation time of the particles, especially in hadronic showers, is large and the energy release due to nuclear processes is not finished on a time scale of a few ns. For example, in a time window of 6 ns 90 % of the energy of a hadronic shower is released in the steel end-cap of the CLIC detector, but only 82 % of

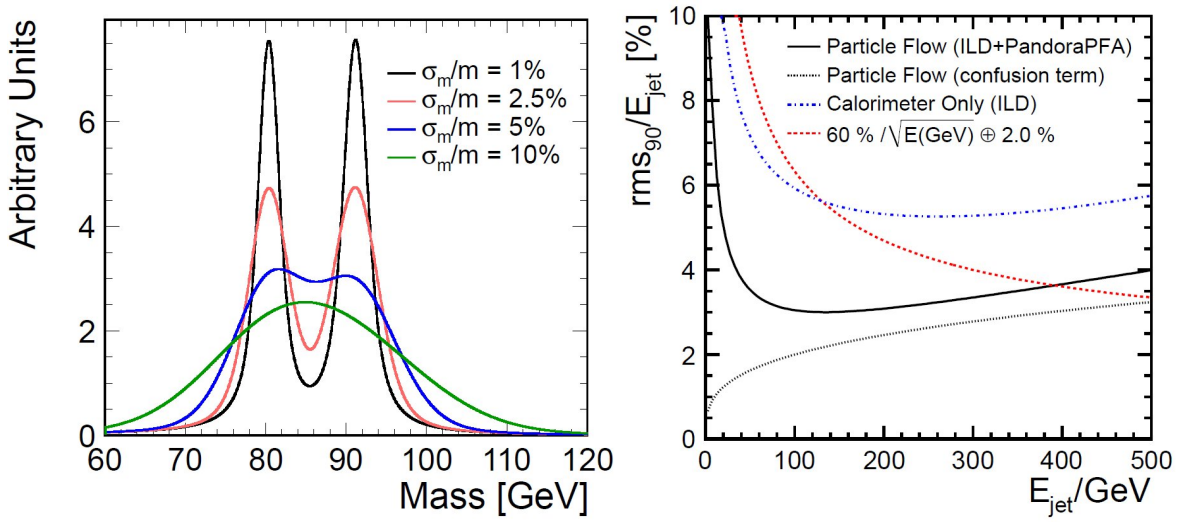

Figure 2.7: (*left*) Ideal W/Z separation versus jet mass resolution obtained using a Gaussian smearing of Breit-Wigner distributions. Figure taken from [51]. (*right*) The jet energy resolution components of the calorimeter (blue dot-dashed line), the confusion term (black dotted line) for ILD, resulting in the PandoraPFA jet energy resolution (solid black line) compared to the traditional jet energy reconstruction approach (red dashed line). Figure taken from [58].

the energy can be detected in a time window of 25 ns in the tungsten barrel [51]. Since the produced particles of the most dominant background process of $\gamma\gamma \rightarrow$ hadrons, mostly have low p_{T}, this variable is used in addition for background suppression.
The selection strategy is as follows: It is assumed that the entire bunch train of data is available for off-line reconstruction. Inside one bunch train, candidates for a hard interaction would be identified and the data in a window around this time would be passed to the event reconstruction. This window differs for the sub-detectors: 10 ns for the silicon detectors, the electromagnetic and the hadronic calorimeter endcap, 100 ns for the hadronic calorimeter barrel, reflecting the slower hadronic shower time development, and the entire bunch train for the CLIC_ILD TPC. In the event simulation, background events of $\gamma\gamma \rightarrow$ hadrons processes are overlaid on the physics events and the full track and particle flow reconstruction is performed on all hits in the above time windows. Timing and p_{T} cuts are then applied to the reconstructed particles. Tighter timing cuts are used at the reconstructed cluster level, where the cluster times are calculated as the truncated energy weighted mean of the hit times, allowing further background reduction. Tracks associated to out-of-time clusters are rejected. In this way an effective time window of the order of 2.5 ns can be used to reject the $\gamma\gamma \rightarrow$ hadrons background events. The effect of the background rejection cuts is shown in Figure 2.8 for an event at 3 TeV.

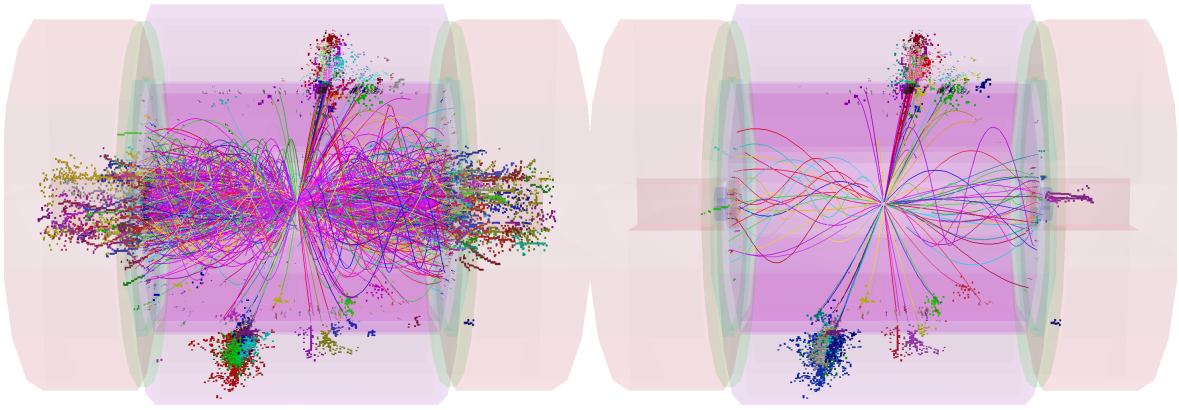

Figure 2.8: Reconstructed particles in a simulated $e^+e \to H^+H \to t\bar{b}\bar{t}$b event at 3 TeV in the CLIC_ILD detector concept with background from $\gamma\gamma \to$ hadrons overlaid (*left*). The effect of applying tight timing cuts on the reconstructed cluster times (*right*). Figure taken from [51].

Chapter 3

Calorimetry

In this chapter, an overview of the physical effects relevant for calorimetry in high energy particle physics is given. Furthermore, some characteristics of sampling calorimeters as well as the necessary details for the further discussion of simulations of hadronic showers are presented.

3.1 Energy loss of particles in matter

Particles which traverse matter lose energy due to interactions with the atoms of the absorber material. A particle with sufficiently high energy will create secondary particles or eventually a cascade of particles. The form of the energy loss depends on the incident particle, as well as on the material properties. A short summary of the energy loss processes of different particles is presented in the following. It is collected from [59–61], where more details can be found.

Energy loss of charged particles Charged particles, with a moderately relativistic energy, lose energy mainly due to ionization and atomic excitation. The energy loss $-\mathrm{d}E/\mathrm{d}x$ is described by the Bethe-Bloch equation:

$$-\left\langle \frac{\mathrm{d}E}{\mathrm{d}x} \right\rangle = Kz^2 \frac{Z}{A} \frac{1}{\beta^2} \left(\frac{1}{2} \cdot \ln \left(\frac{2m_e c^2 \beta^2 \gamma^2 T_{\max}}{I^2} \right) - \beta^2 - \frac{\delta(\beta\gamma)}{2} \right), \tag{3.1}$$

where $K = e\pi N_A r_e^2 m_e c^2$ with the classical electron radius $r_e = e^2/4\pi\varepsilon m_e c^2$, m_e the electron mass, N_A the Avogadro constant, z the charge of the incident particle, Z and A the atomic number and atomic mass of the material, $T_{\max}$ the maximum kinetic energy which can be transferred to a free electron in a single collision, I the mean excitation energy and $\delta(\beta\gamma)$ the density effect correction.
For electrons and positrons, the energy loss due to ionization and excitation is only valid in a very small energetic range around a few MeV. The dominant energy loss processes for electrons and positrons are described below.
In the region $0.1 \lesssim \beta\gamma \lesssim 1000$, the so-called Bethe range shown in Figure 3.1, the accuracy of the equation, is a few percent. For lower energies, the particle energy gets comparable to the bound electron energy levels of the atoms and thus, shell corrections become important. Above this range, radiative effects dominate. In the Bethe range the position of the minimum energy loss due to ionization can be found. Particles which lose this minimal amount of

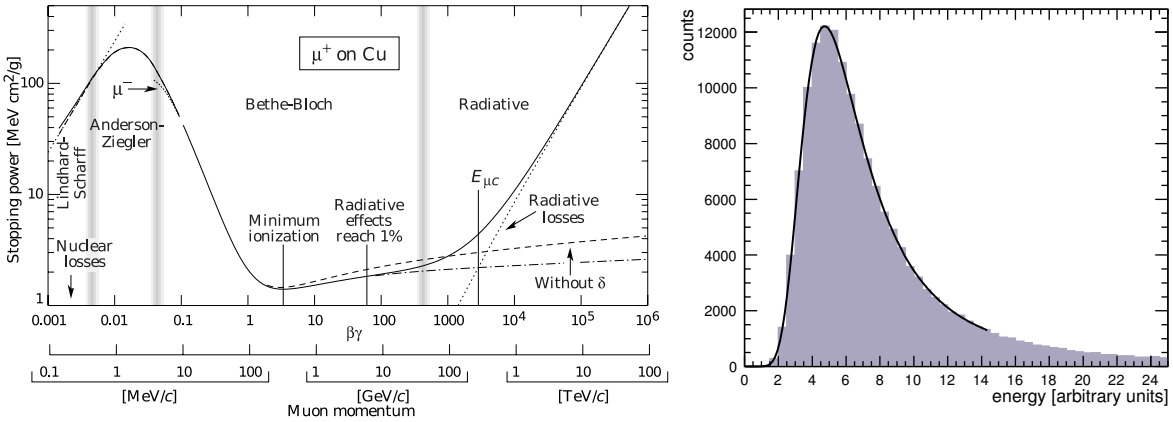

Figure 3.1: (*left*) Stopping power for positive muons in copper. Figure taken from [61]. (*right*) Landau distribution, describing the energy loss of MIPs.

energy, 1 – 2 MeV·cm^2/g in typical materials, are called minimum ionizing particles (MIP). A muon is called a MIP for energies between 80 MeV and 100 GeV.
In thin materials, the measured energy loss distribution reaches a maximum at smaller values than the mean energy loss and has a long tail towards high energy losses. The reasons are the small number of collisions and the large differences in energy loss per collision. The distribution of the energy loss of a minimum ionizing particle is described by a Landau distribution and is shown in Figure 3.1 on the right. The maximum of the distribution is the most probable value (MPV) of the energy loss. Calorimeter can be seen as a thin amount of material for muons above 1 GeV, since the distribution becomes Gaussian-like only for matter with thicknesses larger than 100 m water equivalent.

Photon interactions with matter Three processes lead to an interaction or total absorption of photons: the photoelectric effect, Compton scattering and pair production. The cross sections of these processes versus the photon energy are shown on the left of Figure 3.2 for a lead absorber. For photons of energies below 1 MeV, the photoeffect, i.e. the absorption of a photon by an atomic electron and the following ejection of this electron from the atom, has the highest cross section. For energies less than the electron mass, Thomson scattering contributes as well. With increasing energy, between 1 – 10 MeV, Compton and Rayleigh scattering become prominent. Thomson and Rayleigh scattering are processes in which no energy is transferred from the photons. The atoms gets neither ionized nor excited, only the photon direction changes. These two scattering processes do not contribute to the processes for the photon energy loss. For Compton scattering though, the photon loses energy. The photon is scattered on a free[1] electron, which recoils and is ejected from the atom. At even

[1] If the photon energy is high enough the bound electron can be approximated by a free particle.

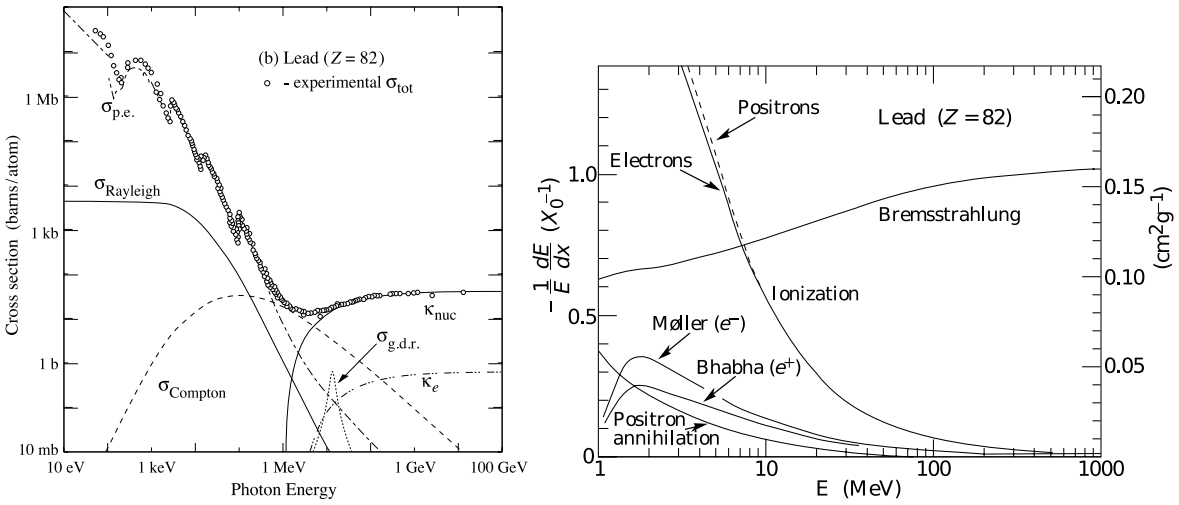

Figure 3.2: (*left*) Cross section of photon interaction processes versus the photon energy for lead. (*right*) Electron energy loss due to the relevant interaction processes versus the electron energy for lead. Figures taken from [61].

higher energies (threshold at $2 \cdot m_e$) the production of e^+e^--pairs, in the field of a nucleus, is the only significant process. The cross section of pair production is nearly energy independent for photon energies above 1 GeV.

Electron and positron interactions with matter Because of their small mass, electrons and positrons do not lose their energy like other charged particles. Their energy loss is due to ionization and bremsstrahlung. At low energies and up to approximately 10 MeV, ionization is the dominant process. Other processes, like Møller (e^-e^-) scattering, Bhabba (e^+e^-) scattering or positron annihilation, contribute as well. For higher energies, bremsstrahlung is the dominant process, in which the electron is scattered in the electric field of a nucleus and emits a photon. The cross sections of these processes versus the electron energy are shown on the right of Figure 3.2 for a lead absorber.

3.2 Electromagnetic showers

High energetic electrons, positrons and photons, above their critical energy[2], generate an electromagnetic cascade due to the production of secondary particles, via multiple successive bremsstrahlung and pair production processes in an absorber. The number of produced particles is roughly proportional to the incident particle energy. The electromagnetic shower development in an absorber material depends on the radiation length X_0. The radiation length

[2]Typically between 5-150 GeV for solids, $E_c = 610\,\text{MeV}/(Z + 1.24)$.

depends on the atomic number and the atomic mass of the absorber material, shown in Equation 3.2, and characterizes the distance after which the incident particle energy E_0 is reduced to E_0/e by bremsstrahlung:

$$X_0\left(\frac{\mathrm{g}}{\mathrm{cm}^2}\right) = \frac{716.4\,\mathrm{g}\cdot\mathrm{cm}^{-2}\mathrm{A}}{Z\cdot(Z+1)\cdot\ln\left(\frac{287}{\sqrt{Z}}\right)}. \tag{3.2}$$

Since the longitudinal shower development is primarily driven by the high energy part of the electromagnetic cascade, the electromagnetic shower length scales with the radiation length of the absorber material.

3.3 Hadronic showers

Hadronic showers are more complex than electromagnetic ones because of the additional dominant hadronic interaction. A schematic picture of a hadronic shower is shown in Figure 3.3. On the basis of this picture, the main properties of hadronic showers are described

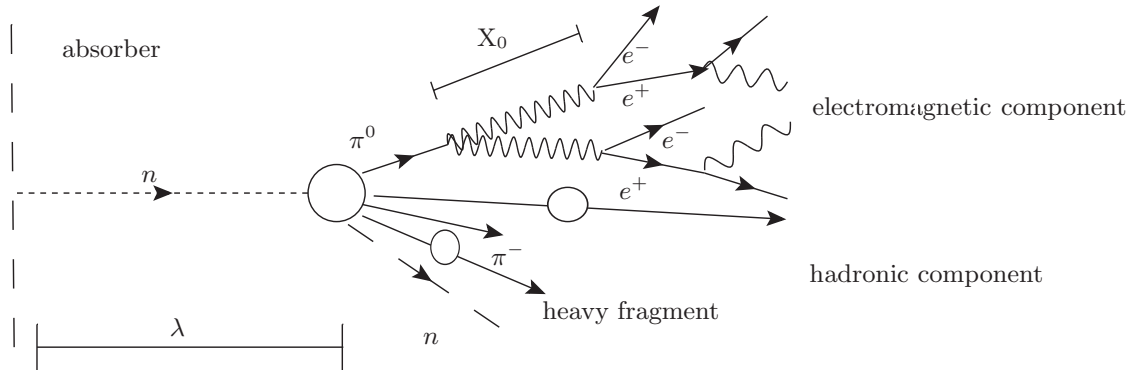

Figure 3.3: Schematic of a hadronic shower showing the electromagnetic and hadronic components.

in the following: A hadron traversing a medium undergoes a strong interaction typically after an interaction length λ_I. The nuclear interaction length λ_I leads to the probability P that a hadronic particle traverses a medium by a distance x without causing a nuclear interaction,

$$P = \exp\left(\frac{-x}{\lambda_I}\right). \tag{3.3}$$

During a nuclear interaction, the hadron interacts with the material nuclei. The nucleus can be broken, lose a number of neutrons and protons and end up in a highly excited state.

The incoming hadron may turn into a number of new hadrons, which are called secondary hadrons. These secondaries are mostly pions, due to their small mass and light quark content. Depending on the type of produced hadrons, an electromagnetic or a hadronic component of the hadronic shower is formed.

Electromagnetic component Mostly, neutral pions, but also for example ηs, form the electromagnetic component of a hadronic shower due to their electromagnetic decay. Neutral pions decay with a branching ratio of 99 % almost immediately into two photons. These photons interact further via pair production, Compton scattering or photoeffect, depending on their energy. If the electromagnetic particles carry enough energy, they trigger an electromagnetic cascade, as described in the previous paragraph. Since the radiation length of a material, which describes the electromagnetic cascade, is mostly shorter than the nuclear interaction length, the electromagnetic shower is typically a narrow, dense shower in the core of the full hadronic shower. The energy of a neutral pion, which starts the electromagnetic component of a hadronic shower, is completely transferred to the electromagnetic component and thus, cannot contribute at any further point to the hadronic component.

Hadronic component The hadronic component is described by the created particles, which do not take part in the electromagnetic component and the nuclei, taken part in the strong interaction. Secondarily produced charged hadrons can lose their energy via ionization or excitation or can undergo nuclear interactions themselves. In a strong interaction, spallation protons and neutrons as well as evaporation neutrons are produced and the nuclei are recoiled into highly excited states. Photons, from the prompt de-excitation of these highly excited states and charged secondaries, produce detectable ionization. However, recoiling nuclei mostly generate too little energy to be detected. Produced neutrons lose their energy in elastic collisions over hundreds of ns, thermalize and are captured with the production of more photons. The emission of these photons is also often hundreds of ns after the primary strong interaction of the incoming hadron. These processes (spallation, nuclear recoil, late neutron capture) lead to the fact that parts of the energy of a hadronic shower are undetectable and are therefore called ”invisible”.

Hadronic shower properties The nuclear interaction length scales with to the mass number of the material as $A^{1/3}$. Furthermore, the cross section of an interaction depends on the projectile size. Therefore, the cross section of pions is approximately 20 % smaller than the one of protons.
The number of produced secondary hadrons depends on the atomic mass of the material and is on average 5 – 10 for typical absorbers. Since the strong interaction is charge independent, the fraction of produced neutral pions is around 1/3, assuming only pions are created. This fraction represents also the average fraction of the electromagnetic component for the first strong interaction. However, since secondary produced hadrons of the hadronic component

can themselves undergo strong interactions and produce more neutral pions, the average electromagnetic component increases with increasing particle energy. In a simple model, the energy E of a hadron, which creates a hadronic shower, is shared between the electromagnetic fraction f_{em} and the hadronic fraction f_{had}: $E = f_{\text{em}} \cdot E + f_{\text{had}} \cdot E$. Because of the undetectable or invisible part in the hadronic component, the visible energy is less than the energy of the incoming hadron $E_{\text{vis}} < E$.
Hadronic showers show more qualitative differences for protons and pions. Protons and neutrons are baryons, meaning that the baryon number is conserved. Therefore, in every hadronic interaction a secondary baryon is produced, which is typically the leading secondary particle. This reduces the fraction of energy which can be used for the production of neutral pions. Hence, proton induced hadronic showers have a smaller electromagnetic fraction. This leads to a smaller signal measurable in the detector but also less fluctuations of invisible energy and a better resolution compared to pion induced hadronic showers.

3.4 Sampling calorimeters

Calorimeters are designed to measure the energy of an electromagnetic or a hadronic shower by its complete absorption and sometimes measure also the shape and direction of the shower. Two types of calorimeters exist, namely homogeneous calorimeters and sampling calorimeters.
Homogeneous calorimeters are made out of active material only, which has the advantage that all measurable energy can be detected, in principle. In order to achieve a complete energy loss of the incoming particle, calorimeters have to have a high density. Table 3.1 shows the density, radiation and interaction length of the active material with the highest density, $PbWO_4$, and of the two passive materials, iron and tungsten. For electromagnetic calorimeters, which typically have to have a total radiation length of $30\,X_0$, the choice of $PbWO_4$ can be suitable. Instead, for a hadronic calorimeter, its interaction length is usually too high to construct a calorimeter with an affordable depth. Typically, a total interaction length of $5 - 8\,\lambda_I$ is needed in high energy particle physics.

Table 3.1: Radiation and interaction lengths for lead tungstate, iron and tungsten.

Material	Density	X_0	λ_I	λ_I/X_0
$PbWO_4$	8.3 g/cm^3	0.89 cm	19.5 cm	21.9
Iron	7.87 g/cm^3	1.76 cm	16.77 cm	9.5
Tungsten	19.3 g/cm^3	0.35 cm	9.95 cm	28.4

Sampling calorimeters are built out of a multitude of successive active and passive layers. Particles lose their energy mainly in the passive materials. For electromagnetic calorimeters, high Z materials, whereas for hadron calorimeters metallic absorbers are preferred. The

energy measurement takes place in the active material, typically made out of ionizing gases or liquids, scintillators or semiconductors. Hence, only a fraction of the total absorbed energy is deposited in the active layers. The sampling fraction characterizes this sharing of deposited energy and is defined as the ratio of the energy deposited in the active and passive layers.
The electromagnetic shower development is a stochastic process, therefore, the energy resolution can be derived from statistical arguments. The measured energy depends on the number of produced ionization particles N. According to Poisson statistics, the variance σ^2 is equal to this number N, which leads to $\sigma(E) \propto \sqrt{N} \propto \sqrt{E}$ where E is the energy of the incident particle. The relative standard deviation gives the stochastic term of energy resolution σ/E:

$$\frac{\sigma}{E} \propto \frac{a}{\sqrt{E}}. \tag{3.4}$$

Additional terms are needed to describe the energy resolution of a realistic calorimeter. Electronic noise of the readout chain may influence the energy measurement. This term behaves as $\mathcal{O}(1/E)$. Finally, a constant term c is present, which results in detector imperfections such as dead material or cell non-uniformities. The different terms add up quadratically to the final description of energy resolution of a sampling calorimeter:

$$\frac{\sigma}{E} = \frac{a}{\sqrt{E}} \oplus \frac{b}{E} \oplus c. \tag{3.5}$$

There are other effects which may influence the energy measurement. Lateral and longitudinal leakage of a shower for a calorimeter with fixed width and length grows on average logarithmically and will result in a distorted detector response and reduced resolution at higher energies. Also, temperature gradients in the detector or radiation damage can affect the energy measurement. Some of these effects can be corrected by the calibration or by dedicated software techniques. The energy measurement of hadronic showers can be described by Equation 3.5, too, with additional effects due to the higher complexity of hadronic showers.
As explained in the paragraph about hadronic showers, hadronic showers have an electromagnetic and a hadronic component. Due to the invisible energy of the hadronic component, the measured energy is less than the incoming particle energy. The relation $e/h \neq 1$ represents the fact that the detector response to a non-electromagnetic component h and an electromagnetic component e of the same energy is not equal. The e/h ratio can never be measured in practice, therefore, addressing compensation, one often refers to the e/π ratio. This ratio describes the detector response of an electron and a pion of the same energy. Since the electromagnetic fraction in a hadronic shower (of the pion) increases with increasing particle energy, the factor e/π is energy dependent and approaches unity for high energies.
Most calorimeters are non-compensating and in particular show $e/\pi > 1$, although $e/\pi < 1$ was measured for some calorimeters. Especially homogeneous calorimeters are intrinsically non-compensating, since the energy, for example used for nuclear breakup, can never be measured. For sampling calorimeter, a wider range of e/π ratios exist. There are even those

which have a ratio very close to one, which are then called self-compensating, like the ZEUS calorimeter [62]. The self-compensating character of the ZEUS calorimeter was achieved due to its constructed sampling fraction, from plates of depleted uranium interleaved with plastic scintillator as active material. The ratio of thicknesses of active to passive layers was chosen to reach self-compensation. Part of the energy of an electromagnetic shower released in the uranium absorber is unseen since the electrons, positrons and photons are completely absorbed without secondary visible effects. In the case of a hadronic shower, charged pions and protons induce uranium fission with the consequent production of nuclear fragments and neutrons. A fraction of these secondaries exits the uranium absorber and interacts elastically with protons in the scintillator, producing visible energy. This mechanism achieves that part of the energy lost by a hadronic shower in the absorber, is recovered via uranium fission. A further contribution came from photons, which were produced in the de-excitation of nuclear fragments of the uranium fission.
Non-compensation seriously degrades the detector linearity and energy resolution. Methods to compensate this behavior address either the hardware, like in the case of the ZEUS calorimeter, or the off-line reconstruction, often called software compensation. Software compensation techniques try to identify the electromagnetic and hadronic component in the event reconstruction and apply different weighting factors to the components to equalize them and reach $e/\pi = 1$. Different techniques for software compensation are described in Chapter 4.

3.5 Simulation of Hadronic Showers

The difficulties in the description of hadronic showers, as explained in Section 3.3, influence the simulation of hadronic showers. The theoretical problem is to describe a multi-particle object, a hadron, interacting with another multi-particle object, a nucleus of the detector material. Simulations in high energy particle physics are mostly performed using Geant4 [63, 64], a toolkit for the simulation of the passage of particles through matter. Different models, so-called physics lists, exists in Geant4 to describe the hadronic cascades in hadronic showers.
All physics lists use the same model to simulate electromagnetic showers, due to its well understood description. The hadronic shower description of the models differs and can be experimentally or theoretically driven. For the hadronic sector, the physics lists are mostly combinations of different models [65], since models only describe interactions well within a limited energy range, because the relevant hadronic processes change their importance with the energy of the particle. A smooth transition between different models is reached by a random selection of one of these models in the transition region. The physics lists used in this thesis are QGSP_BERT and FTF_BIC. QGSP_BERT is the physics list validated by the LHC experiments, which performs best compared to test beam data [28]. FTF_BIC was chosen since the underlying model is very different from QGSP_BERT, but it showed good

performance compared to data in the past [66]. The composition of these two physics lists and a description of the underlying models are described in the following. The model composition of the two physics lists is shown in Figure 3.4.

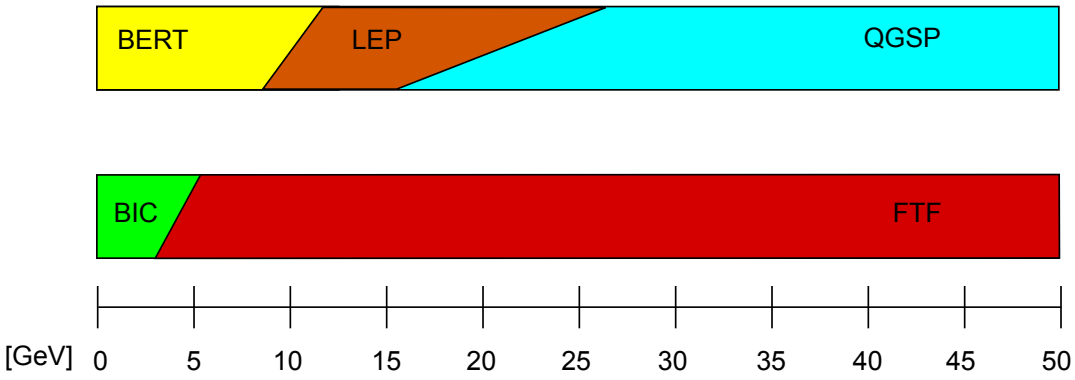

Figure 3.4: Model composition of the two Geant4 physics list used in this thesis.

QGSP_BERT is a model consisting of three underlying models: For low energies ($\lesssim 10\,\text{GeV}$) BERT, which is a Bertini cascade model, and in the medium energy range the parameterization model LEP is used. At higher energies ($\gtrsim 20\,\text{GeV}$) QGSP is applied, which is a quark-gluon string model.

FTF_BIC is a combination of the binary cascade model BIC, which is used for energies $\lesssim 5\,\text{GeV}$, and the Fritiof string model FTF for energies above.

Cascade models describe, like the Bertini model BERT and the binary model BIC, the hadronic cascade due to nucleon-nucleon interactions of the projectile and the material nucleus. Such models are usually used for projectile energies between a few hundred and a few GeV, where the quark sub-structure of the nucleons is not visible, due to their large deBroglie wavelength. All nucleons in the nucleus are treated as a Fermi gas, i.e. up to the Fermi energy, the nucleons occupy all possible states of the system. A minimum energy is required for the creation of secondary particles, due to the Pauli exclusion principle. The distance between two nucleon-nucleon interactions is calculated from modeled nucleon densities and parametrized cross-sections. The differences between Bertini and binary models are based on the treatment of the nucleons inside the struck nucleus and the treatment of an individual hadron-nucleus scattering process.

Parameterization models like LEP are based on fits of experimental data, which predict the production of secondaries in the hadronic cascades. The individual interaction itself is not modeled precisely, therefore energy conservation is only valid on average and not on an event-to-event basis. It is known that the performance of these models reveals significant

discrepancies to data, but they are still used in transition regions of other models, which can not be extended to higher or lower energies.
Parton string models of Geant4 include the quark-gluon string model QGSP and the Fritiof string model FTF. Parton string models are used at high energies, since the quark substructure of the nucleons is taken into account. In an interaction of an incoming hadron with a nucleus a string between two quarks of these objects is formed. The interaction is based on the center-of-mass energies, the impact parameter of the hadron and diffractive and inelastic cross sections. The nucleons inside the struck nucleus are modeled by a harmonic oscillator potential for light nuclei and a Wood-Saxon potential for heavier ones, where each nucleon is assigned a random momentum up to the Fermi momentum. The formed string, which is described by its four-momentum and the constituent quarks, can move due to its constituents and get excited by other nuclei. Strings are successively split as long as the energy is high enough to form new quark-antiquark pairs. Quark-gluon string models and Fritiof string models differ in the string formation and string fragmentation.

Besides the hadronic models, the implementation of the detector geometry and signal generation is important. The conversion from the simulated energy in GeV to a detector signal is done in the digitization. The digitization procedure of the simulations used in this thesis is explained in Subsection 4.1.3.

Chapter 4

Energy reconstruction in the CALICE analog hadron calorimeter

The CALICE collaboration studies calorimeters for experiments at a future linear collider. New materials and technologies are evaluated to build highly granular calorimeters. So far, the CALICE collaboration has built seven calorimeter prototypes (two electromagnetic calorimeters, four hadronic calorimeters and one tail catcher and muon tracker) and tested these prototypes in several test beams at DESY, CERN and Fermilab. The main goal of all these calorimeters is the energy measurement of the incident particles, with detectors optimized for particle flow.
The analysis described in the following focuses on the energy reconstruction and energy resolution of one of the hadronic calorimeter prototypes, namely the analog hadronic calorimeter (AHCAL). In Subsection 4.1.1 the detector design is introduced, followed by the description of the calibration and event reconstruction in Subsection 4.1.2 and the simulation of the calorimeter data in Subsection 4.1.3. The test beam setup used in 2007 at CERN, of which data is presented in this thesis, is explained in Subsection 4.1.4.
The present analyses investigate the energy resolution of pions in the AHCAL, which is a non-compensating sampling calorimeter. The event and run selection of the pion data is described in Section 4.1.5, followed by the results on the intrinsic energy measurement using this data in Subsection 4.1.6. Different techniques were developed to improve the energy resolution in the off-line data analysis. These techniques are referred to as software compensation methods, since they estimate the hadronic and electromagnetic part of a hadronic shower, which are measured with different precision by the calorimeter, and apply weights to the energy components, leading to an equalization of the response to electromagnetic and hadronic particles, and to an overall improved energy reconstruction. A detailed description of the idea behind different methods, their implementation and results are presented in the Sections 4.2, 4.3 and 4.4.

4.1 The CALICE analog hadronic calorimeter

4.1.1 Calorimeter layout

The analog hadronic calorimeter AHCAL is a sampling calorimeter, built as a prototype for a hadron calorimeter at a future linear collider. The design is referred to as “physics“ prototype, investigating and demonstrating the technology, without satisfying the engineering constraints of a collider detector. Since the calorimeter is optimized for particle flow reconstruction it is designed with a high granularity, which manifests itself in active layers of small scintillator tiles, which are individually read out by silicon photomultipliers [67] (SiPM) and placed between 1.7 cm thick stainless steel absorber plates. In total, the hadron calorimeter has 38 sensitive layers, amounting to a depth of 5.3 λ_I. The size of the scintillator tiles in the active layers ranges from $3\times3\,\mathrm{cm}^2$ in the center to $12\times12\,\mathrm{cm}^2$ on the outer edges of the calorimeter. In the last eight layers, for cost reasons, only tiles with $6\times6\,\mathrm{cm}^2$ and $12\times12\,\mathrm{cm}^2$ are used. One scintillator layer of one of the first 30 layers is shown in Figure 4.1 on the right. The total number of scintillator cells is 7608.

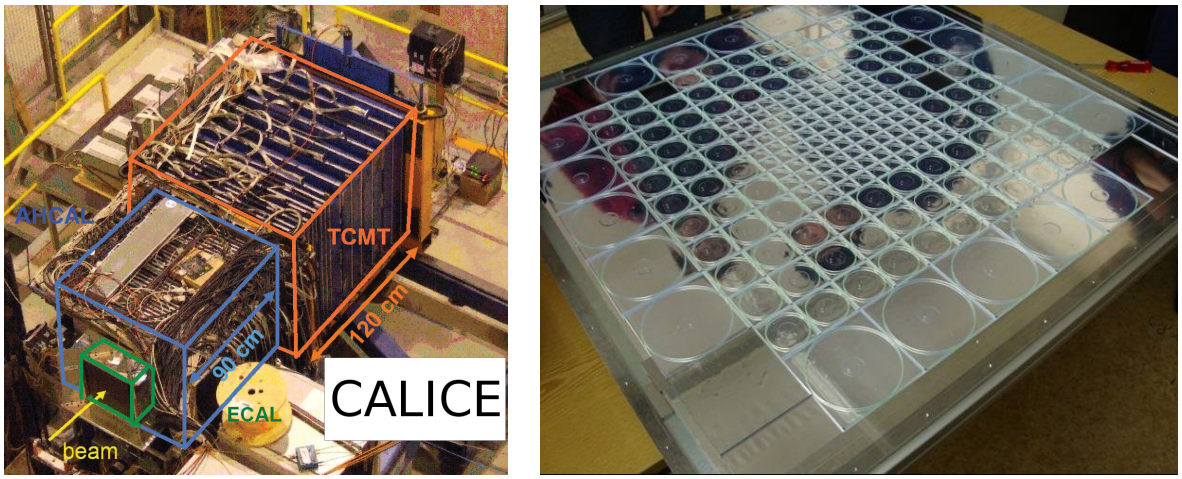

Figure 4.1: (*left:*) AHCAL in the test beam setup described in Section 4.1.4. (*right:*) One scintillator layer of the AHCAL.

The 5 mm thick scintillator tiles are housed in modules, which can easily be moved in or out of the gap between two absorber plates, making the setup flexible and easy to install and dismantle. The modules are made of steel and have a wall thickness of 2 mm. The scintillator tiles are read out by wavelength shifting fibers, which are embedded in a groove in the scintillator. The use of wavelength shifting fibers is necessary to shift the blue light of the scintillator to green, in which wavelength range the SiPM has its highest efficiency. A picture of a $3\times3\,\mathrm{m}^2$ scintillator tile with wavelength shifting fiber is shown in Figure 4.2. The light of the fiber is reflected on the one side by a mirror and detected on the other side by a SiPM.

The large scintillator surfaces sides (top and bottom) of each layer are covered by a reflecting foil for a better light collection. The other sides of the scintillators are matted by chemical etching to prevent light leaking from one tile to another and to provide diffuse light reflection inside the tiles.

4.1.2 Calibration and event reconstruction

The calibration of the CALICE analog hadron calorimeter can be divided into two parts. In one part the response of each scintillator cell to a reference energy is measured and equalized, making the sum of all signals a measure of the detected energy. The reference energy was chosen to be the most probable value of the energy deposition of minimum ionizing particles, for which muons with an energy of 80 GeV were used. The other part refers to the fact that SiPMs saturate, due to their limited number of pixels. Thus, the SiPM response is not linear and the signal has to be corrected for this response behavior, which is measured by a LED calibration system.

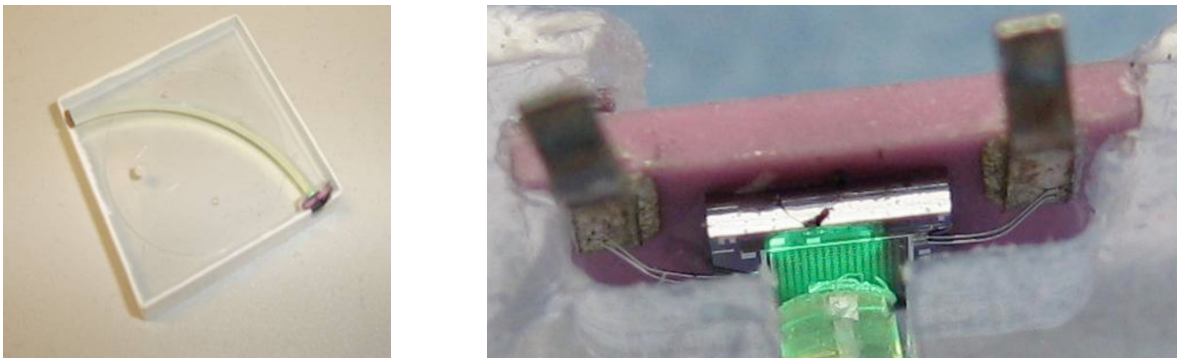

Figure 4.2: (*left:*) Scintillator tile with wavelength shifting fiber. (*right:*) Non-perfect alignment of wavelength shifting fiber light and SiPM surface.

The two calibration parts have to be combined. The final calibration of a single cell i from its raw amplitude A_i to an energy E_i in units of minimum ionization particles is done with the equation below

$$E_i = f_i^{-1}\left((A_i - P_i)\cdot\frac{I_i}{g_i}\right)\cdot\frac{g_i}{I_i}\cdot\frac{1}{M_i}. \tag{4.1}$$

The different steps are explained in the following:

- The pedestal P_i of the channel is subtracted from the raw amplitude A_i. The pedestal is caused by a non-zero baseline of the readout electronics and its measurement is done regularly using random triggers in time windows without beam.
- The resulting signal is divided by the SiPM gain g_i, i.e. the signal is converted from ADC units to pixel, using the inter-calibration factor I_i. The SiPM gain is the number

of electrons of a charge avalanche in a single firing pixel. It is determined in the so called calibration mode of the readout electronics, which is characterized by a high amplification factor and short shaping time. In this mode low intensity LED light from the calibration system illuminates the SiPM so that only a few SiPM pixel fire. By a network of optical fibers, the LED light is injected into each cell. The LED system itself is housed in calibration units on the side of each layer. The system can provide light pulses, comparable to single photon emission, up to light pulses which lead to a complete saturation of the SiPM.
The distance between successive peaks of single pixels defines the SiPM gain. Since data taking is performed in the so called physics mode of the readout electronics (large dynamic range), an inter-calibration factor I_i between the two operation modes is necessary to apply the SiPM gain correction. To determine the inter-calibration factor, the signals of different LED pulses are recorded in both operation modes, making the ratio of these signals a measure of the inter-calibration.

- After the previous step the single cell signal is available in numbers of fired pixels. An inverse saturation function f^{-1} is applied to desaturate the SiPM signal. Since SiPMs have a limited number of pixels they can saturate. The saturation behavior / function was measured for each SiPM before mounting it into the scintillator. Due to possible misalignments, for example because of a not perfect matching between the wavelength shifting fiber and the SiPM, as shown in Figure 4.2 on the right, the actual total number of possible illuminated pixels is not the same for all cells. This is taken into account in the saturation function f. The desaturated signal is converted back to units of ADC using g_i/I_i.

- Finally the signal is converted, using the conversion factor M_I, from ADC units to MIPs. The factor M_i is obtained using muons of an energy of 80 GeV as calibration particles. The energy deposition of a MIP in a detector is defined by the absorber type, density and thickness. The measured energy of a single cell can be represented by the convolution of a Landau and a Gaussian function, describing the energy loss of a minimum ionizing particle in a thin absorber and accounting for smearing by electronic noise and resolution. The peak of the Landau function is the most probable energy loss of a muon and defines the conversion factor M_i.

Temperature dependence The gain calibration factor g_i and the MIP conversion factor M_i are temperature and voltage dependent. The voltage of each SiPM was stabilized during run time. A temperature dependence of the SiPM breakdown voltage, and therefore the temperature dependence of g_i and M_i, is a typical feature of semiconductor devices. Each layer of the AHCAL was equipped with 5 sensors to measure the temperature, which changed by several degrees over a data taking period. The temperature dependence of the SiPM gain and MIP conversion factor has been studied in detail in [68]. During the event reconstruction

a temperature correction is applied to these factors to remove the effects of temperature differences between calibration and run time.

4.1.3 Simulation and Digitization of the AHCAL response

For comparisons of test beam with Monte Carlo simulation data the simulation software Mokka [69] is used. Mokka is based on the Geant4 toolkit, introduced in Chapter 3. The various setups of the CALICE test beams with different detector prototypes are implemented in the Mokka framework. A detailed description of the AHCAL Mokka implementation can be found in [70]. The implementation is based on a very realistic material budget and includes scintillator characteristics in the simulation. For example, Birk's law, which takes the saturation effects for heavily ionizing particles in plastic scintillators into account. Furthermore, the integration time of the readout electronics is implemented with a time cut of 150 ns, which rejects late energy depositions.
Mokka simulates the energy deposition of particles in the calorimeter in units of GeV. The step of digitization is necessary to make the response comparable with raw data. After the digitization the simulated event can be calibrated via the standard reconstruction chain, described in Section 4.1.2. The digitization is performed via the following steps:

- **Ganging:** The scintillator cells of the calorimeter are implemented with sizes of $1 \times 1\text{cm}^2$ in Mokka, to provide flexibility in the size of scintillator tiles in simulation. The ganging transfers the energy deposition of these small cells to the real cell sizes, described in Section 4.1.

- **Light Crosstalk:** A reflective foil covers the large surface sides of each scintillator layer. The neighboring facing tile sides are matted. At the tile edges approximately 2.5 % of the scintillator light is lost per scintillator side to neighboring tiles, which was measured with tiles on a test bench. This light crosstalk is implemented according to the neighboring tile geometry.

- **GeV to MIP conversion:** The two previous steps do not change the energy unit of Mokka, which is GeV. Therefore the signal has to be transfered to units of MIPs. A simulation using muons was performed measuring the pure energy deposition in single tiles after the ganging. The peak of the measured Landau function gives the most probable value for the energy loss. The simulation showed that the mean energy loss of muons changes with muon energy, as expected from the relativistic rise in the Bethe-Bloch equation, Equation 3.1, but the value of the most probable energy loss is relatively stable. Therefore the same factor, determined to 0.1225 MIP/MeV, can be used for test beams with a muon calibration at different energies.

- **SiPM saturation:** The signal is converted into units of pixel and the non-linearity of the SiPM response due to saturation is implemented using the saturation function f,

described in Subsection 4.1.2.

- **Statistical fluctuations:** The limited number of firing pixels leads to statistically significant fluctuations in the modeling of the SiPM response. The number of firing pixel is therefore smeared with a Poisson distribution. After this step the signal is converted from pixel to units of ADCs.

- **Noise:** Electronic noise is not simulated in Mokka. Therefore the noise of single cells are taken from test beam runs (pedestals from random trigger events) and added to the digitized signal.

4.1.4 Test Beam at CERN SPS in 2007

Different test beams were carried out by the CALICE collaboration at DESY, CERN and Fermilab using different electromagnetic and hadronic prototype calorimeters. In 2007 at CERN the test beam was performed with a silicon-tungsten electromagnetic sampling calorimeter (ECAL) [71], the scintillator-steel hadron calorimeter described in Subsection 4.1.1 and a scintillator-steel tail catcher and muon tracker (TCMT). A picture of the three calorimeters at the test beam is shown in Figure 4.1 on the left.
The ECAL has a total depth of $24\,X_0$ or $\sim 1\,\lambda_I$ and consists of 30 active layers arranged in three longitudinal sections with different samplings. The first 10 layers use 1.4 mm thick tungsten absorber plates ($0.4\,X_0$), followed by 10 layers of 2.8 mm thick absorbers ($0.8\,X_0$) and 10 layers of 4.2 mm thickness ($1.2\,X_0$). The total thickness of the calorimeter is 20 cm. Each silicon layer has an active area of $18\times 18\,\mathrm{cm}^2$, segmented into individual modules with 6×6 readout pads with a size of $1\times 1\,\mathrm{cm}^2$. This results in a total of 9720 channels for the detector.
The TCMT consists of 16 readout layers each with 20 $100\times 5\,\mathrm{cm}^2$ scintillator strips read out by SiPMs between steel absorber plates, resulting in 320 readout channels. The detector is subdivided into a fine and a coarse section, where the first 9 active layers have 19 mm thick absorber plates in front, while the absorbers in front of the last 7 active layers are 102 mm thick. The orientation of the scintillator strips alternates between horizontal and vertical in adjacent layers. In total, the TCMT thickness corresponds to a depth of $5.3\,\lambda_I$. This gives a total depth of approximately $13\,\lambda_I$ for the complete CALICE setup.
In addition to the calorimeter system, the setup included several scintillator counters for triggering and beam quality monitoring, drift-chambers to record the incoming particle track and a Cherenkov counter for particle identification. A sketched layout of the beam line is shown in Figure 4.3, which was situated at the CERN SPS north area beam line H6. Secondary particles are generated by sending a high energy proton beam (typically 400 GeV) from the SPS on a beryllium target. In the beryllium target particles, mostly hadrons, electrons and positrons, are generated with different rates. Because of the large ratio of radiation length to

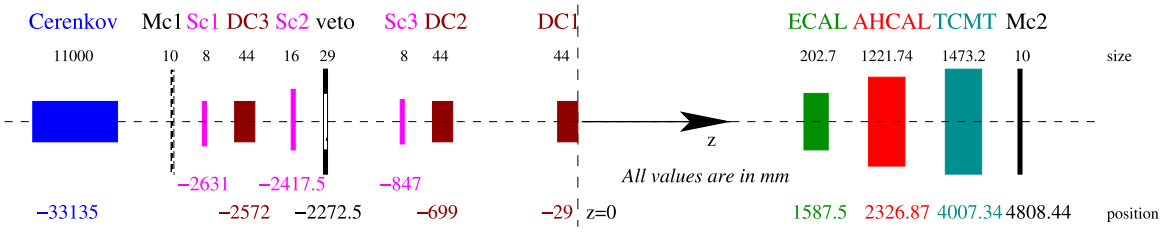

Figure 4.3: Beam Line with calorimeters and additional detectors at the CERN SPS for the test beam time in 2007.

nuclear interaction length[1], beryllium gives a high hadron yield. The produced particles are selected by charge in a magnetic system and can be either used directly or are send on to a second target to produce a tertiary beam of particles with lower energy. Negative secondary hadron beams are mostly pure pions beam, since the production of anti-protons is significantly lower [66] than pion production. One the other hand, positive hadron beams are mostly an admixture of pions and protons. The production cross section of kaons is approximately ten times lower than for pions. A separation of negative pions and electrons and positive pion and protons can be done using the Cherenkov counter information. Since some of the pions decay in flight the runs have a muon admixture as well.

4.1.5 Event and Run Selection

The data samples for the present analysis were extracted from 42 π^- and 10 π^+ test beam runs taken at CERN in 2007 in the energy range 10 – 80 GeV and 30 – 80 GeV, respectively. Run quality checks were performed for all runs, which focused on a valid calibration and average noise level. Runs with an abnormal behavior in one of the following distributions were rejected.

- **Longitudinal profiles:** The longitudinal profile for the full setup (ECAL + AHCAL + TCMT) helped to identify individual noisy or dead layers for a given run. One run with a extremely noisy tail catcher layers was rejected.

- **MIP calibration stability:** In each run, events with muons were identified. These muon events were used to extract the position of the MIP peak. Runs with a valid temperature correction should show the peak position at the calibration value of 1 MIP. One run with a too high estimated MIP peak value, despite the assumed systematic error of the calibration, which is explained in the following, was rejected.

- **Pedestal behavior:** The width of the visible signal distribution for pedestal events was monitored on a run-to-run basis. An abnormal pedestal behavior was observed for one

[1] Beryllium: $X_0 = 35.28\,\text{cm}$, $\lambda_I = 40.7\,\text{cm}$

run taken at highest detected temperature of 29.5 °C.

Histograms illustrating the abnormal behavior of the rejected runs can be found in the Appendix in Section A.1. After these quality assurance procedures 39 runs (29 π^- and 10 π^+ runs) were selected for the further event selection, which are listed in the Tables A.1 and A.2 in the Appendix.
The event selection procedure aimed for the purification of pion samples that have an admixture of muons as well as electrons or protons. The following actions were applied to purify the sample:

- **Muon identification:** To identify and reject events with muons, the information from the TCMT was invoked, requiring low deposited energy both in ECAL + AHCAL and TCMT, with constraints depending on beam energy E_{beam}. The highest muon admixture of 15 % and 30 % was observed for runs with beam energy of 35 GeV and 30 GeV respectively, while for other energies it did not exceed 7 %. The final muon contamination in the pion samples was estimated to be lower than 0.5 % for all energies.

- **Electron and proton identification:** The fraction of electron (proton) to negative (positive) charged pions events in the test beam runs ranged from 0 –71 %. The Cherenkov counter was used to reject events with electrons in π^- samples and protons in the π^+ samples.

- **Multi-particle event identification:** Events are considered as multi-particle events and were rejected if a too high total energy ($> (E_{\text{beam}} + 2.4 \cdot E_{\text{beam}})$) was reconstructed or if more than one ingoing track in the calorimeter was found. For this a dedicated track finder was developed. The fraction of such events was $<$1 % below 50 GeV and $<$2 % above.

- **Empty and bad event identification:** Events with a too small number of hits in the ECAL (< 25) or AHCAL (< 25) were classified as empty events and rejected. Their fraction was less than 0.5 % for all except one run with a beam energy of 10 GeV, for which the fraction was determined to be 3 %.
  Events with a too low energy deposition compared to the beam energy ($< (0.1 \cdot E_{\text{beam}})$) or without a found track in the ECAL and AHCAL before a hadronic interaction, were rejected as well. The fraction of such events was less than 5 % for more than 96 % of all runs.

To analyze the intrinsic AHCAL energy resolution for pions, a constraint was applied to the purified pion samples: the shower start, the position of primary inelastic interaction, was required to be in the first five layers of the AHCAL. This requirement allowed to minimize the effect of leakage and thus, to select hadronic showers which were mostly contained in the AHCAL. A dedicated algorithm was used to find the primary hadronic interaction, described in [72]. The algorithm was tested on simulated samples and showed that the difference

between the found and true primary interaction layer did not exceed one layer for 78 % of events and two layers for more than 90 % of events in the energy range from 10 to 80 GeV.

4.1.6 Reconstructed energy and intrinsic energy resolution

Once all data quality checks were performed the energy of the pion events was calculated. The reconstructed pion energy was determined using the hit energy sum of the ECAL, which was a track of a minimum ionizing particle, the AHCAL and the TCMT. The energy is measured in units of MIPs for all calorimeter types. A conversion to units of GeV was performed, using the conversion factors for each sub-detector, listed in Table 4.1.6. The conversion factor of the ECAL was determined from a Monte Carlo study, using minimum ionizing particles. The AHCAL and the TCMT conversion factor[2] was chosen to obtain a good matching between reconstructed and beam energy at 20 GeV.

Table 4.1: Conversion factors from the MIP to the GeV scale for the different calorimeters and samplings.

Detector	Layers	Conversion factor [GeV/MIP]
ECAL	1-10	0.002953
ECAL	10-20	$2 \cdot 0.002953$
ECAL	20-30	$3 \cdot 0.002953$
AHCAL	1-38	0.0281316
TCMT	1-9	0.0281316
TCMT	10-16	$5 \cdot 0.0281316$

The reconstructed energy distributions were fitted with a Gaussian in the interval of $\pm$ 2 RMS around the mean value. If the resulting χ^2/ndf was not < 2, the fit range was reduced successively by 0.2 RMS till the fit requirement was reached. A fit range reduction due to a $\chi^2/\text{ndf} > 2$ had to be applied for less than 8 % (3 runs) of the runs. Hereinafter, the mean and sigma of the Gaussian fit at a given beam energy, are referred as the reconstructed energy E_{reco} and resolution σ_{reco}, respectively. An example for a 40 GeV π^- run is shown in Figure 4.4. Two statistically independent sets of data were necessary for the software compensation determination and application. For this purpose all test beam runs were split into two sets, one with even and one with odd event numbers. All sets with equal beam energies were merged, finally getting two subsamples for each beam energy. The differences in the reconstructed energy and energy resolution for the single runs and the two sets of merged runs is within the expected uncertainties of systematic and statistics and is shown in the Appendix in Figure A.4. In the following, only one set of the merged data sample and only the runs with π^- events are shown for a better visibility. The linearity and resolution of π^+ and π^- events are included in

[2]The first eight TCMT absorber layers are nearly identical to the ones used in the AHCAL.

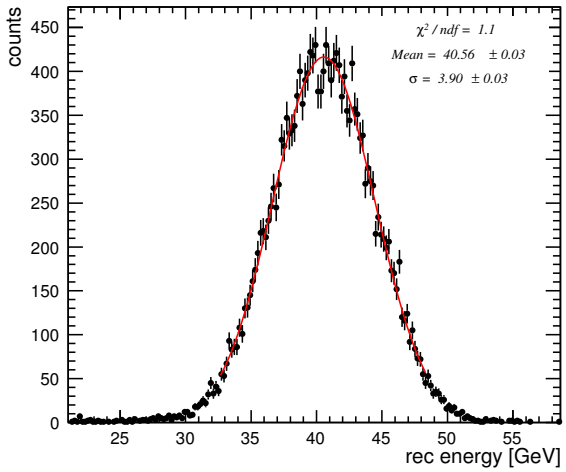

Figure 4.4: Reconstructed energy with Gaussian fit of a 40 GeV pion run.

the Appendix in Figures A.5. In addition, the test beam data is compared to simulated data, which was produced as described in Section 4.1.3. For the simulation the two physics list FTF_BIC and QGSP_BERT were chosen, which are described in Section 3.5, leading to a total of three data set (one test beam data set and two simulated data sets).
Figure 4.5 shows the initial reconstructed energy and energy resolution of the two physics list and the test beam data, for comparison. The simulated data is processed using the same analysis steps described in this section.
The error bars show the statistical and systematic errors. A value of $0.9\% \cdot E_{\text{beam}}$ is assumed for the systematic uncertainties of the calibration and event reconstruction. The systematic uncertainties were studied in detail in [73] for the response to electrons. Two of the most significant sources of systematic uncertainties in the case of electromagnetic showers, the SiPM gain and the effect of saturation, are negligible in the case of hadrons. This can be explained, since hadronic showers are much more diffuse than electromagnetic showers and therefore deposit typically less energy in a single tile, thus the effect of saturation is not significant. Uncertainties in the SiPM gain affect only the saturation correction, making the effect less important for hadronic events, too. The assumptions were confirmed by studies of the energy response for variations of different SiPM gain, MIP and saturation values.
The reconstructed energy of the test beam data (black points) in Figure 4.5 shows a good linearity for beam energies above 20 GeV. Below this value the energy is reconstructed with too low values compared to the beam energy. The difference between beam energy and reconstructed value increases with decreasing beam energy.
The energy resolution was fitted with the function of Equation 3.5 and a stochastic term of 57.3 % with a moderate constant term of 1.8 % was obtained. The noise term c was fixed to a value of 0.18 GeV, corresponding to the noise contribution of the full CALICE setup, taking

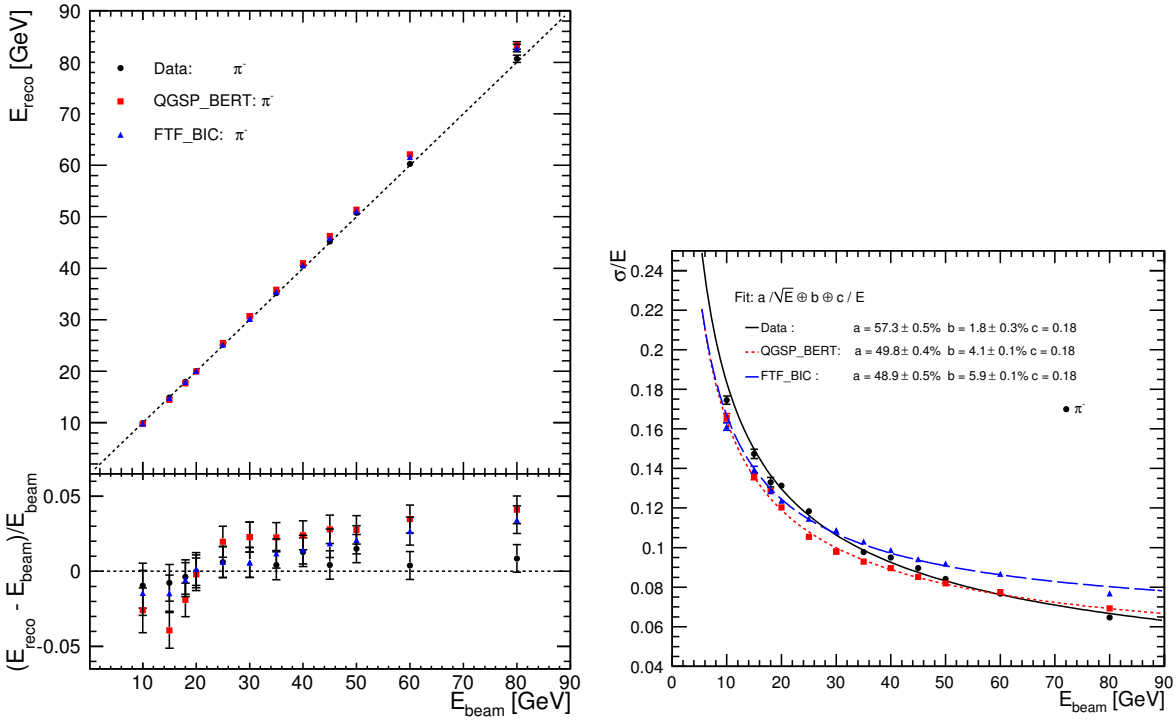

Figure 4.5: Initial reconstructed energy (*left*) and energy resolution (*right*) of test beam data (black circles) and simulation of the physics list QGSP_BERT (red squares) and FTF_BIC (blue triangles).

into account the RMS fluctuations of the noise levels in the ECAL (0.004 GeV), the AHCAL (0.06 GeV) and the TCMT (0.17 GeV). These values were obtained using dedicated runs without particles as well as random trigger events, which were constantly recorded during data taking [73]. Both measurements gave consistent RMS values of the noise contributions. Figure 4.5 includes also the points for data simulated with the physics lists QGSP_BERT (red squares) and FTF_BIC (blue triangles). For the physics list QGSP_BERT, the reconstructed energy of beam energies below 25 GeV is smaller compared to test beam data. In particular, a drop is visible around 12 – 15 GeV. This is due to a change in models of the physics list (see Figure 3.4) and was seen in other CALICE analyses [73, 74] and other physics list validation studies [64], too. For beam energies above 25 GeV the reconstructed energy is higher than for test beam data. This seems to be an effect of the model QGSP used at this energy range in the physics list. The obtained energy resolution points are very close to the ones of test beam data. For small beam energies the energy resolution is better, for high energy it is a little bit worse than the test beam data results. This results in a different shape of the energy resolution and therefore in a significantly lower stochastic and higher constant term of the fit.
The same is true for the energy resolution of the simulated data with the physics list FTF_BIC.

The effect is even more pronounced and therefore the energy resolution of the simulated data with the physics list QGSP_BERT is closer to data than the one using FTF_BIC. The opposite is true for the reconstructed energy. It describes the reconstructed energy of test beam data well for beam energies up to approximately 35 GeV. For higher energies the same behavior as with QGSP_BERT is seen, namely a too high reconstructed energy compared to test beam data.

4.2 Software compensation techniques for the AHCAL of CALICE

The CALICE AHCAL is non-compensating and shows a higher detector response for electrons than for pions, expressed as $e/\pi > 1$. This is due to the fact that a fraction of the deposited energy in hadronic shower cascades is unaccessible for detection, for example the nuclear binding energy, which is released in a nuclear breakup, as discussed in detail in Chapter 3. The invisible energy fraction shows large event-to-event fluctuations, therefore non-compensation degrades the energy resolution of a calorimeter. However, even in intrinsically non-compensating calorimeters, compensation can be achieved by identifying the type of individual energy depositions, namely electromagnetic or hadronic, and by weighting them with suitable factors in the reconstruction software.
The identification of the type of an energy deposition can be achieved via the local energy density in the detector, since electromagnetic showers tend to be much denser than purely hadronic showers, see Chapter 3. To determine the local energy density, for example in units of GeV per cell volume, a high longitudinal and lateral segmentation of the calorimeter readout is required. A higher granularity does allow a greater insight in the substructure of hadronic showers, suggesting that a local software compensation technique is especially powerful in a highly granular calorimeter like the CALICE AHCAL. Such a technique, based on the local energy density of hadronic shower hits in the CALICE AHCAL, is presented in Section 4.3. It tries to identify if the energy deposition in single cells are due to the electromagnetic or the hadronic part of the shower.
It is also possible to examine the shower as a whole and then identify the size of the electromagnetic part. This is applied in global software compensation techniques, which are based on global hadronic shower variables. Two global techniques were developed and are presented in this thesis in Section 4.4. Global software compensation techniques assume that the size of the electromagnetic fraction can be estimated from a combination of shower variables. The main idea behind global software compensation compared to a local one is to be less influenced by possible single hit anomalies. High granularity is also of advantage for global methods, since global shower variables can be determined with a higher precision. The first method, see Subsection 4.4.3, uses the global cluster energy density for a weighting of the full hadronic shower. The second method, see Subsection 4.4.5, uses a neural network

and several global shower properties to determine a more precise detector response.

4.3 Local Software compensation

4.3.1 Implementation

The local software compensation techniques uses the fact that electromagnetic showers tend to be denser than hadronic ones and that therefore typical single hit energy depositions are higher for hits inside an electromagnetic sub-shower than in a hadronic one. Thus, if a hit has a low energy density it is more likely that the hit belongs to the hadronic part of the hadronic shower. If it has a high energy density, it is more likely that it belongs to the electromagnetic part of the hadronic shower.
In order to reach an e/π ratio close to one, different weights are applied to the hits of different energy densities. A bigger weight ω is used for hits with small energy densities ρ and a smaller weight ω is used for hits with a high energy density ρ. The initial energy sum of a hadronic shower changes from

$$E_{\text{initial}} = \sum_{\text{hits}} E_{\text{ecal}} + \sum_{\text{hits}} E_{\text{hcal}} + \sum_{\text{hits}} E_{\text{tcmt}} \tag{4.2}$$

to

$$E_{\text{LocalSC}} = \sum_{\text{hits}} E_{\text{ecal}} + \sum_{\text{hits}} (E_{\text{hcal}} \cdot \omega(\rho)) + \sum_{\text{hits}} E_{\text{tcmt}}. \tag{4.3}$$

The energy deposition inside the electromagnetic calorimeter, which is a track of a minimum ionizing particle, and the tail catcher (longitudinal leakage) is not changed in the overall energy sum. Only hits in the AHCAL are weighted, since the analysis focused on hadronic showers which are mostly contained in the AHCAL due requirement of an to early shower start. A software compensation technique for all calorimeters based on the local energy density, is presented in [75].

Weight determination

To extract a function $\omega(\rho)$, describing the energy density dependences of the weights, the energy density was divided into 15 energy density bins, shown in Figure 4.6. The sum of the hit energies in each of these bins was weighted with a different factor $\omega(\rho)$, where ρ being the energy density center of each bin. For the calculation of the energy density of a given cell, the hit energy in GeV was normalized to the cell volume[3].

[3]The longitudinal size of each layer is the same and was taken into account with a 1 cm. To not have to deal with too small numbers the volume was calculated in units of dm^3.

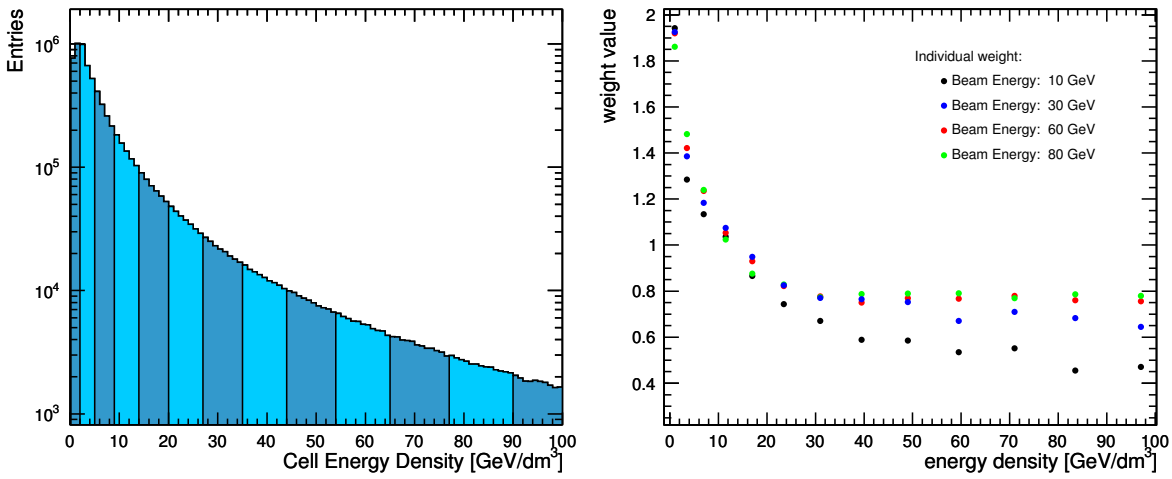

Figure 4.6: (*left*) Binning of local hit energy density. (*right*) Beam energy dependence of the individual weights of the local software compensation technique.

Suitable weights $\omega(\rho)$ were found by minimization of the following function:

$$\chi^2 = \sum_{\text{events}} (E_{\text{LocalSC}} - E_{\text{beam}})^2 \tag{4.4}$$

This was done for all energies to have one set of weights for each beam energy. The individual weights are illustrated on the right of Figure 4.6 for four different beam energies. The visible energy density dependence of the weight factors can be expressed by an exponential function:

$$\omega(\rho) = p_1 \cdot \exp(p_2 \cdot \rho) + p_3. \tag{4.5}$$

This parameterization of the energy density dependence has the advantage that the behavior of the minimization procedure is more stable, since the function enforces a smooth behavior of the weights with energy density, thus eliminating statistical fluctuations from the minimization procedure.
Additionally, differences in the shape of the weights are visible in Figure 4.6 for the four energies, indicating an intrinsic beam energy dependence. Since the e/π ratio changes with beam energy it is expected that the weights change with beam energy as well. This beam energy dependence was taken into account in the weight parameterization, thus, Equation 4.5 changed to:

$$\omega(\rho, E_{\text{beam}}) = p_1(E_{\text{beam}}) \cdot \exp(p_2(E_{\text{beam}}) \cdot \rho) + p_3(E_{\text{beam}}). \tag{4.6}$$

During the weight determination, the shape of the beam energy dependence of p_1, p_2, p_3 was extracted using a minimization procedure analogous to the one described in Equation 4.4, i.e. Equation 4.4 was minimized, but E_{LocalSC} was calculated with constraints on the

weights, expressed by Equation 4.6, instead of using individual weights. To improve the stability of the energy dependence of the three parameters, they were determined in an iterative procedure, first with all three parameters unconstrained in the minimization procedure. After each following iteration one parameter was parameterized by a function, shown in Figure 4.7 and listed in Equation 4.8.

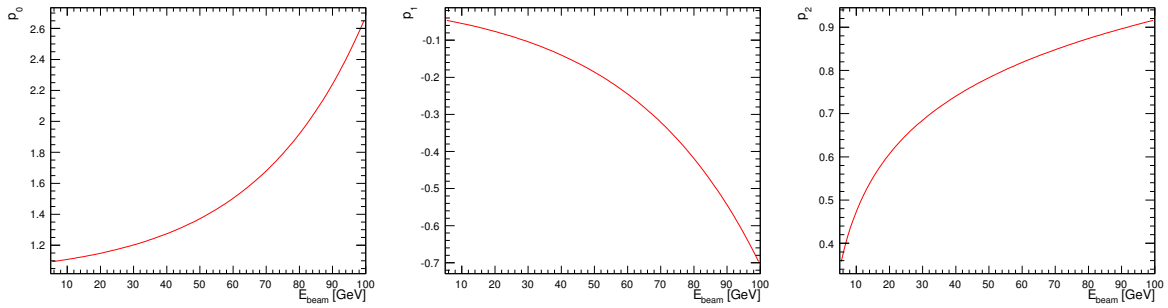

Figure 4.7: Beam energy parameterization of parameters for local software compensation weight function, shown in Equation 4.6. Each parameter $p_1(E_{\text{beam}}), p_2(E_{\text{beam}}), p_3(E_{\text{beam}})$ is parameterized by the function shown in the above figures.

For the application of this local software compensation technique it is assumed that the beam energy is not known. Therefore an estimate of that beam energy from data, namely the initial reconstructed energy E_{initial}, is used to calculate the weights. It was found that the influence on the beam energy is small using E_{initial} instead of E_{beam}. To calculate the weight factor for a single hit it is therefore necessary to determine the initial reconstructed energy of the event and energy density of the hit. The final parameterization of the weights ω for application is given by:

$$\omega(\rho, E_{\text{initial}}) = p_1(E_{\text{initial}}) \cdot \exp\left(p_2(E_{\text{initial}}) \cdot \rho\right) + p_3(E_{\text{initial}}) \tag{4.7}$$

where

$$\begin{aligned} p_1 &= p_{10} + p_{11} \cdot \exp\left(E_{\text{initial}} \cdot p_{12}\right) \\ p_2 &= p_{20} + p_{21} \cdot \exp\left(E_{\text{initial}} \cdot p_{22}\right) \\ p_3 &= p_{30} + p_{31} \cdot \ln\left(E_{\text{initial}} \cdot p_{32}\right). \end{aligned} \tag{4.8}$$

4.3.2 Results with weights derived from test beam data

The results using the local software compensation technique with weights derived from test beam data are presented in Figures 4.8 and 4.9. The parameters for the weighting procedure were determined using the odd events of the merged test beam data runs, while the study of the energy resolution was performed on events with even event numbers. This guarantees statistical independence. The performance using this weight parameterization from test beam

data is presented for the reconstructed energy and energy resolution on test beam data and simulated data.

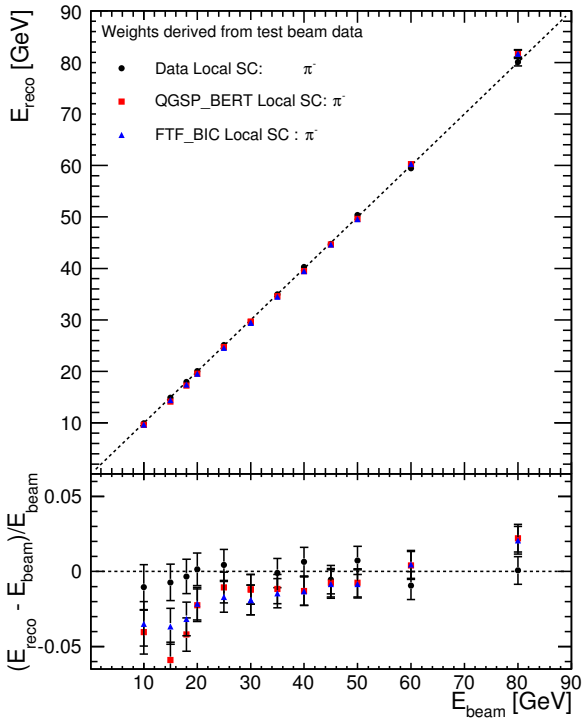

Figure 4.8: Reconstructed energy of test beam data (black circles) and Monte Carlo with the local software compensation with weights which were derived from test beam data. Simulation data of the physics list QGSP_BERT (red squares) and FTF_BIC (blue triangles).

Linearity Comparing the black circles of the initial reconstructed energy in Figure 4.5 with the reconstructed energy using the local software compensation technique, black circles in Figure 4.8, it can be seen that the accuracy of the energy reconstruction of test beam data is not substantially changed using software compensation.
The reconstructed energy of the simulated data (red squares and blue triangles) using the local software compensation technique, decreases over the full energy range compared to the unweighted reconstruction. In view of the initial reconstructed energy this leads to an improvement in the energy reconstruction accuracy for energies above 20 GeV and a degradation for energies below that value. Events are reconstructed to a lower energy if more hits inside the hadronic shower have high energy densities.

Energy Resolution The energy resolution improved for all data sets and all beam energies. The shape of the energy resolution of test beam data did not change significantly, resulting

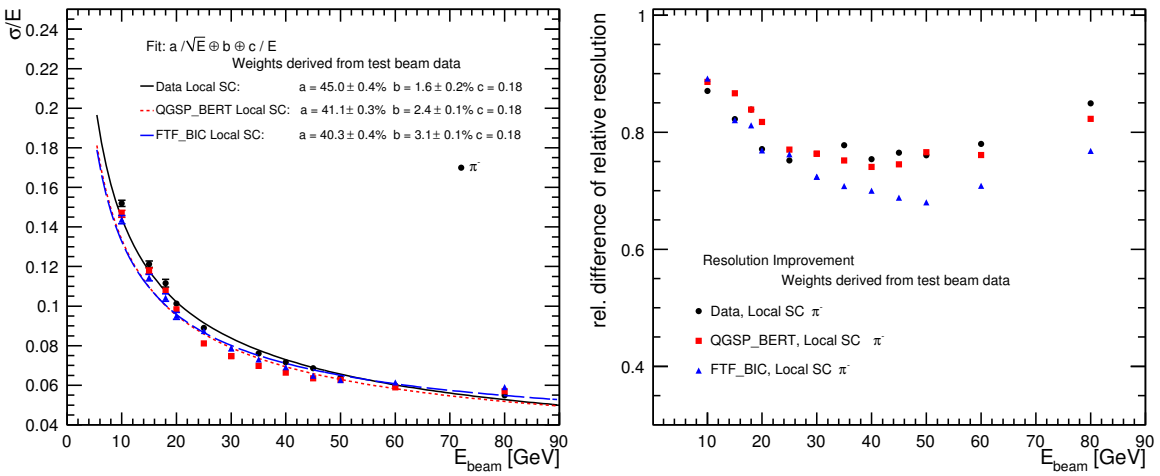

Figure 4.9: Results of the local software compensation techniques for weights derived from test beam data for the energy resolution (*left*) and energy resolution ratio (*right*) of test beam data (black circles) and simulation of the physics list QGSP_BERT (red squares) and FTF_BIC (blue triangles).

in a similar constant term of the fit functions with and without software compensation. The stochastic term of the fit to test beam data decreased from 57.3 % to 45.0 %.
The fit parameters of the energy resolution of simulated data shows a smaller constant term using software compensation (from 4.1 % to 2.4 % and 5.9 % to 3.1 % for simulated data with the physics lists QGSP_BERT and FTF_BIC respectively) and a decrease of the stochastic term (from 49.8 % to 41.1 % and 48.9 % to 40.3 % for simulated data with physics lists QGSP_BERT and FTF_BIC respectively) compared to the initial energy resolution.
It should be noted that the parameters of the fit of the energy resolution using Equation 3.5 are strongly correlated. A higher constant term will lead to a lower stochastic term and vice versa. In general the constant term is the dominant factor for high energies. Thus, although the single energy resolution points of test beam data and simulated data for energies above 40 GeV, are not significantly different, the value of the constant term can change considerately. The stochastic term is mainly determined by low energies, which can be seen in the results for the different data sets. For energies below 60 GeV the energy resolution is larger for the simulated data than for test beam data. It results in a much better value of the stochastic term of the simulated data with the physics list QGSP_BERT of 41.1 % and with the physics list FTF_BIC of 40.3 % compared a value of 45.0 % for test beam data.

Energy Resolution Improvement The energy resolution improvement using software compensation is shown in Figure 4.9 via the ratio of the Gaussian widths with and without software compensation versus the beam energy. For test beam data the improvement is largest

for the middle energy range with a maximum improvement of 25 % and smallest for the lowest and highest energies with 12 – 15 %. Overall, an average improvement of approximately 20 % is achieved.
The improvement of simulated data with physics list QGSP_BERT is comparable with the one of test beam data for beam energies above 20 GeV, while a slightly smaller improvement is obtained for energies below that value. Simulated data with the physics list FTF_BIC shows the reversed behavior.
Over the full energy range the improvement in energy resolution is higher for simulated data with the physics list FTF_BIC compared to QGSP_BERT.

4.3.3 Results with weights derived from Monte Carlo simulations

The weight factors for the local software compensation were not only derived from test beam data but also from simulated data. Thus, two weight parameterizations were extracted, one from simulated data with the physics list QGSP_BERT and the other with the physics list FTF_BIC. These weights were applied to simulated and test beam data. In case of simulated data, the same data sets were used for the weight extraction and weight application. This was different for weight extracted from test beam data.

Linearity The reconstructed energy of all three data sets using software compensation shows, for both weight parameterizations, a deviation from perfect linearity with a maximal deviation from the beam energy of 4 %. Below approximately 30 GeV, the reconstructed energy increases with the beam energy. Above that value the reconstructed energy decreases with increasing beam energy. The point at 80 GeV does not follow this trend, but more runs at different energies above 60 GeV would have been necessary to confirm a further increase of the reconstruction energy.

Energy Resolution The fit values of the energy resolution are very similar for all three data sets comparing the application of the two weight parameterization from simulated data. Also, the parameters of the energy resolution fit do not differ much when comparing the software compensation results with weights derived from test beam data and weights derived from simulated data.

Energy Resolution Improvement Since the energy resolution is similar for the two weight sets, also the energy resolution improvements show almost no differences. In general, it is found that the highest energy resolution improvement, of up to 35 %, can be achieved using simulated data with the physics list FTF_BIC and that weights derived using simulated data with the physics list FTF_BIC lead to a larger improvement at high beam energies.

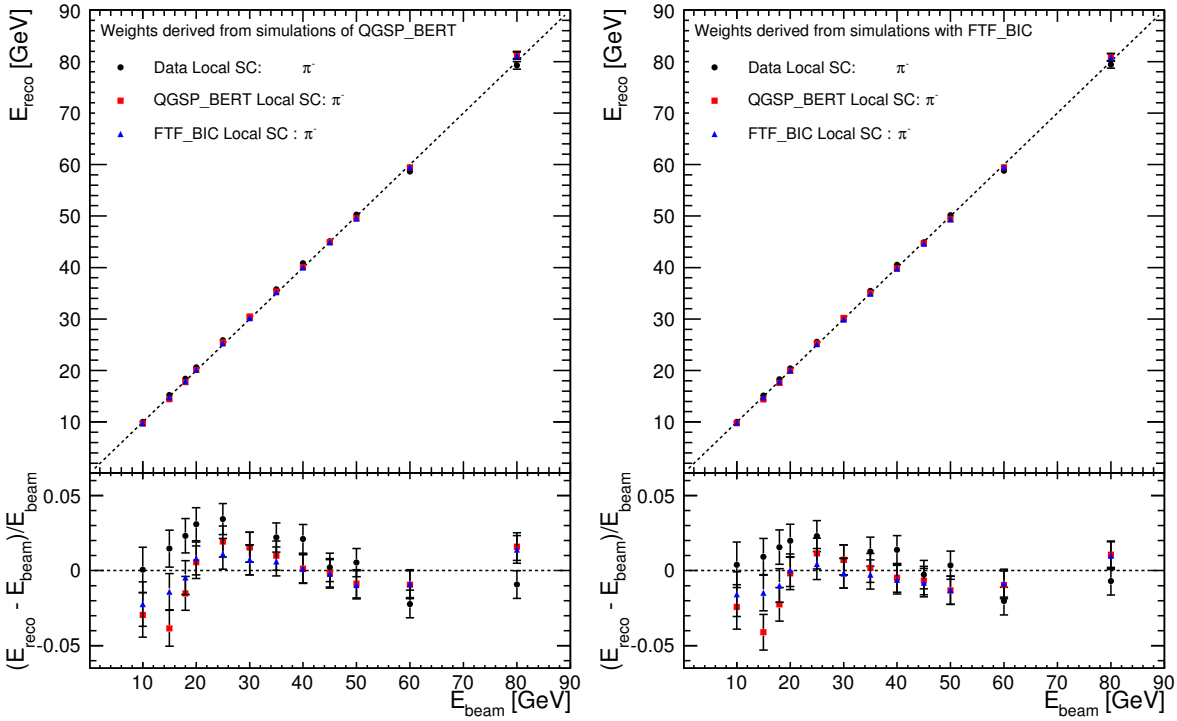

Figure 4.10: Linearity for the local software compensation technique with weights derived from QGSP_BERT (*left*) and FTF_BIC (*right*). Test beam data is shown in black circles, simulation data of the physics list QGSP_BERT in red squares and FTF_BIC in blue triangles.

In this subsection a local software compensation method was introduced, its implementation described and results for different weight parameterizations presented. In the following two global software compensation techniques will be presented, before all methods and data sets are compared to each other in Section 4.5.

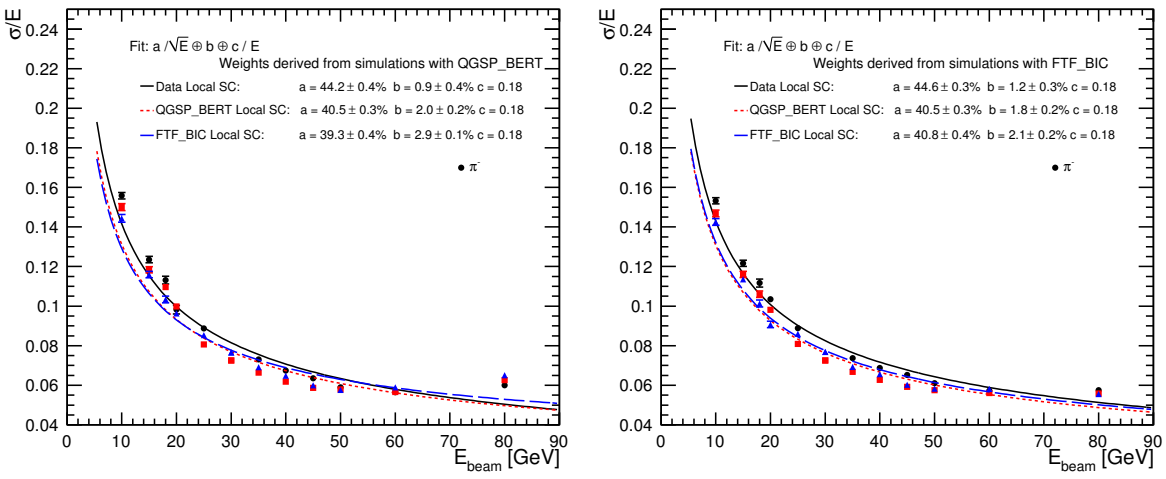

Figure 4.11: Energy resolution for the local software compensation technique with weights derived from QGSP_BERT (*left*) and FTF_BIC (*right*). Test beam data is shown in black circles, simulation data of the physics list QGSP_BERT in red squares and FTF_BIC in blue triangles.

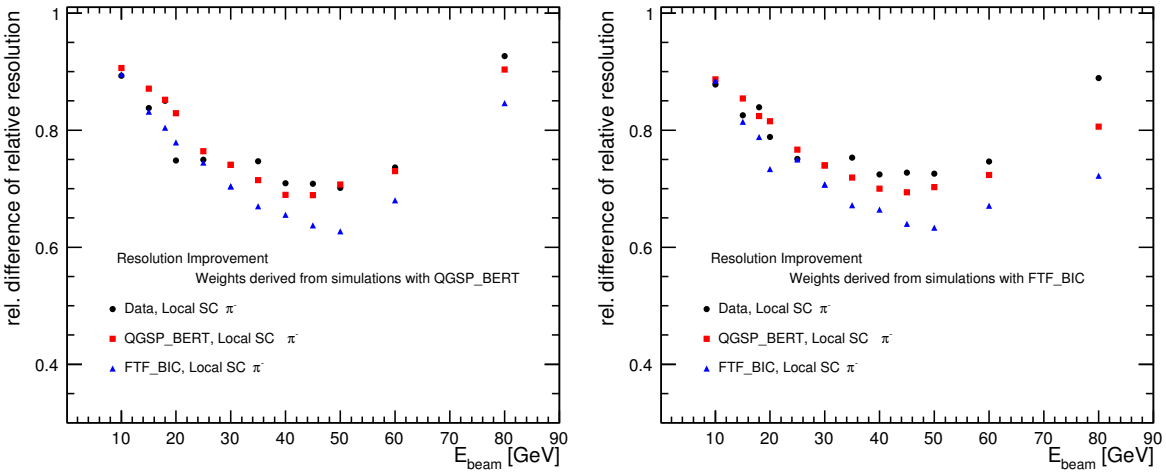

Figure 4.12: Energy resolution ratio for the local software compensation technique with weights derived from QGSP_BERT (*left*) and FTF_BIC (*right*). Test beam data is shown in black circles, simulation data of the physics list QGSP_BERT in red squares and FTF_BIC in blue triangles.

4.4 Global Software compensation

In addition to the local software compensation approach, two global software compensation techniques have been studied. The first one relies on the fact that electromagnetic showers have a higher density, i.e. the same assumption as in the local software compensation technique is invoked. This property can be used on the hit level like in the local method, but also on clusters as a whole. A higher electromagnetic fraction of a hadronic shower increases the overall shower density. The second method assumes that an estimate of the electromagnetic fraction can be extracted from shower properties.
The local software compensation technique presented in this thesis is based on the high granularity of the CALICE calorimeter and takes maximal advantage of it. The goal of the study of global software compensation techniques is to understand if such a method can reach a similar resolution improvement, for example due to reduced impact of single hit anomalies, which might compensate the reduced detail of information. Furthermore it will be compared if a global software compensation technique derived from simulated data can be applied successfully to test beam data as it was the case for the local software compensation technique. The term global is used because one single weight factor is applied to correct the energy measurement and because only variables that describe hadronic showers as a whole were invoked for the global software compensation techniques. Still these variables do take advantage of the calorimeters' high granularity, since their determination can be performed with high accuracy.
To determine shower variables, a clustering algorithm was developed to identify hadronic showers, which is described in Subsection 4.4.1. For each of the hadronic showers, shower properties were calculated, which are introduced in Subsection 4.4.2 together with the reasons for the choice of the used variables. The first global software compensation technique, which is based on a shower weighting depending on the shower energy density, is presented in Subsection 4.4.3. The second technique, presented in Subsection 4.4.5, is based on a neural network.

4.4.1 The Clustering Algorithm

Both global software compensation techniques are based on shower properties, such as the shower length or size. To determine this shower variables a simple clustering algorithm was developed to define showers in the AHCAL. The clustering algorithm is a forward projective method, which starts at the position of the primary hadronic interaction.
The same CALICE data sets of test beam and simulated data, as presented in the previous sections, were used and the same event selection, described in Section 4.1.5, was applied before passing the events to the clustering algorithm. The event selection included the search of the longitudinal position of the primary hadronic interaction, the shower starting point. This starting point was used as a shower seed in the algorithm. For a better comparison of

local and global software compensation techniques in the following, again it was required that the shower start was located in the first five layers of the AHCAL.
Starting from the seed, in an iterative procedure the algorithm collected all neighboring hits of identified cluster hits. It stopped once no new hits could be added to a cluster. Inefficiencies of calorimeter cells or a rather diffuse hadronic shower can lead and an incomplete shower search. Therefore the algorithm searched for extensions of the shower in the end of the calorimeter. In the calorimeter layers before the primary interaction the track leading to the first hadronic interaction was added to the cluster, too.
The clustering of an event was only validated as successful, if the cluster had a size of more that 30 hits in the AHCAL. From pedestal trigger events it is known that the average number of electronic noise hits is about 15 – 20 hits.
The clustering itself was performed in the AHCAL. Since the first hadronic interaction was required to be in the AHCAL the hadron lost energy in the ECAL like a minimum ionizing particle via a track. Due to the low noise of the ECAL the energy of all hits in the ECAL was added to the cluster energy. To account for the leakage in the TCMT the energy of the TCMT needed to be added as well. The tail catcher is a rather noisy detector, therefore not all hits were added by default. Energy measured in the TCMT was only added if the energy of the last five AHCAL layers was more then 1.0 MIP. If this requirement was fulfilled the tail catcher hit energy was added, starting from the front face. A gap of more than two layers without measured energy deposition forced the hit collection in the tail catcher to end and no further possible hits in the end of the tail catcher were collected.
Once the clustering was performed, the energy was transferred from the MIP to the GeV scale. Sine the clustering algorithm could only reconstruct the same or less energy as taking all available hits in the calorimeters, the GeV/MIP conversion factor, shown in Table 4.1.6, of the AHCAL and TCMT were increased by 6 %. Like this a minimal deviation of reconstructed to beam energy is achieved for the energy point of 20 GeV, as in the case without clustering.

Figure 4.13 shows the linearity of the reconstructed energy of test beam and simulated data with the clustering algorithm. The uncertainty of the reconstructed energy of the test beam data increased from $\pm$ 2 %, see Figure 4.5 to $\pm$ 5 %. The stochastic term of the energy resolution increased by approximately 8 %. This is because the cluster algorithm does not always collect the full hadronic shower information. Especially very diffuse hadronic showers, which for example consisted of two main energy deposition areas, connected by an invisible track of a neutral shower particle, were not always collected as a whole.
The clustering algorithm was applied to all sets of test beam and simulated data, introduced in the section about the local software compensation technique. The effect of the clustering algorithm concerning the detector linearity and energy resolution is consistent for test beam and simulated data, i.e. the shape of the energy resolution of simulated data was not changed and the difference between reconstructed cluster energy and beam energy increased for simulated data from 4 % to 10 %, thus by the same factor.

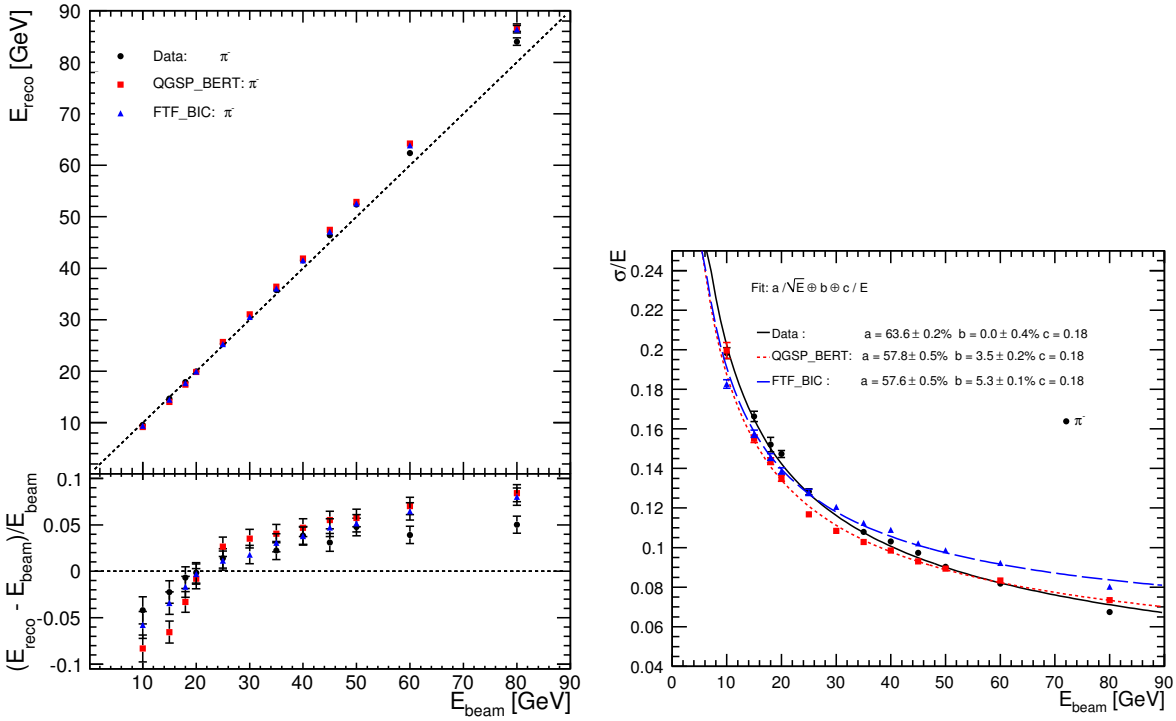

Figure 4.13: Initial reconstructed cluster energy (*left*) and energy resolution (*right*). Test beam data is shown in black circles, simulation data of the physics list QGSP_BERT in red squares and FTF_BIC in blue triangles.

4.4.2 Shower properties

Clusters found by the previous described algorithm were analyzed for the determination of shower properties. The shower properties were used as an input for the global software compensation techniques. Since the techniques aim for the determination of an improved shower energy resolution due to a corrected energy reconstruction and because it is known that the weights need to be energy dependent, variables were selected, which showed a strong beam energy dependence. Figure 4.14 illustrates these shower properties for three different beam energies.

Shower energy The energy sum of all hits in the ECAL, all cluster hits in the AHCAL and all cluster hits in the TCMT defines the total energy of shower. This variable is naturally the most important one for a later energy reconstruction using shower variables, since it provides a first energy estimate.

Shower length The total shower length is defined as the length in layers between the shower starting point and the hit with the highest layer number (in AHCAL or TCMT) of the shower. The shower starting point is the point of the primary hadronic interaction,

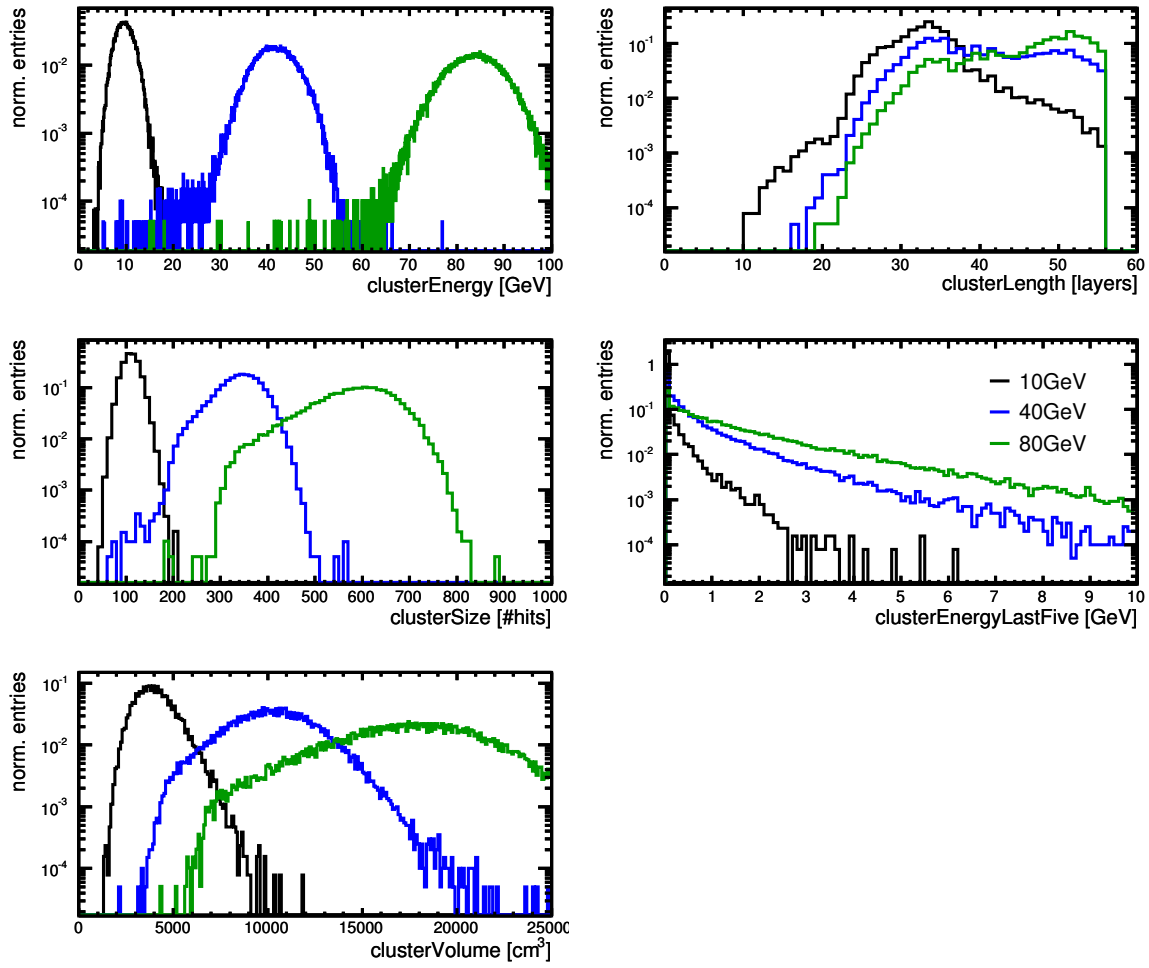

Figure 4.14: Cluster variables distributions for particle energies of 10 GeV, 40 GeV and 80 GeV. All distributions show test beam data.

described in Section 4.1.5. The shower length is a measure of the shape of the shower and gives an indication of the shower compactness, specially since the shower start is required for all events to be located in the first five AHCAL layers.

Shower size The shower size is defined as the number of hits in the cluster (AHCAL and TMCT hits). This variable is another measure for the shower shape and in combination with the shower energy also a measure of the compactness of the shower.

Shower volume The shower volume is defined by the sum of all single tile volumes of the AHCAL. The information of the tail catcher is not taken into account, since a study including the TCMT lead to less accurate description of this variable. The TCMT does not contain scintillator tiles but strips of $100 \times 5\,\mathrm{cm}^2$, thus, the volume cannot be

determined as precise as in the AHCAL. Furthermore most of the shower is contained in the AHCAL, because the primary interaction was required to be in the first five AHCAL layers, giving the TCMT less influence. As shown in the local software compensation and as it will be shown in the global software compensation the volume together with the shower energy provides a very sensitive variable to estimate differences in electromagnetic and hadronic shower components.

Energy in the last five AHCAL layers The cluster energy which is deposited in the last five hadron calorimeter layers, gives an indication of the longitudinal energy deposition.

4.4.3 Global Software compensation using hadron shower densities

The first global software compensation technique described in this thesis is based on a cluster weighting approach, which is similar to the single cell weighting technique described in Section 4.3 and [75]. The global aspect is characterized by the use of only one weight per shower to change the shower energy and by the use of a global input variable, namely the shower energy density, which defines the value of the weight. The shower energy density is defined as the shower energy divided by the shower volume[4].
The suitability of the cluster energy density variable is illustrated in Figure 4.15. On the left, the figure shows the cluster energy density versus the cluster energy for pion induced showers of 40 GeV. Clusters with a high energy density tend to have a higher reconstructed cluster energy. This is not the case for electromagnetic showers. As an example, on the right side of Figure 4.15 the reconstructed cluster energy versus cluster energy density is shown for shower events of a 40 GeV positron run, as well taken during the CALICE test beam campaign. Besides the independence of the cluster energy from the cluster energy density, the energy density of electromagnetic induced showers is typically higher than for hadronic ones. This is also true for the electromagnetic sub-showers of a hadronic shower. Thus, the higher the electromagnetic content of a hadronic shower, the larger the energy density and therefore the reconstructed energy. The figure illustrates that the typical shower density of a 40 GeV positron shower agrees with the highest shower densities of a 40 GeV pion shower, for which the electromagnetic fraction is typically maximal. Therefore, the cluster energy density is chosen as the property to determine the amount of the electromagnetic content. The strength of the correlation between the reconstructed energy and the cluster density depends on the beam energy, since the electromagnetic fraction increases with higher beam energies. Hence, a weighting technique based on the cluster energy density can be applied, if the weights are energy dependent.

[4] Again, the energy density is calculated in units of GeV/dm^3.

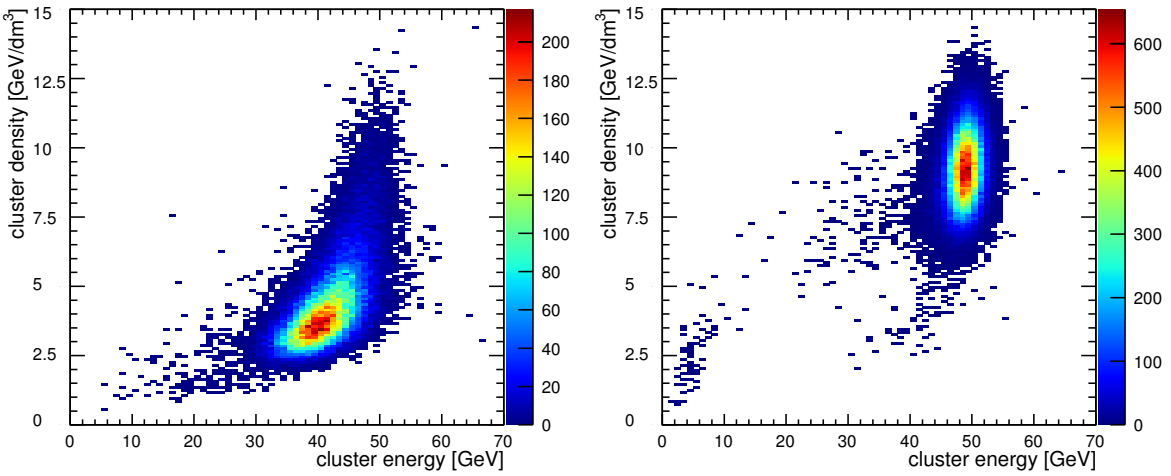

Figure 4.15: Cluster energy versus cluster density for pions (*left*) and positrons (*right*) of 40 GeV. The comparison shows that the reconstructed energy of hadronic showers depends on the energy density and that the overall energy density of electromagnetic shower energy density is on average higher than the hadronic one. Both particle types are calibrated with the same factor for the conversion to the GeV scale. This is not correct in case of the positron energy determination, but necessary to illustrate the increased cluster energy density for hadronic showers.

Implementation

The idea of the cluster weighting technique is to correct the reconstructed cluster energy, which is the sum of all shower hit energies on the GeV scale, $E_{\text{initial}}[\text{GeV}] = \sum_{\text{hit}} E_{\text{hit}}[\text{GeV}]$, by applying a single weight factor $\omega(\rho)$ to cluster energy:

$$E_{\text{GobalSC}}[\text{GeV}] = E_{\text{initial}}[\text{GeV}] \cdot \omega(\rho). \tag{4.9}$$

To obtain the dependence of ω on the cluster energy density ρ, the cluster energy density was divided into 15 bins, which are partially shown in Figure 4.16 on the left. The full range of energy density bins was only needed for high beam energies.
Similar to the local software compensation technique, the weights were found via the minimization of

$$\chi^2 = \sum_{\text{events}} (E_{\text{GlobalSC}} - E_{\text{beam}})^2 \tag{4.10}$$

for every beam energy.
By obtaining individual weights for each beam energy, i.e. without any requirement on the value of the weights, not only the energy density dependence, but also the intrinsic beam energy dependence can be studied. For different beam energies the individual weights versus

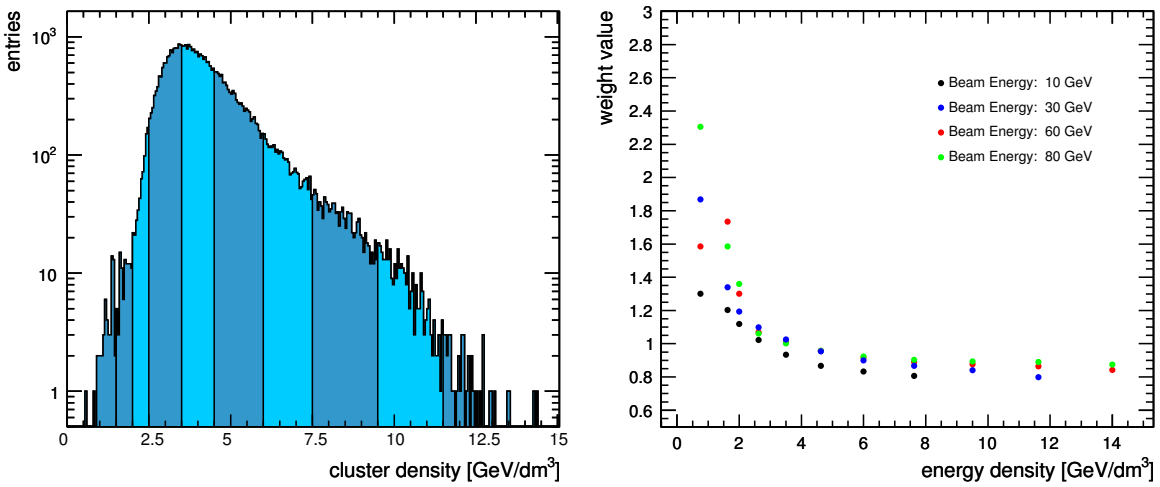

Figure 4.16: (*left*) Binning of global cluster energy density for a 40 GeV test beam data run. (*right*) Beam energy dependence of the individual weights of the global software compensation technique for particle energies of 10 GeV, 30 GeV, 60 GeV and 80 GeV. Not for all beam energies weights can be extracted over the full energy density range, for example the energy densities of a 10 GeV runs did not exceed energy densities of 20 GeV/dm^3.

the shower energy density are shown on the right of Figure 4.16. The distribution of the points was parameterized in the weight determination with the following function:

$$\omega(\rho, E_{\text{beam}}) = p_1(E_{\text{beam}}) \cdot exp(p_2(E_{\text{beam}}) \cdot \rho) + p_3(E_{\text{beam}}). \tag{4.11}$$

In this function, the parameter p_0, p_1, p_2 are energy dependent functions itself and ρ is the center of the corresponding energy density bin. Using the minimization of Equation 4.10 and the weight parameterization of Equation 4.11, the beam energy dependence of the parameters p_0, p_1, p_2 was found. This was done analog to the local software compensation by an iterative minimization of Equation 4.11, each time constraining one more of the p_0, p_1, p_2 parameters with a function shown in Figure 4.17.
The final parameterization of the weights ω, when applying the software compensation to a data set, is given by

$$\omega(\rho, E_{\text{initial}}) = p_1(E_{\text{initial}}) \cdot \exp\left(p_2(E_{\text{initial}}) \cdot \rho\right) + p_3(E_{\text{initial}}), \tag{4.12}$$

where

$$\begin{aligned} p_1 &= p_{10} + p_{11} \cdot \exp\left(E_{\text{initial}} \cdot p_{12}\right) \\ p_2 &= p_{20} + p_{21} \cdot \exp\left(E_{\text{initial}} \cdot p_{22}\right) \\ p_3 &= p_{30} + p_{31} \cdot \ln\left(E_{\text{initial}} \cdot p_{32}\right). \end{aligned} \tag{4.13}$$

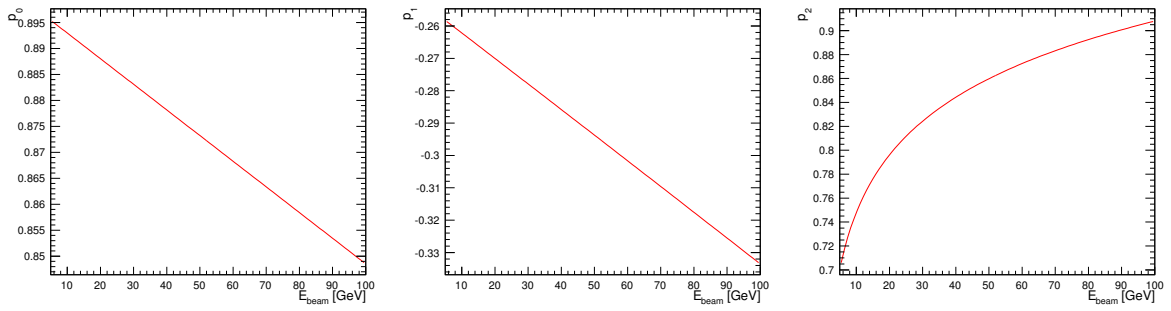

Figure 4.17: Parametrization of parameters for the weight function of the global software compensation technique. Each parameter $p_1(E_{\text{beam}}), p_2(E_{\text{beam}}), p_3(E_{\text{beam}})$ used Equation 4.11 is parameterized by the function shown in the above figures.

The beam energy, which was used to determine the weight parameterization, is replaced by the initially reconstructed energy, which is more realistic if one assumes the beam energy is unknown. Thus, for the final weight calculation of the global software compensation technique, the initial reconstructed energy and the cluster energy density are used as an input. The results of the application with weights extracted from test beam data are presented in Figures 4.18 and 4.19. Weight parameterizations were also extracted from simulated data with the physics list QGSP_BERT and FTF_BIC. All possible applications of the two weight sets on test beam data and simulated data are shown in Figures 4.20 and 4.21.

Results with weights derived from test beam data

The results for the reconstructed energy of the global software compensation technique using weights extracted from test beam data are shown in Figure 4.18 and for the energy resolution in Figure 4.19.

Linearity The deviation of the reconstructed energy from the beam energy of the test beam data improved significantly from $\pm 5\,\%$, see Figure 4.13, to approximately $\pm 2\,\%$. Also, the deviation of simulated data of both physics lists improved for energies above 20 GeV, where the energy was initially reconstructed too high, compared to the beam energy. At these energies the showers of simulated data tend to have a higher energy density than test beam data, as shown in the Appendix in Section A.4. Thus, smaller weights are applied for simulated data compared to test beam data. Overall the accuracy of simulated data with the physics list QGSP_BERT is within 8 % and with FTF_BIC is 7 %.
For simulated data, which initially was reconstructed to an energy smaller than test beam data, the weighting did not improve the detector response much. In this energy range the simulated data does not show a significantly lower energy density (see Figure A.8), which would have been necessary for a higher reconstructed energy using the software compensation approach.

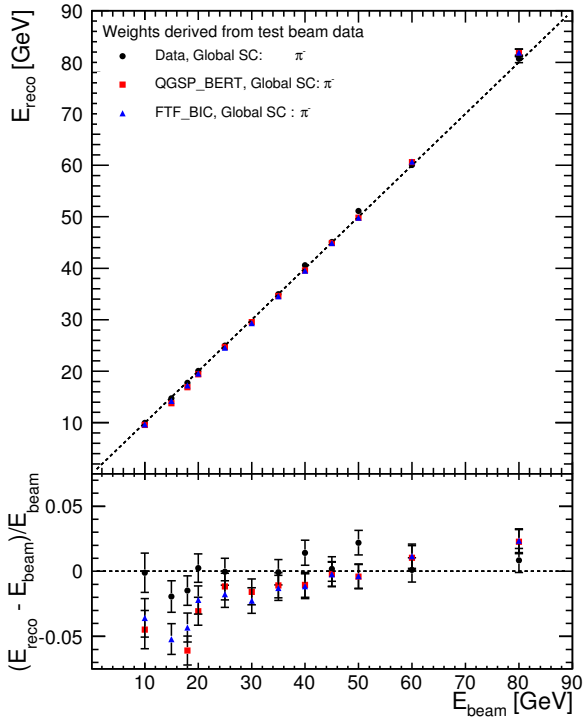

Figure 4.18: Reconstructed cluster energy with the weights of the global software compensation technique derived from test beam data. Test beam data is shown in black circles, simulation data of the physics list QGSP_BERT in red squares and FTF_BIC in blue triangles.

Overall the values of the reconstructed energies of the simulated data decreased compared to the reconstruction without weighting.

Energy Resolution The global software compensation technique based on energy density weights improves the stochastic term of the energy resolution fit by 18 % for data and by 13 % for the simulated data. The improvement is different for test beam and simulated data, since in case for the simulated data the constant term was reduced in addition, from 3.5 % and 5.3 % without software compensation, to 0.6 % and 2.2 % with software compensation, for QGSP_BERT and FTF_BIC respectively. In case of test beam data the constant term is in both cases zero. The characteristics of the physics list using the software compensation with test beam data derived weights, are still present: the fit parameters obtained from simulated events using with the physics list FTF_BIC show a smaller stochastic term of 49.9 % but a higher constant term than simulations using the physics list QGSP_BERT (stochastic term 50.5 %).

Energy Resolution Improvement The energy resolution improvement is very similar for all data sets in the energy range 10 – 25 GeV with approximately 15 %. Above that range

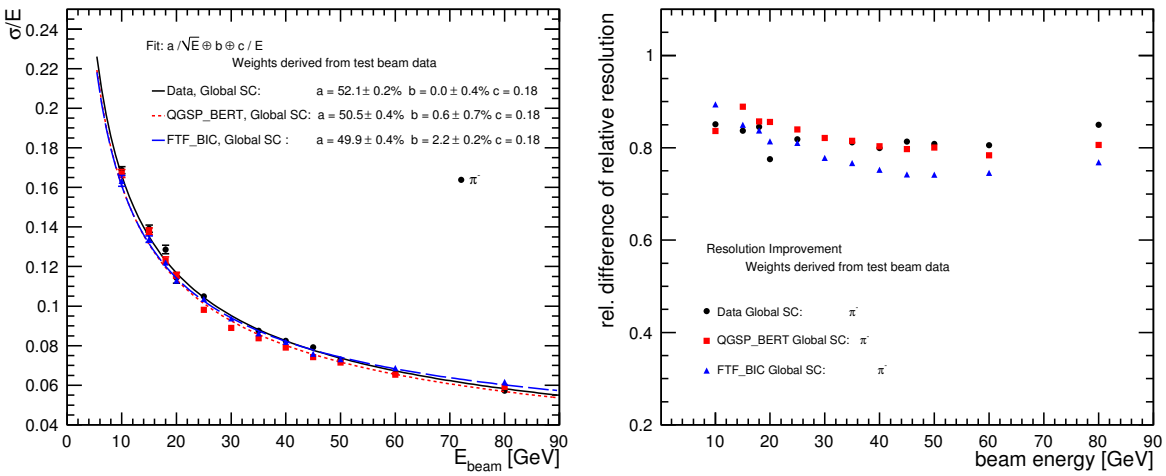

Figure 4.19: Energy resolution (*left*) and energy resolution improvement (*right*) with the weights of the global software compensation technique derived from test beam data. Test beam data is shown in black circles, simulation data of the physics list QGSP_BERT in red squares and FTF_BIC in blue triangles.

test beam data and simulated data with the physics list QGSP_BERT show a very similar and constant energy resolution improvement of approximately 17 %. For simulated data with the physics list FTF_BIC the improvement is larger, reaching up to 25 %.

4.4.4 Results with weights derived from Monte Carlo simulations

Weights were also extracted from simulated events, as in the case of the local software compensation technique. This led to two sets of weight parameterizations, namely one using simulated data with physics list QGSP_BERT and one with the physics list FTF_BIC. The results of the global software compensation technique using these two sets are compared to each other in the following. In addition the results are also compared to the ones obtained with weights extracted from test beam data.

Linearity The application of software compensation with weights derived from simulated data to test beam data led to reconstructed energies which were approximately 5 % to high at low energies, compared to the beam energies. Figure A.6 in the Appendix shows this behavior for both weight parameterizations. The reason is based on the differences in the initially reconstructed energy and energy density of test beam and simulated data. Especially at low beam energies these differences have a high influence. The correction due to weighting is highest at low energies, due to large differences between the electromagnetic and the hadronic fraction.

The energy reconstructed with software compensation was corrected with a first order polynomial accounting for this difference, as shown Figure A.6 in the Appendix. The reconstructed energy of simulated data was not corrected.
The final reconstructed energies using software compensation are shown in Figure 4.20. The corrected energy of test beam data is flat with an accuracy of about 2 %. The accuracy of the cluster energy reconstruction of simulated data is better using the weights from simulated data, which is no surprise. Simulated data with the physics list FTF_BIC reaches an accuracy of approximately 2 % and simulated data with the physics list QGSP_BERT 5 %.

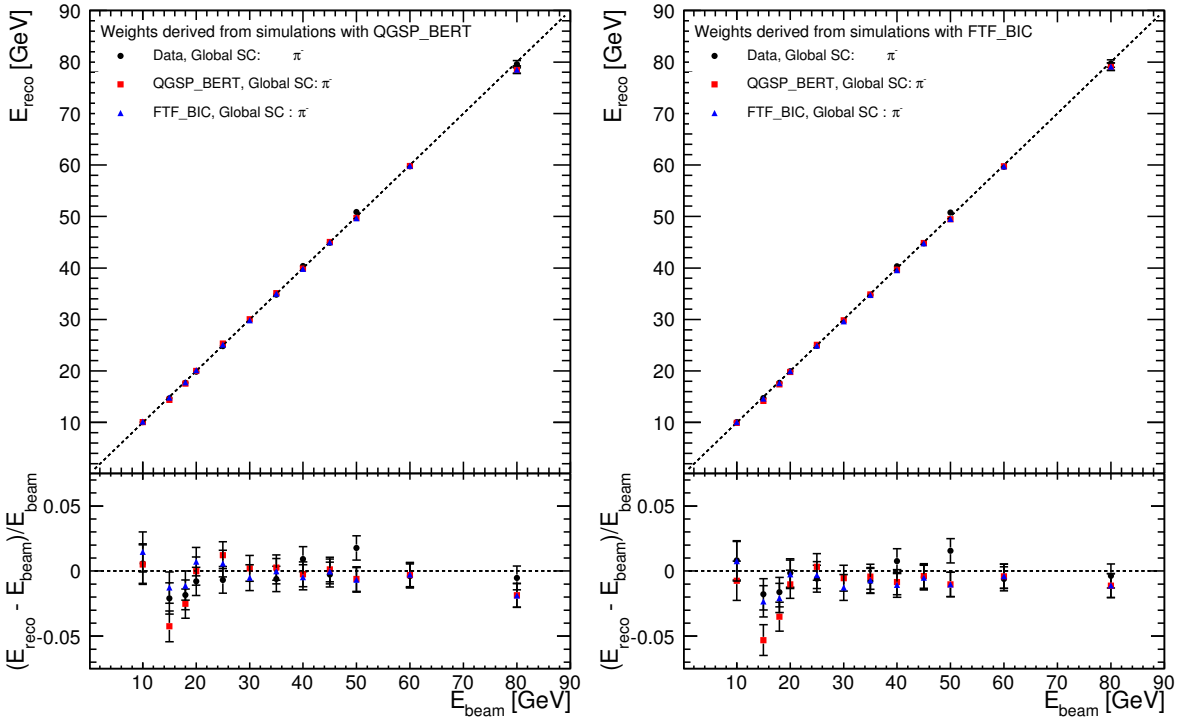

Figure 4.20: Reconstructed cluster energy with the weights of the global software compensation technique derived from simulated data of the hadronic physics lists QGSP_BERT (*left*) and FTF_BIC (*right*). Test beam data is shown in black circles, simulation data of the physics list QGSP_BERT in red squares and FTF_BIC in blue triangles.

Energy Resolution Due to the linearity correction of the test beam data not only the reconstructed energy changed but also the energy resolution, since it is defined by the ratio of Gaussian width to reconstructed energy σ/E. If the energy resolution improvement was purely due to an increase of reconstructed energy, the energy resolution would be significantly worse after this correction. This is not the case, as seen by the comparison of Figure A.7 before the correction and Figure 4.21 afterwards. Thus, the global software compensation led

to a real energy resolution improvement.
Comparing the fit energy resolution results obtained with weights of the two physics list (left and right side of Figure 4.21), it can be seen that the fit values for one data sample, give nearly the same numbers. Comparing the energy resolution fits of the different data sample to each other, the performance of the simulated data is better, since the stochastic terms of the fits are nearly equal to the ones with weights derived from test beam data, but the constant terms are reduced.

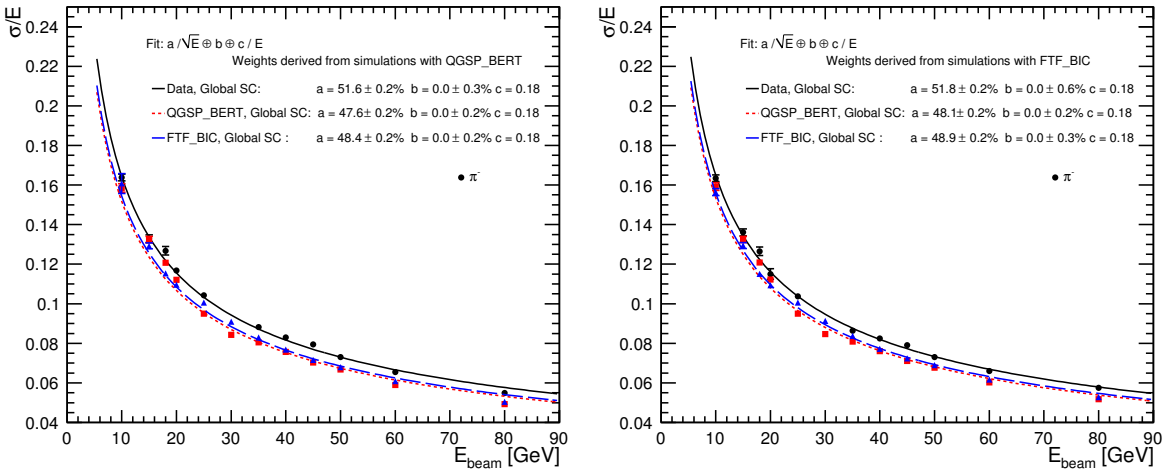

Figure 4.21: Energy resolution with the weights of the global software compensation technique derived from simulated data of the hadronic physics lists QGSP_BERT (*left*) and FTF_BIC (*right*). Test beam data is shown in black circles, simulation data of the physics list QGSP_BERT in red squares and FTF_BIC in blue triangles.

Energy Resolution Improvement Figure 4.22 shows the energy resolution improvement for weights derived from simulated data. Both weight parameterization give similar results. The energy resolution improvement for test beam data is nearly flat over the full energy range with an improvement of approximately 18 %. For simulated data the energy resolution improvement increases with increasing beam energy leading to an average improvement of 22 – 25 % for both physics lists. Again, as it was the case for the weights obtained with test beam data, the data simulated with physics list FTF_BIC improved most.

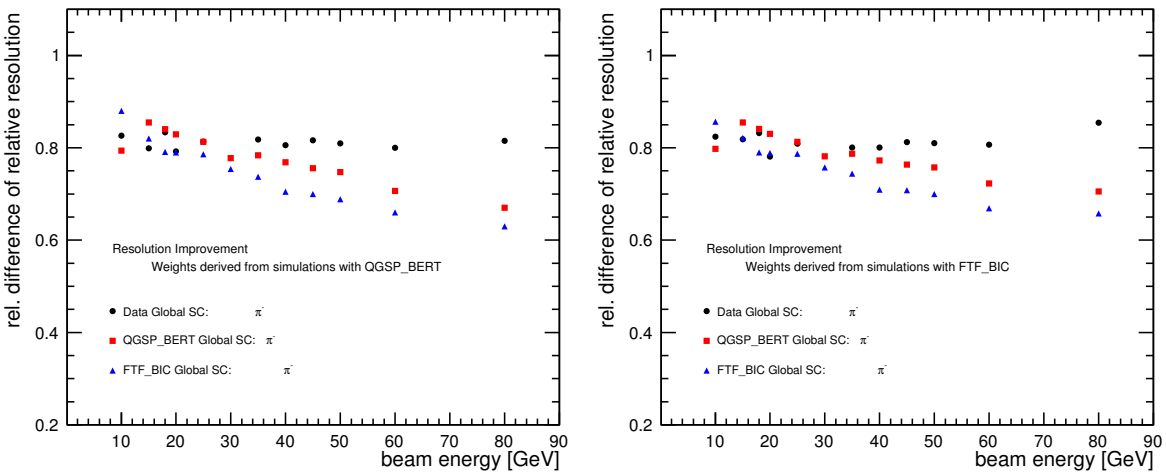

Figure 4.22: Energy resolution improvement with the weights of the global software compensation technique derived from simulated data of the hadronic physics lists QGSP_BERT (*left*) and FTF_BIC (*right*). Test beam data is shown in black circles, simulation data of the physics list QGSP_BERT in red squares and FTF_BIC in blue triangles.

4.4.5 Global Software compensation using a Neural Network

The second global software compensation technique presented in this thesis determines the reconstructed shower energy from the output of a neural network. The program TMVA [76] (Toolkit for Multivariate Data Analysis with ROOT) was used to perform a neural network regression analysis.
An artificial neural network consists of an interconnected group of artificial neurons. The neurons form an adaptive system that, used in regression mode, tries to model a variable from a number of input variables. Therefore, the regression approach is often called function approximation. The neural network approach was chosen since a neural network can model complex relationships between inputs and outputs and can find patterns in data. The neurons of a neural network architecture are grouped in different layers. In the first layer, the neurons represent the input variables of the neural network. The last layer is the output of the regression method, thus the output of the approximated function. The layers in between are called hidden layers. Their number and the number of neurons in each hidden layer have to be defined by the user in neural network implementation of TMVA.
In this analysis the input variables of the neural network were the shower properties, described in Section 4.4.2. The neural network was built to estimate the reconstructed energy of an event. During the training phase, a target value, namely the beam energy, was provided to the neural network. In the testing and application phase, the target value was not provided to the neural network.

Training and Testing of the neural network

The neural network had to be trained with a special set of simulated data. Using the so far presented data samples of beam energies between 10 – 80 GeV led to a over-trained neural network. I.e. the neural network easily recognized the steps in beam energy of mostly 5 GeV between two successive beam energies and only used the information of the initial reconstructed energy for its output value determination. Thus, reconstructed energy of each beam energy using the neural network consisted not of Gaussian like distributions but instead of delta-peaks around the beam energies. An application of such a trained neural network to a set of data with different beam energies from the ones used in the training phase would fail to properly reconstruct shower energies.
Therefore, a data set with a quasi-continuous beam energy distribution was needed for the neural network training. Such a data set was generated by the simulation of single particle pion events in the test beam data setup with energies from 5 GeV to 105 GeV in energy steps of 0.1 GeV. For each energy step 200 π^- events were simulated with the physics lists QGSP_BERT and FTF_BIC. The simulated data sets where analyzed with the clustering algorithm, see Subsection 4.4.1, to determine the cluster variables introduced in see Subsection 4.4.2.
The neural network was trained to minimize the absolute deviation of the output value, the reconstructed cluster energy, from the target value, the beam energy. However, for a good energy reconstruction over a certain energy range not the absolute deviation but instead the relative deviation is significant. Large target values thus were overemphasized in the training of the neural network. Thus, a weight expression, which gave events with lower energies (target values) more weight, was introduced in the training phase of the neural network. A number of network architectures were tested to find the one with the best performance. For simplicity, an architecture with a single hidden layer was chosen.
Testing the neural network means applying the weights of the neural network on a data set which has not been used for the training of the neural network. Two neural networks were trained using simulated data with physics lists FTF_BIC and QGSP_BERT. The neural networks were applied to the test beam data and simulated data samples used in the previous sections.

Results with weights derived from Monte Carlo simulations

The below presented results are for a neural network architecture which gave the best performance in linearity and energy resolution. For the neural network, trained with simulated data using simulated data with physics lists QGSP_BERT and FTF_BIC, this was an architecture of one hidden layer and $N+5$ neurons, where N is the number of input variables. For both architectures the same six cluster variables were used as in input.

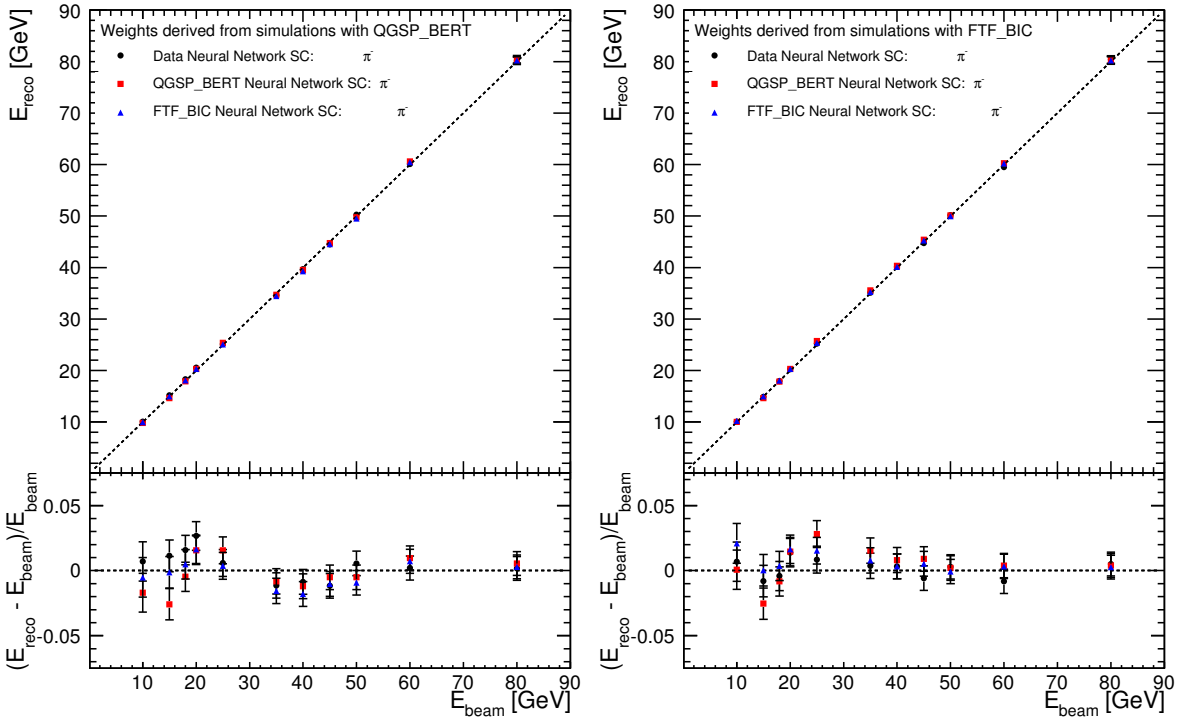

Figure 4.23: Reconstructed cluster energy with the weights of the neural network software compensation technique derived from simulated data of the hadronic physics lists QGSP_BERT (*left*) and FTF_BIC (*right*). Test beam data is shown in black circles, simulation data of the physics list QGSP_BERT in red squares and FTF_BIC in blue triangles.

Linearity The reconstructed energy of test beam data using the neural network was too high at low beam energies, shown in Figure A.11, as in the case of the global software compensation weighting technique based on energy density. Thus, also for this method the energy of test beam data was corrected using a function, described in the Appendix Section A.5. Again, the reconstructed energy of simulated data was not corrected.
Without this correction the neural network determined, in the energy range between 10 – 30 GeV, the reconstructed energy to a 4 % value higher than the beam energy. This is due to the sensitivity of the neural network to differences between test beam and simulated data. Thus, at low energies this is mostly due to the too low reconstructed initial energies of simulated data and in the medium energy range due to a smaller reconstructed shower volume. Both facts lead to an overestimation of the reconstructed test beam energy, because a larger electromagnetic fraction in the test beam data is assumed by the neural network. The comparison of cluster properties between test beam data and simulated data of the energies 10 GeV, 40 GeV and 80 GeV is shown in Figures A.13, A.14 and A.15, respectively.
The final reconstructed energy of the test beam data, Figure 4.23, shows a deviations between

reconstructed and beam energy of approximately ±1 % for the neural network trained using simulated data with the physics list FTF_BIC. For the neural network trained using simulated data with the physics list QGSP_BERT the deviation is approximately ±3 %.
The linearity of the simulated data with the physics list FTF_BIC shows a very good accuracy of about ±2 %. The linearity of the simulated data with the physics list QGSP_BERT shows an accuracy of ±3 %. The larger deviation from linearity of simulated data with physics list QGSP_BERT is due to the typical drop at 12 GeV, where a transition of hadronic models is situated, as described in Section 3.5.

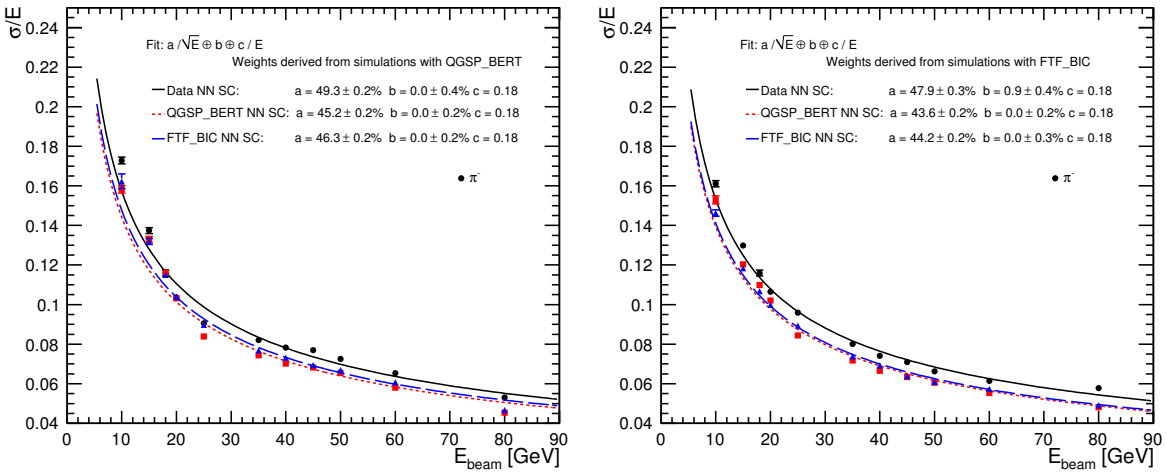

Figure 4.24: Energy resolution with the weights of the neural network software compensation technique derived from simulated data of the hadronic physics lists QGSP_BERT (*left*) and FTF_BIC (*right*). Test beam data is shown in black circles, simulation data of the physics list QGSP_BERT in red squares and FTF_BIC in blue triangles.

Energy Resolution As for the single cluster weights, the additional correction of the reconstructed energy after the neural network, does not degrade the resolution significantly. The fits of the energy resolution are shown in Figure 4.24. The stochastic terms are reduced to 5 – 6 % smaller values compared to the other global software compensation technique presented in this thesis, with values of 49 % for test beam data and 45 – 46 % for simulated data. Additionally the constant term is zero for the simulated data samples and small (<1 %) in case if test beam data. The neural network trained using simulated data with the physics list FTF_BIC reaches slightly better results than QGSP_BERT.

Energy Resolution Improvement The energy resolution improvement is better for simulated data (on average 30 % improvement) than for test beam data (on average 22 % improvement), as in the case of the other global software compensation technique. Simulated

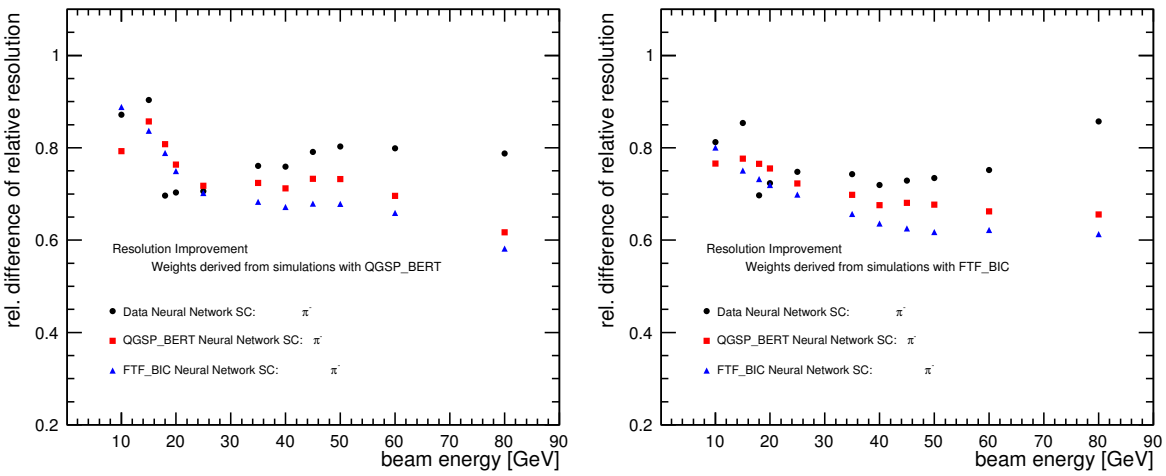

Figure 4.25: Energy resolution improvement with the weights of the neural network software compensation technique derived from simulated data of the hadronic physics lists QGSP_BERT (*left*) and FTF_BIC (*right*). Test beam data is shown in black circles, simulation data of the physics list QGSP_BERT in red squares and FTF_BIC in blue triangles.

data with the physics list FTF_BIC results in a larger energy resolution improvement than simulated data with the physics list QGSP_BERT, for both neural networks.

4.5 Summary

Three different software compensation techniques were developed for the energy reconstruction of pions in the CALICE analog hadron calorimeter. All methods use the fact that electromagnetic showers have other characteristics than hadronic showers. These differences can be used to estimated the sharing of energy between the electromagnetic and the hadronic fraction in a hadronic shower.
The local and one of the global software compensation techniques presented in this thesis, directly used the fact that electromagnetic showers have typically a higher energy density than hadronic showers. In the local software compensation this was used on the hit level. Each single hit energy was corrected with a weight, which was calculated from the value of the single hit energy density. In the global software compensation, the cluster energy was corrected for each event, i.e. a suitable weight factor, based on the value of the cluster energy density, was applied to the cluster energy. Weights of both techniques needed to be parameterized by a function, which was energy and energy density dependent. Different weight parameterizations were extracted from test beam and simulated data.
The third presented approach was a global software compensation technique based on a neural network. In this method the corrected reconstructed energy was estimated from a number of

shower variables. Since the correct training of the neural network required a quasi-continuous particle energy distribution, it could only be performed with simulated data.
The weights of all techniques and data samples were applied to all available sets of test beam and simulated data. Results for the energy resolution, the deviation of reconstructed energy from beam energy, and the energy resolution improvement, given by the ratio of the fitted Gaussian width of the reconstructed energy with and without software compensation, were discussed.
In the following, results obtained with the different techniques for various data samples are summarized in three parts, each illustrated by a schematic (Figures 4.26, 4.27 and 4.28).

- First, the differences between the performance of the local energy density software compensation technique, the global energy density software compensation technique and the neural network software compensation are discussed.

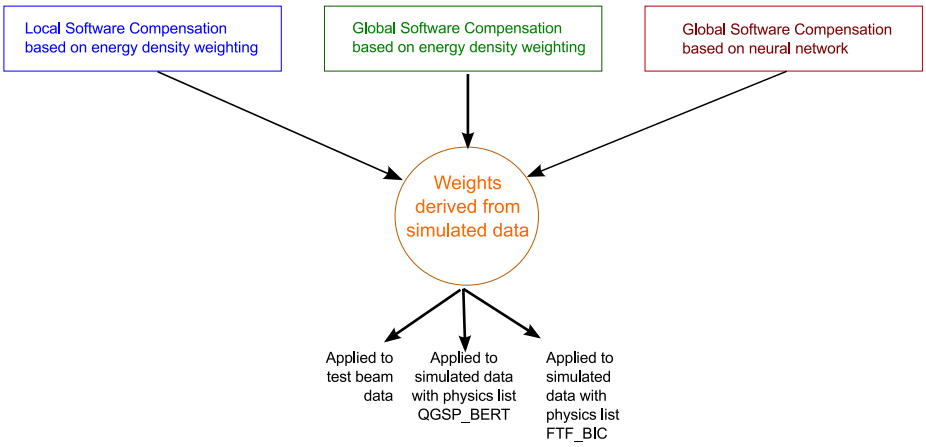

Figure 4.26: Illustration of the software compensation technique comparison, illustrated by the blue, green and red boxes.

The methods are compared for the same conditions as shown in Figure 4.26, i.e. for all techniques weights were extracted from simulated data and applied to all sets of simulated and test beam data. The sizes of the energy resolution improvements are listed in Table 4.2. It is largest for the neural network approach, followed by the local and then by the global energy density software compensation technique.
One of the main results of this thesis chapter is that all three presented software compensation methods are very successful in improving the energy resolution of test beam and simulated data. Additionally a good accuracy of the reconstructed energy was achieved. A decision about which of the presented software compensation techniques should be recommended for a usage in the future, depends on the particular application. The neural network approach led to the largest energy resolution improvement but its implementation, due to additional needed data sets, was most resource intensive. Between

Table 4.2: Comparison of different software compensation methods for weights derived from simulated data.

Weight derived from simulated data		
Local energy density SC	Global energy density SC	Neutral Network SC
• Average energy resolution improvement 20 % for test beam and 25 % for simulated data	• Average energy resolution improvement 18 % for test beam and 22 – 25 % for simulated data • Almost no beam energy dependence of energy resolution improvement of test beam data	• Average energy resolution improvement 22 % for test beam and 30 % for simulated data

the two methods based on energy density, the local method achieved a better energy resolution improvement. Furthermore it used the full capacity of the calorimeters' fine granularity. However, the global energy density weighting approach led a constant improvement over the full applied energy range.

- Second, the performance with weights derived from test beam data and from simulated data is compared.
  As illustrated schematically in Figure 4.27 this only includes techniques directly using the energy density. In case of simulated data the comments include both physics lists from which weights were derived.
  It can be concluded that the software compensation gives the best performance for both energy reconstruction accuracy and energy resolution, if the weights were applied to the same data sample type as the weights were extracted from, which is an expected result. It is important to stress that it is a great success that software compensation using weights extracted from simulated data also result in a significant improvement of resolution when applied to test beam data and vice versa. Obviously, the goodness of the results dependence on how accurate the simulated data described the test beam data in the first place. Models should describe data well on both the microscopic level, like local energy densities, and on shower shape level. There are ongoing activities between the CALICE collaboration and the developers of the hadronic models of Geant4 to improve the physics lists further. This is done on the side of the CALICE collaboration

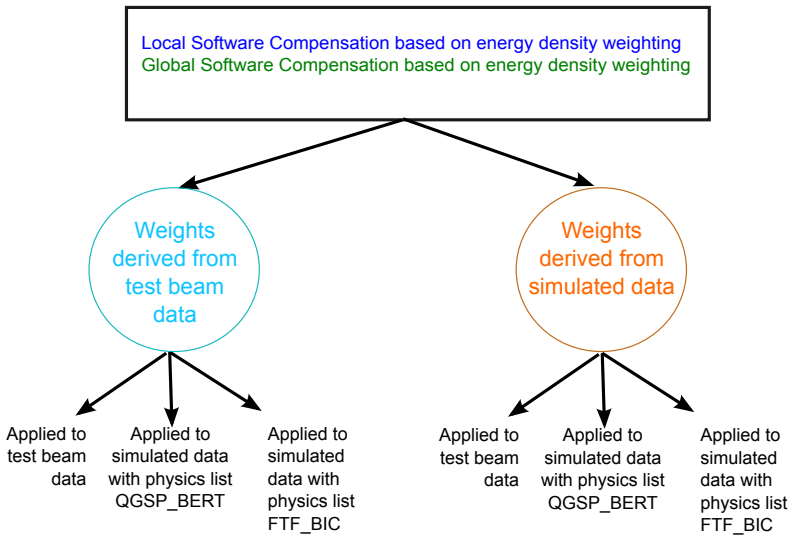

Figure 4.27: Illustration of test beam data and simulated data weight parameterization, illustrated by the light blue and orange circles.

through the comparison of many different shower variables of test beam data with simulated data using the available physics lists. The Geant4 developers, on the other hand, try to tune and adjust the implementation of their hadronic model descriptions to achieve a better agreement of test beam and simulated data.

- Third, the two physics list are compared with each other, as illustrated in Figure 4.28. It should be noted that it was not the goal of this thesis to study the performance of different physics lists. In that case, many more variables and physics lists should have been evaluated. Nevertheless, two physics lists were chosen to be presented in this thesis. Simulated data with physics list QGSP_BERT led to a better description of the initial energy resolution of test beam data. The initial reconstructed energy was better described by simulated data with the physics list FTF_BIC.
  For the software compensation, weights extracted from simulated data of both physics lists achieved similar results for the energy resolution of test beam data. Using weights extracted from simulated data can lead to a bias in the reconstructed energy of test beam data. However, it was shown that this can easily be corrected. Furthermore, weights which were extracted from simulated data with the physics list FTF_BIC gave better results for the linearity than weights which were extracted from simulated data with the physics list QGSP_BERT. Also, the energy resolution improvement of simulated data was larger for all techniques with the physics list FTF_BIC. Thus, it can be concluded that FTF_BIC is slightly favored for the application in software compensation techniques.

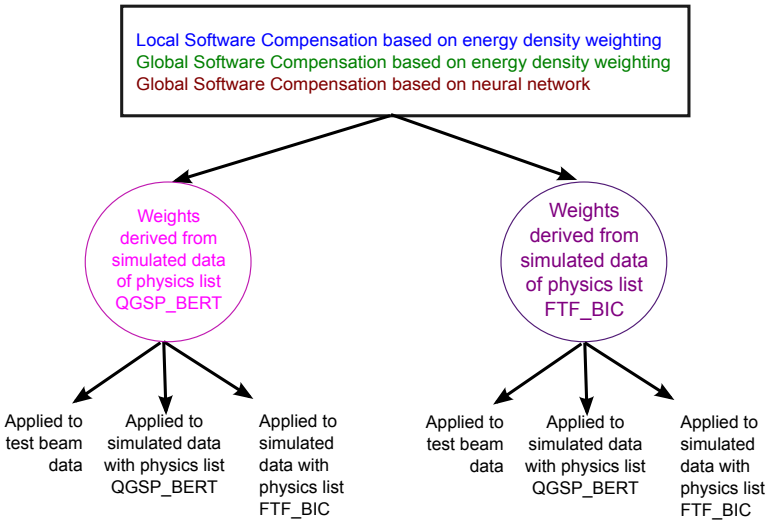

Figure 4.28: Illustration of physics list comparison, illustrated by the pink and purple circles.

However, the most important conclusion is that the large improvement in energy resolution was only achievable due to the construction of the calorimeter itself. Its high granularity made it possible to have a much better description of hadronic showers, since it provides a detailed three-dimensional picture of hadronic showers. For example, a software compensation technique for the CMS hadronic calorimeter led only to an energy resolution improvement of approximately 8 % [77]. The ATLAS hadronic calorimeter reached an energy resolution improvement due to calibration methods which included software compensation, dead material corrections, clustering corrections and other corrections for an imperfect reconstruction of $<$20 % [78], compared to resolution improvements of up to 25 % obtained here with software compensation alone.

Chapter 5

Software Compensation in the CLIC_ILD and ILD detectors

The detectors developed and constructed by the CALICE collaboration are prototype detectors for the ILD and SiD detector systems of both ILC and CLIC, in the latter case called CLIC_ILC and CLIC_SiD. The analog hadron calorimeter with steel absorber plates, described in Section 4.1, represents the prototype for the ILD hadronic calorimeter. A prototype for the hadronic calorimeter for CLIC was recently built by the CALICE collaboration, taking the active layers and readout from the AHCAL and replacing the approximately 2 cm thick steel plates with 1 cm thick tungsten absorber plates.
In the previous chapter it was shown that software compensation improves the single particle energy resolution in the hadronic prototype calorimeter. Thus, it is an obvious step to implement software compensation in the event reconstruction software of ILD and accordingly CLIC_ILD.
This chapter presents first, in Section 5.1, the studies on necessary requirements for software compensation in ILD and CLIC_ILD. The second part, in Section 5.2, focuses on the energy resolution improvement for single hadrons and jets in the ILD calorimeter.

5.1 Calorimeter response to electrons and pions of ILD and CLIC_ILD

Software compensation works through the offline equalization of electromagnetic and hadronic detector response. It only can help to improve the energy resolution if the e/π ratio, introduced in Chapter 3, is not equal to unity and differs by a large enough amount. Since the geometry and material of active and passive layers in the ILD detector design is comparable the one of the prototype, it is expected that the $e/\pi \neq 1$ for the ILD hadronic calorimeter in simulations[1], too. In case of the CLIC_ILD hadronic calorimeter, this ratio is not a priory known, since a tungsten absorber, compared to steel like in the ILD case, will change the detector response. Therefore, a simulation study for its determination, as a necessary requirement for the feasibility of software compensation, was performed.
The study was based on the simulation and reconstruction of e^- and π^- events at two energies

[1] and eventually in reality

(10 GeV and 30 GeV). In Section 3.4 is was explained that the electromagnetic fraction in hadronic showers increases for higher energies. Therefore the fraction of invisible to incoming particle energy decreases with higher particle energy and the e/π differs less from unity. Thus, the difference of electromagnetic and hadronic detector response should be largest for lower energies and it is sufficient to determine the ratio in the lower energy range.
The events were simulated with detector models of ILD and CLIC_ILD. The creation point of the particles was placed between the electromagnetic and the hadronic calorimeter in the central barrel region, since only the detector response of the hadronic calorimeter, needed to be investigated. To test whether the results were simulation model dependent, two sets of events with different physics lists (QGSP_BERT and FTF_BIC) were simulated. QGSP_BERT is the default physics list for high energy experiments. Another physics list (FTF_BIC) was included to check for possible effects which are hadronic model dependent. The reconstruction was performed with the official reconstruction software[2]. An event picture of such a single particle shower is shown in Figure 5.1.

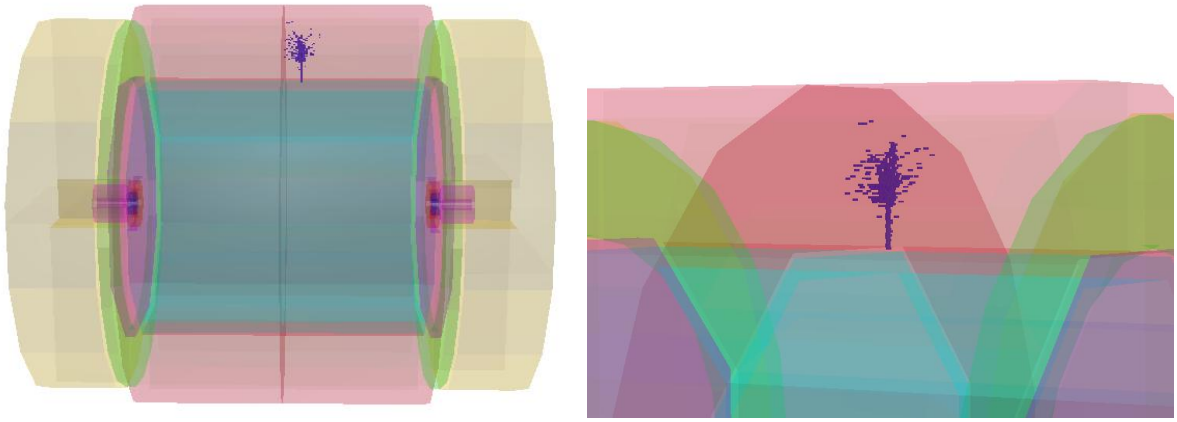

Figure 5.1: Event picture of a pion of 30 GeV in the barrel of the CLIC_ILD hadronic calorimeter. The creation point of the particle was between the electromagnetic and hadronic calorimeter. (*left:*) Full detector. (*right:*) Hadronic calorimeter.

The output of the Particle Flow reconstruction are objects with a reconstructed energy based on the same calibration scale, since both particle types are treated as hadrons. The distributions of the reconstructed cluster energy was fitted with a Gaussian for all settings (particle type, particle energy, detector model, physics list). The mean value of the fitted Gaussian corresponds to the reconstructed energy. By comparing the reconstructed energies for electrons and pions the e/π ratios were calculated, shown in Table 5.1 for the CLIC_ILD detector and in Table 5.2 for the ILD detector.
The simulation of the hadronic calorimeter response of CLIC_ILD shows an e/π ratio of

[2]One change to the default PandoraPFA settings had to be applied. See Section B.2 for more detail.

Table 5.1: Detector response to simulated electron and pion events in the CLIC_ILD hadronic calorimeter with the physics lists QGSP_BERT and FTF_BIC. Both particle types are reconstructed with the same calibration values.

Detector: ILD for CLIC				
	FTF_BIC		QGSP_BERT	
particle energy	10 GeV	30 GeV	10 GeV	30 GeV
	E_{rec}	E_{rec}	E_{rec}	E_{rec}
e^-	11.89 ± 0.01 GeV	35.07 ± 0.03 GeV	11.86 ± 0.01 GeV	35.07 ± 0.03 GeV
π^-	10.67 ± 0.02 GeV	33.48 ± 0.04 GeV	11.38 ± 0.02 GeV	36.33 ± 0.04 GeV
e/π ratio	1.14 ± 0.002	1.047 ± 0.002	1.042 ± 0.002	0.965 ± 0.001

Table 5.2: Detector response to simulated electron and pion events in the ILD hadronic calorimeter with the physics lists QGSP_BERT and FTF_BIC. Both particle types are reconstructed with the same calibration values.

Detector: ILD for ILC				
	FTF_BIC		QGSP_BERT	
particle energy	10 GeV	30 GeV	10 GeV	30 GeV
	E_{rec}	E_{rec}	E_{rec}	E_{rec}
e^-	14.42 ± 0.01 GeV	43.57 ± 0.03 GeV	14.43 ± 0.01 GeV	43.59 ± 0.03 GeV
π^-	10.33 ± 0.03 GeV	34.38 ± 0.07 GeV	10.68 ± 0.03 GeV	36.62 ± 0.06 GeV
e/π ratio	1.396 ± 0.004	1.267 ± 0.003	1.351 ± 0.004	1.190 ± 0.001

almost unity for the hadronic physics model of QGSP_BERT. Thus, the electromagnetic and hadronic response of the detector are nearly the same and nothing has to be corrected. For the hadronic model of FTF_BIC the ratios are bigger, but still to small to expect that a large energy resolution improvement due to the usage of software compensation could be achieved. The simulation results for the tungsten calorimeter are quite surprising, since the geometry was not constructed in the view of compensation. There are two possible explanations for the result: Either the material and geometry of hadronic calorimeter of CLIC_ILD gives indeed an

e/π ratio close to one and the calorimeter is self-compensating or the simulation of particles in tungsten with Geant4 is not adequate. For clarification, the currently designed hadronic CALICE prototype with tungsten absorber layers is going through an extensive test beam campaign, which started in September 2010 at the CERN SPS. The data is currently analyzed and a simulation model is under construction. Once the test beam data is understood and the simulations are validated, the e/π ratio can be calculated for test beam data and simulation, and decided, which hadronic model describes the data best.
The hadronic calorimeter of ILD shows an e/π ratio of around 1.2 – 1.4. This value is large enough to assume that a software compensation algorithm could be used to improve the energy reconstruction.

5.2 Software Compensation in PandoraPFA

The results of the previous section indicated that the energy reconstruction and energy resolution of hadrons in the ILD detector can be improved due to software compensation. The determination and implementation of such an approach into the PandoraPFA reconstruction method is described in Subsection 5.2.1. The method, which was chosen to be applied, is the local software compensation technique described in the previous chapter. In Subsection 5.2.2 the results of the software compensation technique in the hadronic calorimeter of ILD are stated and explained for single hadrons. However, the aim of PandoraPFA is an excellent jet energy resolution. Therefore in Subsection 5.2.3 the jet energy resolution performance of PandoraPFA with an implemented software compensation technique is shown.

5.2.1 Implemenation

For typical events PandoraPFA determines only the energy of neutral hadronic particles from the measured cluster energy in the calorimeter system. Charged hadronic particles create also a measurable signal in the tracking systems, thus, their energy is estimated from the reconstructed track information. A general overview about the motivation of PandoraPFA was given in Section 2.5. More details, especially on the different steps of the PandoraPFA algorithm, can be found in the Appendix B.1.
The method of local software compensation was chosen to be implemented into the PandoraPFA framework, with a weight determination described analog to Section 4.3. As a first step and since typically only the energy of neutral hadrons is measured in the hadronic calorimeter, a weight parameterization was extracted from neutral hadron events.
For the weight parameterization single neutral particle (K_0 and n) events were simulated in the energy range between 10 – 95 GeV. The events were generated with a particle production at the interaction point and with flight directions to all possible positions in the central barrel region. The same detector geometry of ILD as in Subsection 5.1 was used, together with the hadronic physics model QGSP_BERT. After the event reconstruction the output of the

particle flow algorithm is a single particle flow object, classified as a neutral particle with one associated cluster and no associated tracks. For these objects, the hit energy density was calculated and divided in energy density bins. For some events the hadronic shower was not contained in the hadronic calorimeter, but started already in the electromagnetic calorimeter. Therefore two sets of energy density bins were determined, for hits in the electromagnetic and the hadronic calorimeter. Analog to the approach of the local software compensation technique, described in Section 4.3.1, the weight function was parameterized in an iterative minimization procedure.
These parameterized weights are applied to hits in clusters of neutral hadronic particle flow objects. The performance of such an application is shown for single particles in Subsection 5.2.2 and for jets in Subsection 5.2.3.

5.2.2 Single particle energy resolution with software compensation in ILD

A weight parameterization based to the local hadron compensation technique described in Section 4.3 for hits in the electromagnetic and hadronic calorimeter was determined for neutral hadrons, as explained in the previous subsection. To test these weights on a statistically independent data sample a new set of neutral K_L events was simulated[3] in the energy range of 10 – 95 GeV. The particle creation point was placed between the electromagnetic and hadronic calorimeter to only be sensitive to effects in the hadronic calorimeter.
The reconstructed energy and energy resolution of these events was determined with and without software compensation and is shown in Figure 5.2. The error bars of the points illustrate the statistical error only. For the energy reconstruction without software compensation an offset is visible over the full energy range of approximately 20 % with a spread of 25 %. This is due to the use of non-perfect calibration values. More details relating this issue can be found in the Appendix Section B.2. With weighting, the energy reconstruction accuracy improved over the whole energy range, although on offset of approximately 13 % with a spread of 20 % is still present. The energy resolution improvement is clearly visible over the full energy range with improvements of 12 – 30 %.

The same test was applied to a second set of single K_L events which were created at the interaction point of the ILD detector in the same energy range of 10 – 95 GeV with flight directions to all possible positions in the barrel. The energy resolution degraded, which can be explained by the fact that dead material between the electromagnetic and hadronic calorimeter lead to particle energy loss, which could not be determined. For the application of software compensation is was required that the larger part of the cluster energy was deposited in the hadronic calorimeter than in the electromagnetic calorimeter. Therefore, the energy resolution

[3] Software versions can be found in B.3.

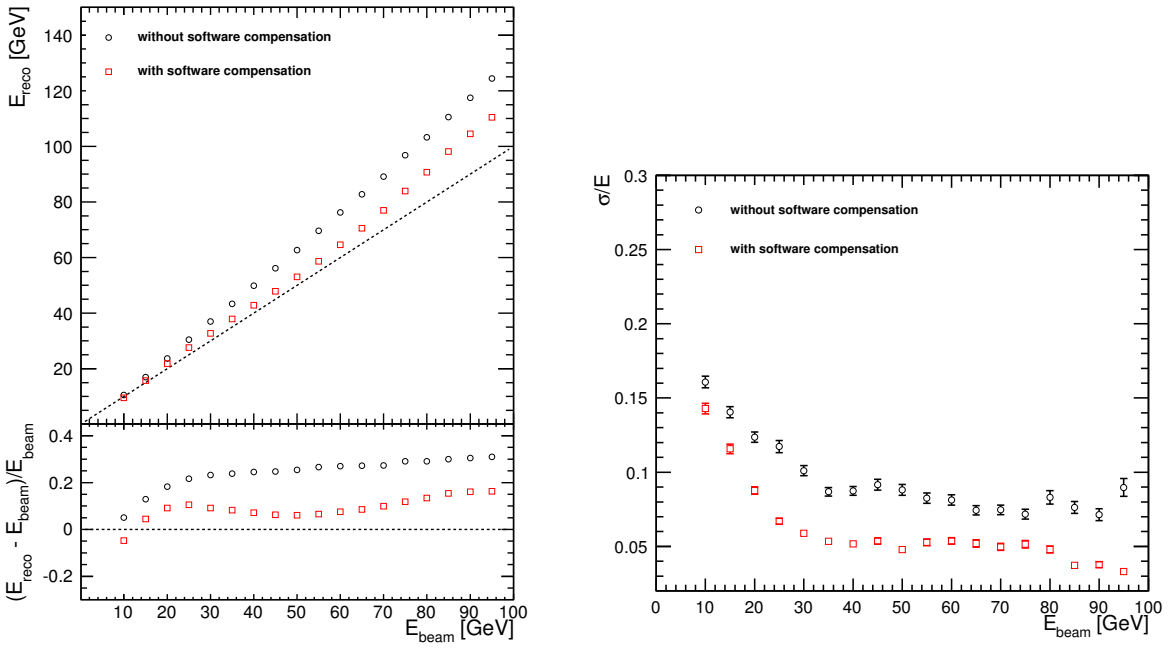

Figure 5.2: Detector response (*left*) and energy resolution (*right*) for neutral kaons with and without software compensation in the ILD detector. The particle were created in the gap between the electromagnetic and hadronic calorimeter.

shows approximately the same improvement due to software compensation, as for particles, which only traverse and lose energy in the hadronic calorimeter.

5.2.3 Jet energy resolution with software compensation in ILD

Due to the successful energy resolution improvement of single neutral hadrons, as shown in the previous subsection, and because PandoraPFAs main goal is to achieve an excellent jet energy resolution, the software compensation technique was tested on events with jets. For a typical multi-particle event a software compensation algorithm can be applied to clusters at two stages in the PandoraPFA algorithms (more detail can be found in the Appendix B.1). The first one is the application to neutral hadrons once particle flow object are created, which is equal to the approach explained in the previous subsection. Another possibility is to apply the software compensation technique inside the PandoraPFA clustering and reclustering algorithms as a so called cluster energy correction function. The correction would be applied to all hadronic clusters and therefore may change the construction of particle flow objects, i.e. their track and cluster composition. However, if the energy correction function does not lead to a different particle flow construction, the reconstructed energy of a charged hadron will not be changed compared to the default PandoraPFA usage.

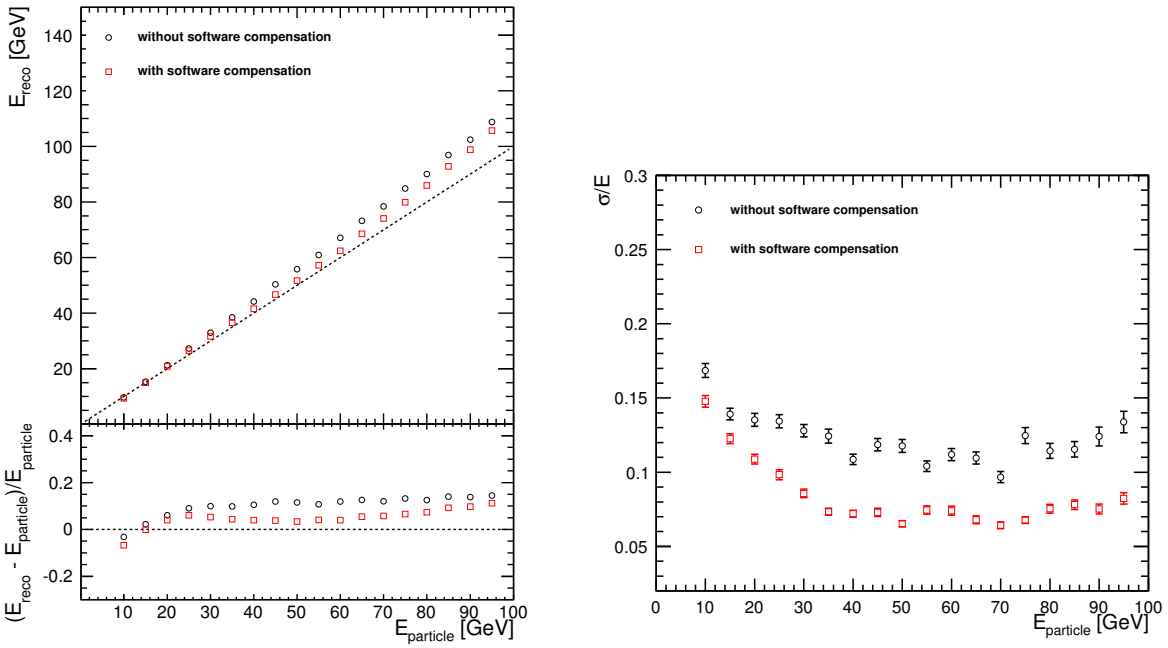

Figure 5.3: Detector response (*left*) and energy resolution (*right*) for neutral kaons with and without software compensation in the ILD detector. The particle were created at the interaction point.

Since the largest amount of energy in the hadronic calorimeter is deposited by charged hadrons, weights for the energy correction function using software compensation were extracted from charged single hadron events ($\pi^{+/-}$). The weight extraction was performed analog to the one of neutral hadrons via single particle event generation in the energy range between 10 – 95 GeV.

For the weight application and thus to provide a first proof that software compensation is a useful method for the energy correction in the ILD detector, jets of particles were simulated and reconstructed with different settings for PandoraPFA (no software compensation, software compensation only for neutral hadrons, software compensation for neutral hadrons and for all hadrons inside the clustering algorithms). The jet events were simulated using generator files of the following configuration: $e^+e^- \rightarrow Z/\gamma^* \rightarrow q\bar{q}$ (only light (u,d,s) quarks). Four sets of events were created with center-of-mass energies of 91 GeV, 200 GeV, 360 GeV and 500 GeV, to have different jet energies available. The results of the jet energy resolution for the different settings are listed in Table 5.3 and are explained in the following. For a center-of-mass energy of 200 GeV the reconstructed di-jet energy is shown in Figure 5.4.

The first part of the table shows the results for the jet energy resolution for the default

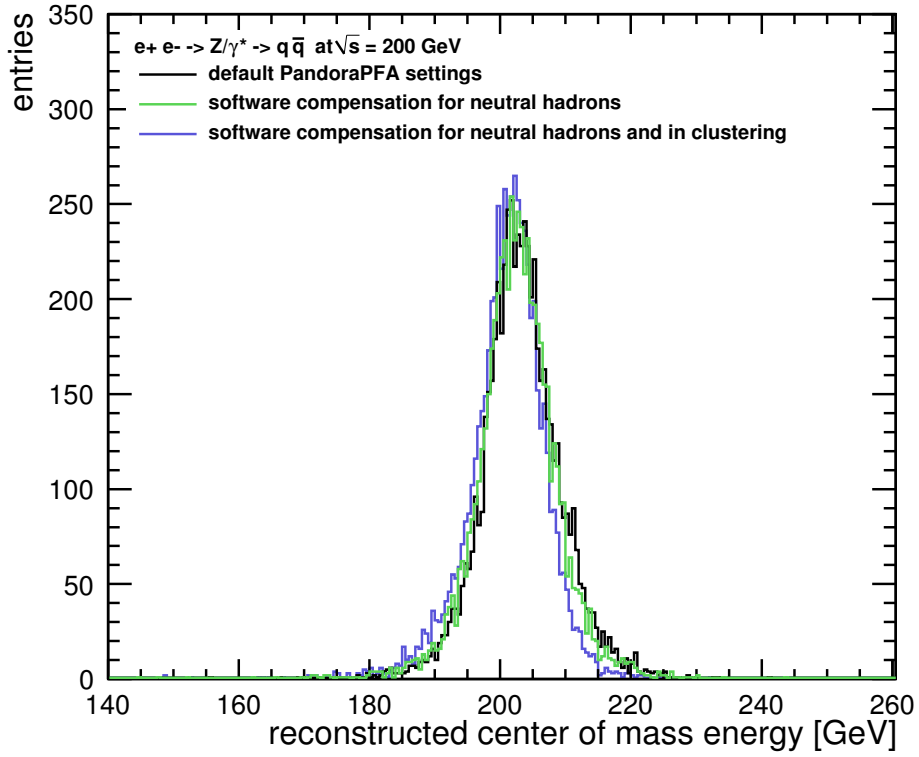

Figure 5.4: Reconstructed di-jet energy of the process $e^+e^- \to Z/\gamma^* \to q\bar{q}$ at $\sqrt{s} = 200\,\text{GeV}$ with and without software compensation in the particle flow algorithm PandoraPFA. The black line shows the jet reconstruction for the default PandoraPFA settings. The di-jet energy for software compensated energies of neutral hadrons in the PandoraPFA reconstruction is illustrated by the green line. The blue line shows the result for software compensation of neutral and charged hadrons in the clustering and reclustering algorithm.

settings of PandoraPFA, i.e. no software compensation was applied. Results are divided in the reconstructed di-jet energy E_{jj}, the overall rms(E_{jj}) of the di-jet energy, the rms$_{90}(E_{jj})$, which is defined as the rms in the smallest range of reconstructed energy which contains 90 % of the events, and the final single jet energy resolution rms$_{90}(E_j)/E_j$.
PandoraPFA always quotes the rms$_{90}$ as a reference of the jet energy resolution instead of the width of a Gaussian or the overall rms. The reconstructed di-jet energy, shown for $E_{jj} = 200\,\text{GeV}$ in Figure 5.4, cannot be described well by a Gaussian, because of non-perfect reconstructed events, which populate the tails. Quoting the rms, as a measure of the jet energy resolution, overemphasizes the importance of these tails. Thus, the term rms$_{90}$, which parametrizes the bulk of the events and is robust and relatively insensitive to the tails, is used instead.
The second part of Table 5.3 shows the results for a software compensation algorithm applied

Table 5.3: Reconstructed jet energy and jet energy resolution for different PandoraPFA settings (Default: no changes in the default PandoraPFA settings; SC: software compensation for neutral hadrons; SC-EC: software compensation for neutral hadrons and inside the clustering and reclustering algorithms for all hadrons). The the fractional jet energy resolution for a single jet is $\mathrm{rms}_{90}(E_j)/E_j$, where $\mathrm{rms}_{90}(E_j) = \mathrm{rms}_{90}(E_{jj})/\sqrt{2}$. The improvement is defined as the relative difference between the software compensation result and the default PandoraPFA setting.

E_{cms}	90 GeV	200 GeV	360 GeV	500 GeV
Default				
E_{jj} [GeV]	92.1468	203.096	365.749	508.777
$\mathrm{rms}(E_{jj})$ [GeV]	3.42198	6.27993	12.1937	17.6334
$\mathrm{rms}_{90}(E_{jj})$ [GeV]	2.42726	4.42869	8.29062	12.0325
$\mathrm{rms}_{90}(E_j)/E_j$	3.73±0.05	3.08±0.04	3.21±0.04	3.34±0.05
Software compensation for neutral hadrons				
E_{jj} [GeV]	92.2585	202.294	367.072	513.322
$\mathrm{rms}(E_{jj})$ [GeV]	3.27827	6.48737	13.9508	24.544
$\mathrm{rms}_{90}(E_{jj})$ [GeV]	2.34271	4.36875	9.14467	14.1477
$\mathrm{rms}_{90}(E_j)/E_j$	3.59±0.05	3.05 ± 0.04	3.52±0.05	3.90±0.06
Improvement [%]	3.6	1.0	-9.7	-16.8
Software compensation as an energy correction function and for neutral hadrons				
$\mathrm{E}_{\mathrm{rec}}$ [GeV]	92.0609	201.614	362.28	502.738
$\mathrm{rms}(E_{jj})$ [GeV]	3.23298	6.21553	13.637	21.4374
$\mathrm{rms}_{90}(E_{jj})$ [GeV]	2.29363	4.13729	8.62862	12.9567
$\mathrm{rms}_{90}(E_j)/E_j$	3.52±0.05	2.90±0.04	3.37±0.05	3.64±0.06
Improvement [%]	5.3	5.8	-5.0	-9.0

to neutral hadrons. The improvement is significant for low energies. It should be noted that also the actual value of the di-jet energy is reconstructed closer to the generated value. The overall rms is larger for most energies compared to the default settings (except for $\sqrt{s}$ =91 GeV). This leads to the conclusion that not correctly reconstructed events cannot be corrected via software compensation. The probable reason for an incorrect reconstruction is confusion, i.e. the incorrect cluster and track to particle matching. This is not a weakness of the software compensation, instead, ideally other algorithms have to take care for the correct track to cluster assignment and therefore particle flow object creation. For even higher energies no improvement is seen due to software compensation, in fact the jet energy resolution even degrades. This result is not surprising in view of the breakdown of contributions to the PandoraPFA resolution, given in Table 5.4. It shows the jet energy resolution for the following jet energies: 45, 100, 180, 250 GeV. These jets were simulated with in $e^+e^- \to Z/\gamma^* \to q\bar{q}$

(only light (u,d,s) quarks) events and are therefore directly comparable to the results presented in Table 5.3. The values of the total jet energy resolution differ due to the use of different tracking software packages. Between a center-of-mass energy of 200 GeV and 360 GeV the most significant term for the total jet energy resolution changes from calorimeter resolution to confusion. Thus, if the confusion is the dominant term in the overall jet resolution, a change in the calorimeter resolution will not change the overall resolution significantly. Another reason might be that a significant change in the overall energy estimation, because single neutral hadrons with relatively high energies are reconstructed to a different energy with software compensation, would require the modification of the overall calibration to get an improved jet energy reconstruction.

Table 5.4: Values taken from [58]. The particle flow jet energy resolution obtained with PandoraPFA broken down into contributions from: intrinsic calorimeter resolution (for photons and neutral hadrons), imperfect tracking, leakage and confusion.

Contribution	Contribution Jet Energy Resolution rms90$(E_j)/E_j$			
	E_j =45 GeV	E_j =100 GeV	E_j =180 GeV	E_j =250 GeV
Total	3.7%	2.9%	3.0%	3.1%
Resolution	3.0%	2.0%	1.6%	1.3%
Tracking	1.2%	0.7%	0.8%	0.8%
Leakage	0.1%	0.5%	0.8%	1.0%
Other	0.6%	0.5%	0.9%	1.0%
Confusion	1.7%	1.8%	2.1%	2.3%

The results for an additional energy correction on the basis of software compensation for all hadronic clusters is shown in the last part of Table 5.3. For the center-of-mass energies of 91 GeV and 200 GeV the jet energy resolution can be improved further. At even higher jet energies the cluster correction function based on software compensation is still degraded compared to the default jet energy resolution.

5.3 Summary

Overall the results give a proof of principle that software compensation is a realistic and successful algorithm to improve the jet energy resolution in the PandoraPFA jet reconstruction. For a full integration of software compensation into the ILD reconstruction software (PandoraPFA) the weight extraction would need to be automatized, which was not the focus of this thesis. Since the ILD detector and reconstruction is constantly improved, the weight parameterization would need to be renewed for changes in detector geometries, but not if details in the PandoraPFA algorithm would change, since the weights depend on the physics

of hadronic showers and not on the reconstruction method.
Compared to this “proof of principle study“ there are a couple of points which could be improved in a further analysis. For example, the role of the electromagnetic calorimeter has not been throughly investigated yet. It should be studied if software compensation can improve the energy determination for hadrons with a main energy deposition in the electromagnetic calorimeter. Following this question it should be studied if weights should include the electromagnetic calorimeter or if software compensation should only be applied if the main energy deposition of a particle is in the hadronic calorimeter. Also it could be studied if PandoraPFA provides an estimate for the goodness of cluster and track to particle association, to be able to excluded events with an incorrect cluster formation from the software compensation technique. This would prevent a degradation of the jet energy reconstruction of events, which populate the tails of the di-jet energy distribution.

Chapter 6

Top Quark Mass Measurement

The proposed accelerator CLIC and one of its detector options, namely CLIC_ILD, have been introduced in Chapter 2. A conceptual design report (CDR) has been written in 2011 and will be published in early 2012. The analysis presented in the following is one of the benchmark processes of this CDR and is a top quark mass and width determination from the process $e^+e^- \to Z/\gamma^* \to t\bar{t}$, based on the kinematic reconstruction of the top quark decay products.
The top quark plays a unique role in particle physics. Due to its high mass, it is particularly sensitive to new physics and is intimately connected to the mechanism of electroweak symmetry breaking. It has a sizable impact on the Higgs boson mass through radiative corrections, and, together with the W boson mass, drives electroweak predictions for the Higgs mass. Due to its short lifetime the top quark decays before hadronizing, offering the unique opportunity to study a bare quark by accessing its properties directly through its decay products. Top quarks decay exclusively through electroweak processes, into a real W boson and a down-type quark. Due to the large V_{bt} CKM matrix element ($V_{bt} = 0.9992$ [79]), the decay is almost exclusively into a W boson and a b quark.
To date, top quarks have been observed at the Tevatron and at the LHC. At present, the best measurement of the mass is provided by the Tevatron, with a statistical error of 0.6 GeV. The measurement is already limited by systematics, with a total systematic error of 0.75 GeV [80]. Early LHC analyses obtained statistical errors on the order of 1 GeV to 2 GeV, with systematic errors close to 3 GeV [81, 82]. With increasing integrated luminosity, significant improvement is anticipated, but the systematics are expected to remain substantial due to the challenging environment of hadron colliders and due to theoretical uncertainties [11]. It should be noted that what is called the top mass in the hadron collider studies as well as in this analysis should theoretically be called the peak position of the top pole mass, as discussed in Chapter 1. However, in the following this mass is referred to as Breit-Wigner or top mass.
Due to the cleaner experimental environment at an e^+e^--collider, such as CLIC, and combined with the expected jet energy and track momentum resolution of linear collider detectors, a significant improvement for such a measurement is expected. The presented analysis is based on the experimental environment at CLIC, which has a design center-of-mass energy of 3 TeV. However, this benchmark process was performed at $\sqrt{s}$ =500 GeV, because CLIC is proposed to be built in stages, starting at center-of-mass energy of 500 GeV, while the construction is under way for the higher energy phases. Another motivation is to study how precisely the top quark mass can be determined considering the more severe background conditions at CLIC compared to the ILC, as discussed in Section 2.4. For the ILC, the studies with full

detector simulations have shown that statistical errors below 100 MeV can be achieved for integrated luminosities of 100 fb^{-1} at $\sqrt{s} = 500$ GeV for a top mass measurement via top pair production.
Related to this thesis, which so far focused on the energy reconstruction of hadrons, the measurement of the top quark mass is also interesting in view of the hadronic calorimeter. The top quark mass will be measured in the fully-hadronic ($e^+e^- \to t\bar{t} \to q\bar{q}bq\bar{q}b$) and semi-leptonic ($e^+e^- \to t\bar{t} \to q\bar{q}bl\nu_l b$) decay channels, thus the quarks of the decay products in both channels will create jets, requiring good jet reconstruction for precise measurements.

6.1 Experimental Conditions at a 500 GeV CLIC Collider

In the present analysis, the top quark mass is measured in the environment of a 500 GeV CLIC machine, which is directly comparable to the baseline design of the ILC. The use of different technologies compared to the ILC acceleration technique leads to differences in the experimental environment, which could potentially have a negative impact on the physics performance.
The most important parameter here is the time between bunch crossings within a bunch train, which is 0.5 ns in the case of CLIC, while it is 356 ns or 670 ns in the case of the ILC, depending on the adopted design. For typical detector integration times of the order of a few to 100 ns, the short bunch crossing time leads to the pile-up of background from many bunch crossings over the 177 ns long bunch trains. In addition, the smaller beam spot size at CLIC leads to increased beamstrahlung and correspondingly larger energy spread, with ∼61% of the total luminosity within 1 % around the peak of the center-of-mass energy distribution, compared to ∼72% at the ILC. This translates into larger uncertainties when using energy or momentum constraints along the beam axis.
The radiated beamstrahlung photons lead to a creation of coherent and incoherent e^+e^--pairs as well as incoherent quark pair production, which results in hadronic events. As discussed in Section 2.4, only the hadronic background affects the event reconstruction, in particular the jet energy measurements. At a 500 GeV CLIC machine, 0.19 $\gamma\gamma \to$ hadrons events per bunch crossing are expected, with an average energy of 13.3 GeV. Approximately 3.4 GeV of this energy is deposited in the calorimeter system, 0.2 GeV out of this in the barrel detectors [83].
The detector model used in the present study is a variant of CLIC_ILD [84], a detector concept based on particle flow event reconstruction with PandoraPFA, introduced in Section 2.3.1. At 500 GeV, the background is significantly reduced compared to the 3 TeV case, permitting modifications of the detector to optimize its performance for the lower collision energy. In particular the innermost vertex detector layer for CLIC_ILD can move in by 6 mm to a radius of 25 mm, improving flavor tagging at low momentum.
The minimization of the impact of the hadronic background requires strict timing cuts on the reconstructed particles to limit the influence of out-of-time contributions. Here, timing in the calorimeters is of particular importance.

6.2 Event Generation, Simulation and Reconstruction

The signal process studied in this note is top quark pair production, $e^+e^- \to Z/\gamma^* \to t\bar{t}$, which, at a 500 GeV CLIC collider, has a cross section of approximately 528 fb. The top quark decays almost exclusively into a W boson and a b quark. The signal events can thus be grouped into different classes, according to the decay of the W bosons. These are the *fully-hadronic* channel, with both W bosons decaying into quark pairs, the *semi-leptonic* channel, with one W boson decaying into quarks, the other into a lepton and the corresponding neutrino, and the *fully-leptonic* channel, with both W bosons decaying into lepton and neutrino. The branching ratios of the top quark pair decay channels are listed in Table 6.1. In the leptonic channels, the decay into a τ lepton and a neutrino is a special case, since the τ decays almost instantly into either a lepton and two neutrino (branching ratio of 35 %) or into one or more hadrons and a neutrino (branching ratio of 65 %), giving rise to additional missing energy in the final state, and potential confusion with hadronic decay modes.

Table 6.1: Branching ratios of the top quark decay channels.

Event class	$t\bar{t} \to WbWb$	branching ratio
fully-hadronic	$\to q\bar{q}bq\bar{q}\bar{b}$	46 %
semi-leptonic	$\to q\bar{q}bl\nu_l\bar{b}$	45 %
fully-leptonic	$\to l\nu_l bl\nu_l\bar{b}$	9 %

In the analysis, only fully-hadronic and semi-leptonic events, excluding τ final states, were selected since those provide the best possible mass measurement. However, to account for imperfect event classification, all possible decay modes of the $t\bar{t}$ pair were generated according to their branching fractions and included in the generated signal event sample. The top mass and width were fixed for the signal event sample to $m_{\mathrm{bw}} = 174.0\,\mathrm{GeV}$ and $\sigma_{\mathrm{bw}} = 1.37\,\mathrm{GeV}$. A second set of $e^+e^- \to t\bar{t}$ events were generated with the same top mass and width as the signal sample. This second sample was necessary for the final fit of the top mass distribution, as described in Section 6.3.7.

Besides the signal, background processes with similar event topologies have to be considered. These are mostly four and six fermions final states, with the high cross-section quark pair production in addition. Table 6.2 lists the studied processes, with approximate cross sections at a 500 GeV CLIC machine, and the corresponding event numbers that were generated for an integrated luminosity of $100\,\mathrm{fb}^{-1}$. In addition, the processes $e^+e^- \to q\bar{q}e^+e^-$ and $e^+e^- \to q\bar{q}e\nu$, which are dominated by t-channel single boson production ($e^+e^- \to Ze^+e^- \to q\bar{q}e^+e^-$, $e^+e^- \to We\nu \to q\bar{q}e\nu$), were investigated using samples with reduced statistics. It was shown that the non-di-boson contributions are rejected completely in the analysis, thus, they were not considered in the final production of $100\,\mathrm{fb}^{-1}$.

WHIZARD 1.95 [85] was used as the default event generator for the CLIC CDR benchmark studies. Since final-states with explicitly defined intermediate states are not correctly produced,

Table 6.2: Signal and considered physics background processes, with their cross section calculated for CLIC at 500 GeV. Signal and background events were generated for and integrated luminosity of 100 fb^{-1}. Only the signal control sample with a generated top mass of 174 GeV twice the number of statistics was generated and simulated.

$\sqrt{s} = 500\,\text{GeV}$

type	$e^+e^- \rightarrow$	cross section σ	number of generated events
Signal (m_{top} =174 GeV)	$t\bar{t}$	528 fb	$5.3 \cdot 10^4$
Background	WW	7.1 pb	$7.1 \cdot 10^5$
Background	ZZ	410 fb	$4.1 \cdot 10^4$
Background	$q\bar{q}$	2.6 pb	$2.6 \cdot 10^5$
Background	WWZ	40 fb	$4.0 \cdot 10^3$
Signal control (m_{top} =175 GeV)	$t\bar{t}$	528 fb	$5.3 \cdot 10^4$
Signal control (m_{top} =174 GeV)	$t\bar{t}$	528 pb	$1.2 \cdot 10^5$

i.e. the intermediate state is generated with zero width, PYTHIA [86] was used to generate the signal process $e^+e^- \rightarrow t\bar{t}$ as well as the two background processes $e^+e^- \rightarrow WW$ and $e^+e^- \rightarrow ZZ$. The processes with explicitly given final states, without specifying intermediate particles, $e^+e^- \rightarrow q\bar{q}$, $e^+e^- \rightarrow q\bar{q}e^+e^-$ and $e^+e^- \rightarrow q\bar{q}e\nu$ were generated with WHIZARD. Since the process $e^+e^- \rightarrow WWZ$ is not implemented in PYTHIA, WHIZARD was used for its generation. For simplicity, these events were generated with zero width for the intermediate bosons, allowing to specifically defined intermediate states in WHIZARD.

For the simulation with Mokka [69], the detector model introduced in Section 2.3.1 and 6.1 was used. Three hundred bunch crossings of $\gamma\gamma \rightarrow$ hadrons events were overlaid with the signal event at the digitization stage [87]. The number of overlaid bunch crossing was higher than in the 3 TeV case since at 500 GeV more relaxed timing cuts are necessary due to the increased importance of low momentum tracks for the overall jet and event energy reconstruction. It should be noted that the sets of background rejection cuts for 3 TeV were also studied for this analysis, leading to a significant loss of true signal information. The correspondingly longer integration times of the detectors required the simulation of the background accumulated over a more extensive period. The tracking and particle flow event reconstruction, using PandoraPFA, was then performed on the overlaid event, comprising signal and beam induced background.

The background from $\gamma\gamma \rightarrow$ hadrons processes is one of the major challenges at CLIC due to the short time between to bunches of 0.5 ns inside a bunch train. Mitigation of the influence of this background requires precise time stamping to assign energy deposits to individual bunch crossings, and cuts based on the transverse momentum of particles, since the background particles are predominantly at low p_{T} in the forward and backward region of the detector. Different sets of cuts with varying severity in timing and p_{T} were applied to the reconstructed particles, which are called Particle Flow Objects by the particle flow algorithm, and stored for

further analysis. These sets were labeled *no cut*, *loose*, *default* and *tight*. The settings for the *default* timing and p_T cuts are listed in Table 6.3.

Table 6.3: *Default* Particle Flow Objects selection cuts for a center-of-mass energy of 500 GeV at CLIC.

Region	p_T *range*	Time cut
Photons		
central	$1.0\,\text{GeV} \leq p_T < 2.0\,\text{GeV}$	$t < 5.0$ nsec
$(\cos\theta \leq 0.975)$	$0\,\text{GeV} \leq p_T < 1.0\,\text{GeV}$	$t < 2.5$ nsec
forward	$0.75\,\text{GeV} \leq p_T < 4.0\,\text{GeV}$	$t < 2.0$ nsec
$(\cos\theta > 0.975)$	$0\,\text{GeV} \leq p_T < 0.75\,\text{GeV}$	$t < 1.0$ nsec
Neutral hadrons		
central	$1.0\,\text{GeV} \leq p_T < 2.0\,\text{GeV}$	$t < 5.0$ nsec
$(\cos\theta \leq 0.975)$	$0\,\text{GeV} \leq p_T < 1.0\,\text{GeV}$	$t < 2.5$ nsec
forward	$2.0\,\text{GeV} \leq p_T < 4.0\,\text{GeV}$	$t < 2.0$ nsec
$(\cos\theta > 0.975)$	$0\,\text{GeV} \leq p_T < 2.0\,\text{GeV}$	$t < 1.0$ nsec
Charged PFOs		
all	$1.0\,\text{GeV} \leq p_T < 4.0\,\text{GeV}$	$t < 10.0$ nsec
	$0\,\text{GeV} \leq p_T < 1.0\,\text{GeV}$	$t < 3.0$ nsec

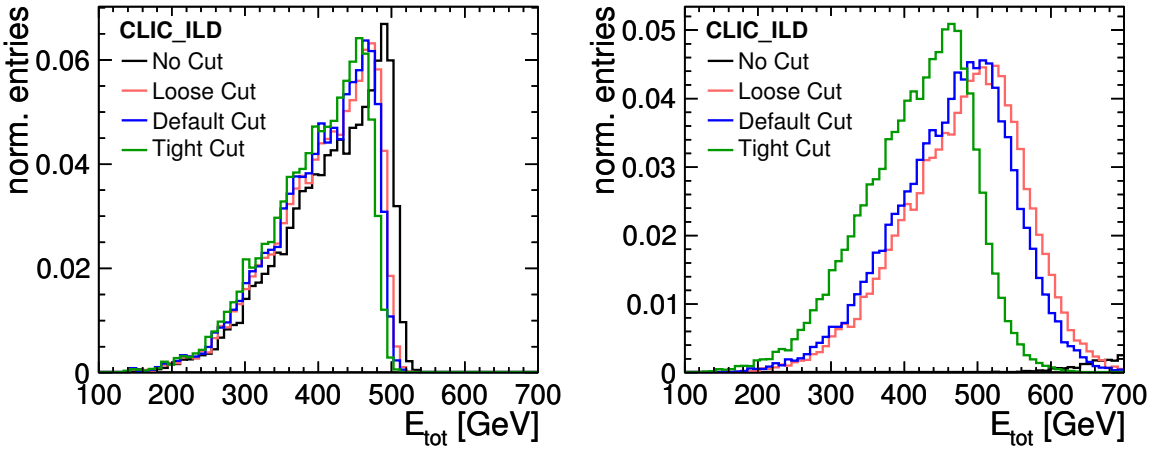

Figure 6.1: Effect of timing and p_T cuts for events without (*left*) and with overlaid $\gamma\gamma \rightarrow$ hadron events (*right*). It should be noted that with overlaid $\gamma\gamma \rightarrow$ hadron events the total measured energy distribution of all reconstructed particles, without any timing and p_T cuts, starts approximately at 600 GeV.

Figure 6.1 shows the effect of these four sets of particle flow object selections on the total visible energy in $e^+e^- \to t\bar{t}$ signal events, both for the case without and with overlaid $\gamma\gamma \to$ hadrons background. While too loose cuts result in significant pick-up of additional energy, too tight cuts lead to a loss of signal particles. Significant loss of signal energy leads to a deterioration of mass resolution due to missing information, while excessive background reduces flavor tagging efficiency, in addition to negative effects on the mass resolution. Figure 6.1 on the right shows the tight cuts result in a too small peak value of the total reconstructed energy. From further detailed studies of the different cut sets, the *default* cut option was chosen[1]. In the following the data sample with *default* background rejections cuts is meant when speaking of events with overlaid $\gamma\gamma \to$ hadron events.

6.3 Data Analysis

The data analysis proceeds in several steps, described in the following. In general, the present analysis scheme is similar to the $t\bar{t}$ analysis performed for the ILD Letter of Intent [88, 89]. Due to a more general input sample including semi-leptonic τ events as well as fully-leptonic events, and due to the different bunch and beam structure of the CLIC machine, some additional steps had to be introduced and major strategy changes had to be adopted for other steps. In general, the analysis was optimized to provide precise measurements of the top quark mass and width, favoring strict rejection of imperfectly reconstructed events over the maximization of reconstructed top quark candidates. This is an important aspect and will be further explained in Subsection 6.3.5.
As a first step, the *Lepton Finder*, see Subsection 6.3.1, was used to classify all events as fully-hadronic (no isolated lepton found), semi-leptonic (exactly one isolated lepton found) or fully-leptonic (at least two isolated leptons found), according to the number of isolated leptons found. Events classified as fully-leptonic were rejected, while the other two classes were clustered into four or six jets, according to their number of quarks in the event class, as described in Subsection 6.3.2. Following this, a *Flavor Tagging* algorithm was used, to identify the two jets originating from b quarks, as described in Subsection 6.3.3. For the fully-hadronic channel, the correct combination of the four non-b jets into W bosons had to be found among the three possible combinations, see Subsection 6.3.4. In the semi-leptonic case, this step was unnecessary, since the assignment of light jets and leptons to W candidates is unique. The pairing of W candidates and b jets into the two top quark candidates was done using a *kinematic fit*, exploiting constraints on the event topology to improve the top mass measurement, as discussed in Subsection 6.3.5. After the *background rejection* using a binned likelihood technique (Subsection 6.3.6), the final top mass distribution was fitted to extract the top mass and width as discussed in Subsection 6.3.7.

[1] Implemented in the *SelectedPandoraPFANewPFOCollection*.

6.3.1 Lepton Finder

The classification into fully-hadronic, semi-leptonic and fully-leptonic events was based on the identification of isolated leptons using a lepton finder as a first step of the analysis. It was optimized to identify charged leptons ($e^{\pm}$ or $\mu^{\pm}$) from the leptonic W boson decay. Since these leptons are typically highly energetic, and in contrast to leptons originating from hadronic decays in quark jets, well separated from other activity in the event, isolation and energy were used as selection criteria. A minimum lepton energy of 10 GeV was required, and for the isolation a cone around the lepton momentum axis with an opening angle of 10° was chosen. The lepton candidate was classified as isolated if no other charged particle with an energy larger than 2.5 GeV was measured inside the cone. The minimal required lepton energy was found using the true Monte Carlo information. The other energy cut value and the cone opening angle were determined to optimize the selection efficiency with a parameter scan using the true Monte Carlo information of a $t\bar{t}$ event sample. All events in which more than one isolated lepton was found were classified as fully-leptonic and were consequently rejected for the further analysis.

Table 6.4: Selection efficiency of the lepton finder for the various $t\bar{t}$ event classes, with and without the inclusion of overlaid background events.

	no $\gamma\gamma \to$ hadron events overlaid	$\gamma\gamma \to$ hadron events overlaid
Semi-leptonic events correctly identified (single isolated lepton found)	93 %	91 %
All-hadronic events correctly identified (no isolated lepton found)	97 %	96 %
All-leptonic events correctly identified (more than one isolated lepton found)	57 %	57 %

The efficiency for semi-leptonic and fully-hadronic events to be classified correctly by the lepton finder is summarized in Table 6.4 for events with and without $\gamma\gamma \to$ hadron events overlaid. The lower selection efficiency for fully-leptonic events is because here events with one or two τ leptons in the final state are included in the sample. For those events, the rejection is considerably less efficient due to the large branching fraction of hadronic τ decays and due to the reduced momentum of leptons from leptonic τ decays.

6.3.2 Jet Clustering

Jet clustering of the events was performed according to the classification of the lepton finder. At this stage the event sample was split into a fully-hadronic and a semi-leptonic branch. In the fully-hadronic branch, events were forced[2] to be clustered in six jets, while for the semi-leptonic branch four jets were required. In the latter, the isolated lepton was excluded from jet finding.
In the $t\bar{t}$ analysis performed for the ILC Letter of Intent, the so called Durham jet algorithm was used. The Durham jet algorithm was developed for e^+e^--colliders and collects particles to a jet, if the distance d_{ij} between a jet particle i and a jet particle candidate j is smaller than a certain value. This value is determined by the algorithm due to the enforced number of jets. The distance d_{ij} between these two particle is calculated via

$$d_{ij} = \min\left(E_i^2, E_j^2\right) \cdot \frac{2 \cdot (1 - \cos\theta_{ij})}{s}, \tag{6.1}$$

where θ_{ij} is the polar angle between the two particles, E_i^2 and E_j^2 are the corresponding particle energies squared and s being the nominal center-of-mass energy. Due to this distance calculation many background particles, especially in the forward region, are added to the jets by the algorithm. In the analysis performed for the ILC Letter of Intent this was not an issue, since the number of background particles was not critical. In an environment with the CLIC beam induced background conditions too many background particles are picked up to be included in the jets, instead of performing an additional background rejection. Therefore different jet algorithms from the FastJet package [90] were tested and the k_t algorithm with a $\Delta\eta$, $\Delta\phi$ metric was used. In this algorithm the distance between two particle is calculated according the equation

$$d_{ij} = \min\left(p_{\mathrm{T},i}^2, p_{\mathrm{T},j}^2\right) \cdot \frac{(\eta_i - \eta_j)^2 \cdot (\phi_i - \phi_j)^2}{R^2}, \tag{6.2}$$

where p_T is the transverse momentum of the particles, η is the pseudorapidity, ϕ is the azimuthal angle and R is a parameter, chosen by the jet algorithm user, which defines the size of the "jet-radius". Using Equation 6.2, the calculated particle distance is increased in the forward region, leading to the exclusion of more background particles from the jets and thus, making the jet clustering more robust against $\gamma\gamma \to$ hadrons events. These particles are collected in the so called beam jet. Since the events were clustered into a fixed number of jets, the value of d_{ij} was calculated by the algorithm leaving only the jet size parameter R to be selected. Different jet size parameter values were tested and a value of $R = 1.3$ was chosen, as the best trade-off between the requirements to not loose signal particles and to limit the inclusion of background. This is illustrated in Figure 6.2, which shows the total reconstructed energy in jets of the full-hadronic event class, both for events with and without $\gamma\gamma \to$ hadrons

[2] In the context of jet algorithms this is called the exclusive mode.

background and for a variety of jet size parameters. For R below 1.3, significant signal energy loss is apparent, while the largest parameter R of 1.57 results in a broadening of the total energy distribution due to pile up of background.

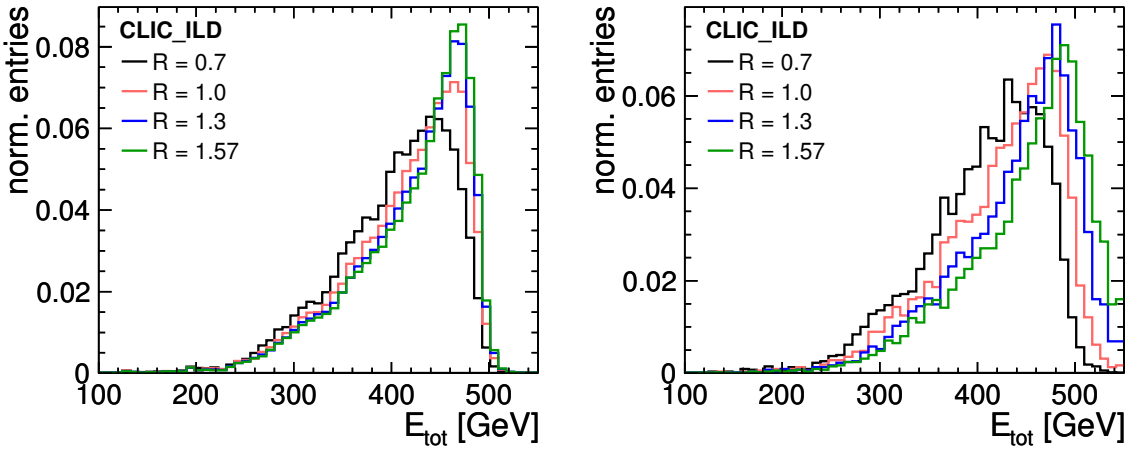

Figure 6.2: Effect of the size of the R parameter in the k_t jet-algorithm for the fully-hadronic decay channel of the signal samples without (*left*) and with overlaid $\gamma\gamma \to$ hadron events (*right*). The jet algorithm setting of $R = 1.3$ was chosen for the further analysis.

In the following discussions the different analysis branches (semi-leptonic event candidates and fully-hadronic event candidates) are referred to as *4 jet sample* and *6 jet sample*, respectively.

6.3.3 Flavor Tagging

Flavor tagging describes the method to determine the quark flavor, typically b, c or light (u, d, s), of the quark, which created a jet. Efficient b-tagging is essential for the identification of $t\bar{t} \to (bq\bar{q})(\bar{b}q\bar{q})$ and $t\bar{t} \to (bq\bar{q})(\bar{b}l\nu_l)$ events compared to multi-fermion background, and is also crucial for the correct assignment of jets to top quark decay product candidates for signal events. Flavor tagging was performed using the *LCFI Flavour Tagging* [91] package and is divided into two parts.
Quarks, for example from a decay of a W boson, hadronize and form hadrons which produce jets. In the first part of the flavor tagging the decay vertices of these hadrons are reconstructed using information from the vertex detectors. The vertex search is based on the function $V(\vec{r})$, which quantifies the relative probability to find a vertex at a location $\vec{r}$. The function $V(\vec{r})$ is constructed from the probability tubes of each track trajectory and from the position of the interaction point. More information about about the basics of the vertex search can be found in [92].

In the second part the flavor of each particle that decayed at the vertex is determined from its decay products. Since typically many particle are involved, a multivariate method is used to determine the flavor. The *LCFI Flavour Tagging* package uses a neural network to provide from a set of input variables the b jet probabilities ("b-tag") for each jet in the event. The input variables, which are based on information of the vertex position search, are listed in in Appendix in Table C.1 and are shown in Figure C.1 for the 4 and 6 jet signal samples. More details about the package and input variables can be found in [93].
The neural network training was performed using a 6 jet sample of $t\bar{t}$ events. These events were generated and reconstructed without beam spectrum, initial state radiation and top width, but did contain all other generation, simulation and reconstruction detail, such as overlaid $\gamma\gamma \rightarrow$ hadrons events. With this approach a statistically independent neural network training was achieved. The b-tagging efficiency versus purity for the full-hadronic and semi-leptonic signal event samples used in this analysis are shown in Figure 6.3. A performance degradation is seen by the difference between only signal events and signal events which have been overlaid with $\gamma\gamma \rightarrow$ hadron events.

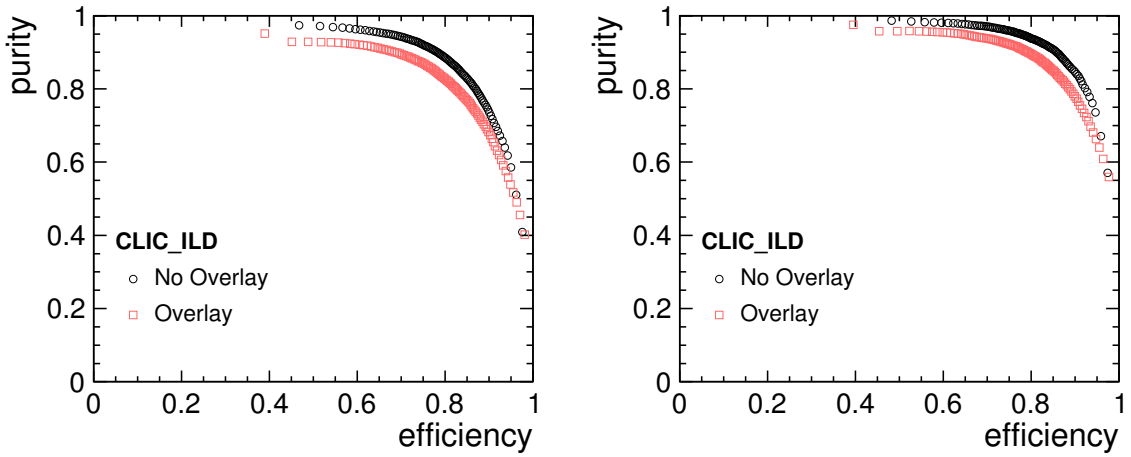

Figure 6.3: Efficiency versus purity of b-tagging for fully-hadronic signal sample (*left*) and the semi-leptonic event sample (*right*) with and without overlaid $\gamma\gamma \rightarrow$ hadron events.

6.3.4 Jet Combinatorics

For both samples the two jets with the highest b-tag values were classified as jets created by a b quark (b jets). All other jets were classified as light jets, i.e. they were created by u, d, s or c quarks, originating from the W decay.
In case of the 4 jet sample all decay products of the $t\bar{t}$ pair are found at this stage of the analysis: Two b jets, two light jets forming one W boson, one charged lepton and a neutrino

forming the other W boson. Since the neutrino is unmeasured, its momentum is taken to be the total missing momentum. The resulting mass distribution of the two W bosons is shown in Figure 6.4. The neutrino comprises, due to its momentum assignment, all energy reconstruction uncertainties, and since the missing energy measurement also includes contributions from the beam energy spectrum, the leptonic W mass is significantly less well constrained than the hadronic W mass. This is apparent from the comparison of the semi-leptonic distribution, Figure 6.4 with the distribution measured in the fully-hadronic case Figure 6.5, discussed in the following.

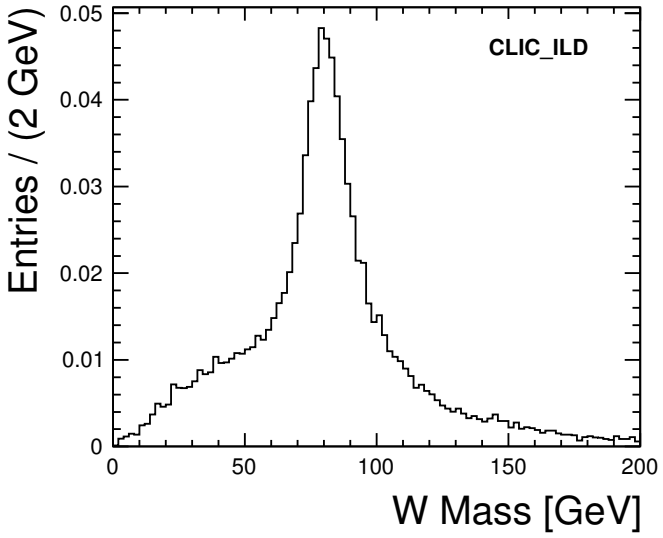

Figure 6.4: W boson invariant mass reconstruction in the semi-leptonic channel. One W boson is reconstructed from the four-momentum of the two light jets in the 4 jet sample. The other W boson is reconstructed from the measured lepton and missing energy, classified as neutrino. The neutrino momentum is given by the opposite sum of all other measured objects momenta.

In the 6 jet case, the correct pairing of light jets into W bosons has to be identified among the three possible permutations of constructing light jet pairs. For each permutation the invariant mass of both jet pairs was calculated and compared with the true W mass. The permutation with the minimal value of

$$v = |m_{ij} - m_W| + |m_{kl} - m_W|,$$

where $m_W = 80.4\,\text{GeV}$ and m_{ij} and m_{kl} are the invariant masses of two distinct jet pairs, was chosen as the correct combination. Figure 6.5 shows the invariant mass of all possible light jet pair combinations, and the chosen combinations to form W candidates.
After this step all decay products of the $t\bar{t}$ pair in the full-hadronic channel are uniquely assigned.

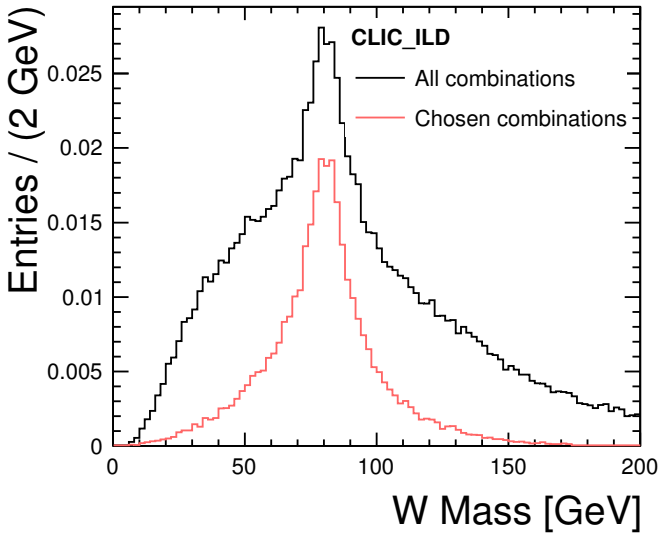

Figure 6.5: Effect of jet combinatorics for the W reconstruction in the 6 jet channel. Black: All possible jet-pair combinations from the set of four light jets. Red: Chosen jet combinations. The number of chosen combinations is reduced by a factor three compared to all combinations due to the three possible pairings for the four light jets.

6.3.5 Kinematic Fit

After the identification of b jets and the pairing of light jets and leptons into W bosons, the next step of the analysis is the correct grouping of W candidates and b jets into top quarks, which is done with a kinematic fit.
Such a fit uses kinematic constraints on the given physical process, in this case the $t\bar{t}$ decay, to improve the precision of the event parameters of interest. In this analysis those parameters are the properties of the top quarks, namely their four-vectors and especially their masses. The top quarks are reconstructed due to their decay products, which are measured with respective uncertainties. In the kinematic fit the decay products, called fit objects in the following formalism, are fitted such that, under the given kinematic constraints, they minimize a χ^2 that describes the deviations between the measured and the fitted quantities. Thus, the fit improves the measurement of the decay products and therefore the top quark mass determination.
The fit objects have either fit parameters η with measured values a, where $\eta = (\eta_1, ..., \eta_M)$ and $a = (a_1, ..., a_M)$, or unknown fit parameters ξ, where $\xi = (\xi_1, ..., \xi_N)$. In the context of this analysis, the fit objects describing measured jets and leptons have fit parameters η and the fit objects describing the unmeasured neutrino have unknown fit parameters ξ.
For each event the parameters of interest are determined using a least squares technique and physical constraints are incorporated into the fit using Lagrange multipliers λ as shown in the

following equation:

$$\chi^2 = (\eta - a)^T C^{-1} (\eta - a) + \sum_{k=1}^{K} \lambda_k \cdot H_k(\eta, \xi) + \sum_{l=1}^{L} S_l^2(\eta, \xi), \tag{6.3}$$

where $H(\eta, \xi)$ are hard constraints and $S^2(\eta, \xi)$ are soft constraints. Hard constraints have to be fulfilled in the kinematic fit. Soft constraints on a parameter have to be only fulfilled in a certain range in the kinematic fit, in which the soft constraints have to have a certain functional form, which has to be provided as input to the kinematic fit. This functional form cannot be arbitrary, in the used framework, making the soft constrain fitter option limited in use. The term $(\eta - a)^T C^{-1} (\eta - a)$, with the covariance matrix C, is a measure for the deviation of the fitted values from the measured values of the fit objects. Focusing only on hard constraints, the minimization of the function χ^2 with the necessary constraint on the minimum of $\bigtriangledown \chi^2 = 0$ leads to

$$\frac{\partial \chi^2}{\partial \lambda_k} = H_k = 0. \tag{6.4}$$

Equation 6.4 gives $L+K$ single equations for the determination of $M+N$ parameters. Solving these equations is done via so called fitters. Such fitters are implemented together with the explained formalism into the MarlinKinFit package [94], which is used in this analysis. The user has to declare hard and/or soft constraints and has to pass the fit objects to the MarlinKinFit program.
Here, only hard constraints are used since those have shown the best performance. The following constraints were used in the kinematic fit, where i sums over the $t\bar{t}$ decay products:

- energy conservation
  - $\sum_i E_i = 500\,\text{GeV}$
- momentum conservation
  - $\sum_i p_{x,i} = 5\,\text{GeV}$, due to the beam crossing angle of 20 mrad
  - $\sum_i p_{y,i} = 0\,\text{GeV}$
  - $\sum_i p_{z,i} = 0\,\text{GeV}$
- correct W boson mass measurements (with a nominal W boson mass of 80.4 GeV)
  - $|m_{W_1} - m_W| = 0\,\text{GeV}$
  - $|m_{W_2} - m_W| = 0\,\text{GeV}$
- equal mass of both top quark candidates
  - $|m_t - m_{\bar{t}}| = 0\,\text{GeV}$.

The use of hard constraints creates some issues in combination with the beam energy spectrum, which results in a sizable fraction of events with non-zero momentum along the beam axis and with reduced center-of-mass energy, as discussed below.
The input to the kinematic fit are the four-momenta of the light jets, already paired into W bosons in the case of the 6 jet sample, the four-momenta of the b jets as well as the four-momenta of the isolated lepton in the 4 jet case. In the latter case, also the unmeasured neutrino is represented in the fit, with starting values set to the measured missing energy and momentum in the event. The neutrino is included in the kinematic fit as a special *neutrino fit object*, making the constraints on energy and momentum conservation applicable also in the reconstruction of the semi-leptonic decay channel.
During the fit procedure, the fitter varies the particle momenta and energies to fulfill the constraints. This is done according to the detector resolution for the various input particles, both in energy, azimuthal and polar angle. The angular resolutions for jets and angular and energy resolutions for leptons were derived from Monte Carlo studies of the $t\bar{t}$ sample (see Appendix C.2) and are parameterized as

Jets:
$\sigma_E = 4.5\% \cdot E_{jet}$ $\quad \sigma_\theta = 0.27\,\text{rad} \cdot \text{GeV}/\sqrt{E_{jet}}$ $\quad \sigma_\phi = 0.25\,\text{rad} \cdot \text{GeV}/\sqrt{E_{jet}}$
Leptons:
$\sigma_p = 1.5 \cdot 10^{-4} \cdot E_l^2$ $\quad \sigma_\theta = 5\,\text{mrad}$ $\quad \sigma_\phi = 15\,\text{mrad}.$

The uncertainty of the energy resolution for jets is not obtained from the signal sample, because this includes uncertainties of the quality of the jet clustering, and thus correlations between the jets belonging to one parent particle, resulting in an overestimation of the energy uncertainties. Since these correlations are not taken into account in the kinematic fit, the uncertainties expected for single jets [95] are used as input parameters.
The fit provides a fit probability which is a measure of the goodness of the fit. In this analysis, the fitter is called twice for each event, accounting for the two possible combinations of W bosons and b jets into top quark candidates. The combination with the higher probability of the kinematic fit result is chosen as the correct combination.
The fit fails if the fitter is unable to satisfy the constraints outlined above within the allowed modifications of the input parameters. It was observed that some of the fit failures are due to the wrong identification of one of the b jets. This is particularly likely in the case of a W decaying into a charm quark and another light quark. Thus, to improve the number of successful fits and to account for possible wrong flavor tagging, the kinematic fit is repeated for unsuccessful kinematic fits after exchanging the b jet with the lower b-tag value with the light jet with the highest b-tag value. This procedure increases the number of successful kinematic fits by $\sim 20\,\%$.
The result of the kinematic fit, compared to the top mass reconstruction without kinematic fit, is shown in Figure 6.6 for the 6 jet case and in Figure 6.7 for the 4 jet case.
Both the 4 and 6 jet samples contain semi-leptonic events with τ decays and fully-leptonic

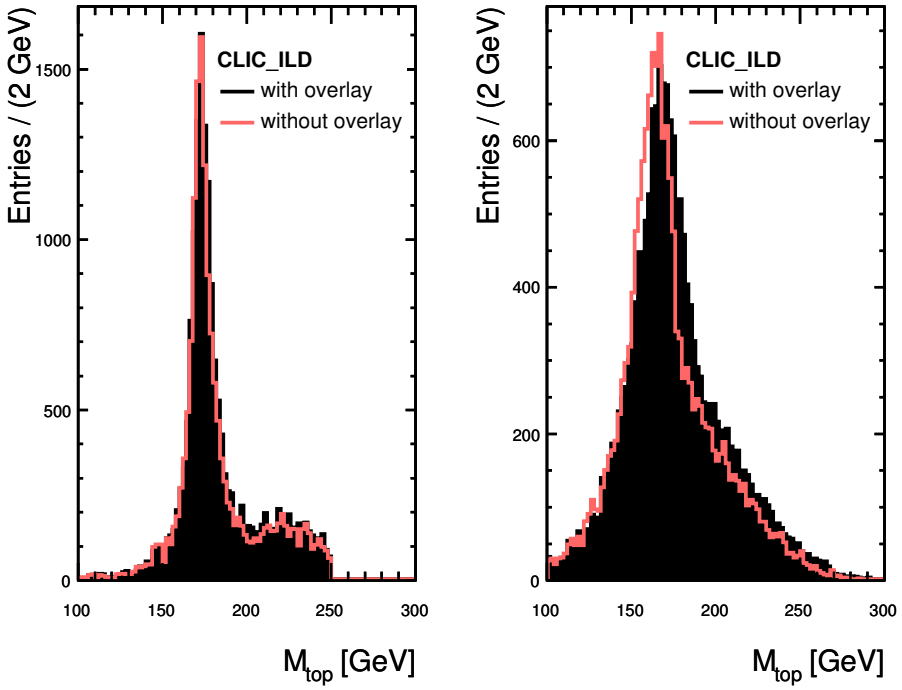

Figure 6.6: Reconstructed top mass distribution for the 6 jet channel without (*right*) and with (*left*) kinematic fit. The black lines show the top mass distribution for events with overlaid $\gamma\gamma \rightarrow$ hadrons events, the red lines show events without. The high-mass tail in the mass distribution obtained with kinematic fit is due to kinematic reflections for events with incorrect assignment of jets to top candidates.

events, with and without τ decays. The majority of events from τ decays of semi-leptonic or fully-leptonic events were grouped into the 6 jet sample, due to the dominating hadronic decay of the τ lepton. Due to the additional neutrino in the final state and the corresponding additional missing energy and momentum, the fit fails for 99 % (93 %) of the τ events in the 6 jet (4 jet) event sample, eliminating the problematic τ events from the final sample. From the remaining τ events in the final 6 jet (4 jet) sample 0 % (39 %) are τ decays from fully-leptonic events.
The isolated lepton finder (see Section 6.3.1) rejected approximately 56 % of the fully-leptonic events. The remaining fraction is mainly contained in the 4 jet sample, of which 95 % are rejected by the kinematic fit. In the end, the fraction of semi-leptonic events with τ decays and fully-leptonic events in the final sample is 1.3 % (2.7 %) for the 6 jet (4 jet) sample.
The overall rate of successful fits for true signal events (without τ events) in the 6 jet and the 4 jet was $\sim$37% and $\sim$60%, respectively. The relatively large failure rate of the kinematic fit

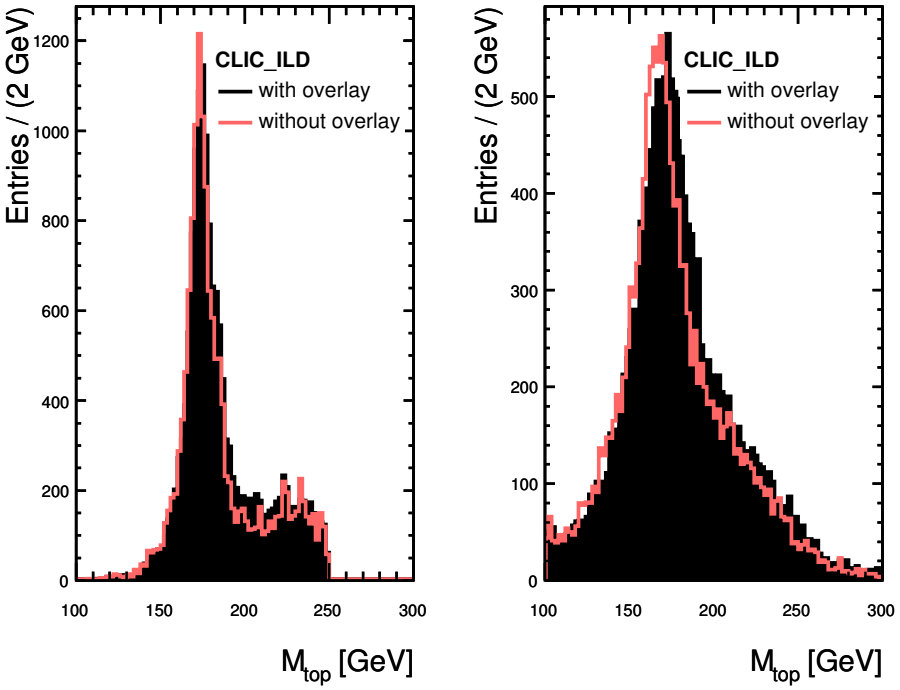

Figure 6.7: Reconstructed top mass distribution for the 4 jet channel without (*right*) and with (*left*) kinematic fit. The black lines show the top mass distribution for events with overlaid $\gamma\gamma \to$ hadrons events, the red lines show events without. The high-mass tail in the mass distribution obtained with kinematic fit is due to kinematic reflections for events with incorrect assignment of jets and/or leptons to top candidates.

is due to imperfectly reconstructed top quark decay particles. Several effects are expected to contribute to this: wrong classification into the semi-leptonic and fully-hadronic event branch, imperfect jet clustering, W reconstruction from a wrong jet combination, too large remaining signals of the $\gamma\gamma \to$ hadrons background or large effects of beamstrahlung.
The reasons for the failure of the kinematic fit have been investigated by studying the reconstructed invariant W mass without kinematic fit for events that pass or fail the fit. The results are shown for fully-hadronic events in Figure 6.8 and for semi-leptonic events in Figure 6.9. This shows quite clearly that mis-reconstructed W bosons are responsible for a significant fraction of the failed kinematic fits.
Another important factor for the failure of the kinematic fit was the center-of-mass energy of the event, which can deviate substantially from 500 GeV for events with large beamstrahlung contribution. In particular in the fully-hadronic event sample this results in failures of the kinematic fit. In the semi-leptonic case, also events with large beamstrahlung can pass the fit,

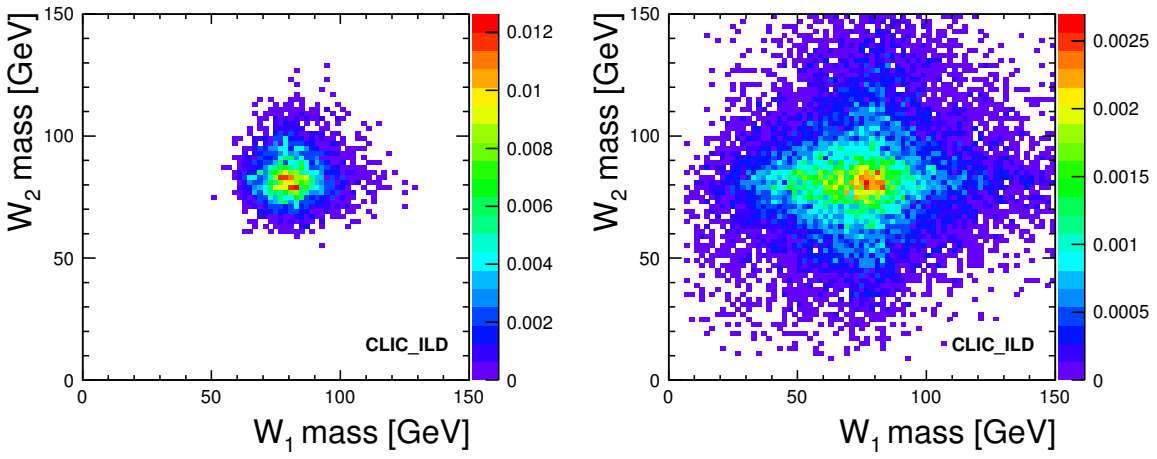

Figure 6.8: Reconstructed masses of the W bosons before the kinematic fit for the 6 jet event sample of the signal events. (*Left:*) successful kinematic fit. (*Right:*) Unsuccessful kinematic fit. Events with reconstructed W bosons masses far from 80.4 GeV do not lead to a successful kinematic fit.

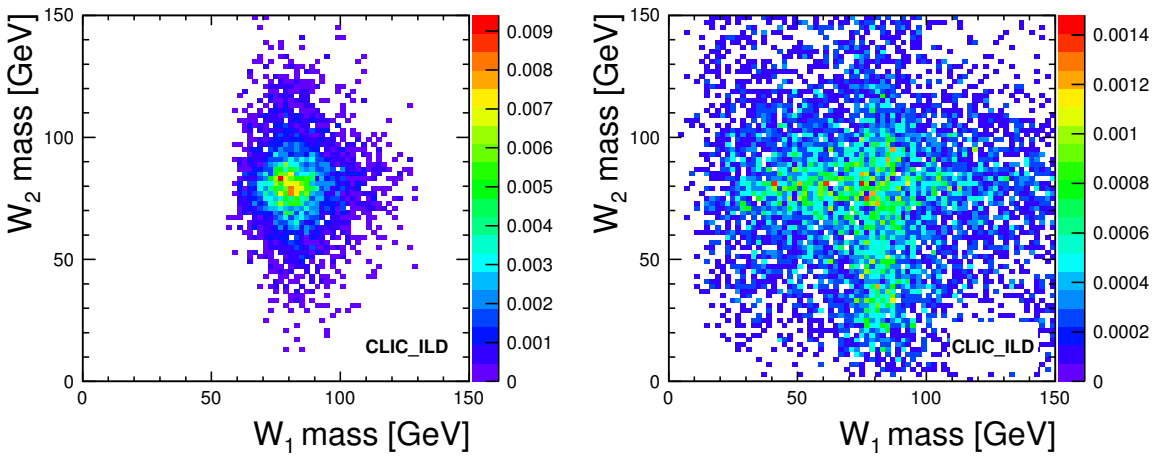

Figure 6.9: Reconstructed masses of the W bosons before the kinematic fit for the 4 jet event sample of the signal events. (*Left:*) successful kinematic fit. (*Right:*) Unsuccessful kinematic fit. Events with reconstructed W bosons masses far from 80.4 GeV do not lead to a successful kinematic fit.

because of the allowed missing energy due to the presence of the neutrino, which is partially responsible for the increased width of the invariant mass distribution.
The high kinematic fit failure rate also depends on the estimated errors of the fit object

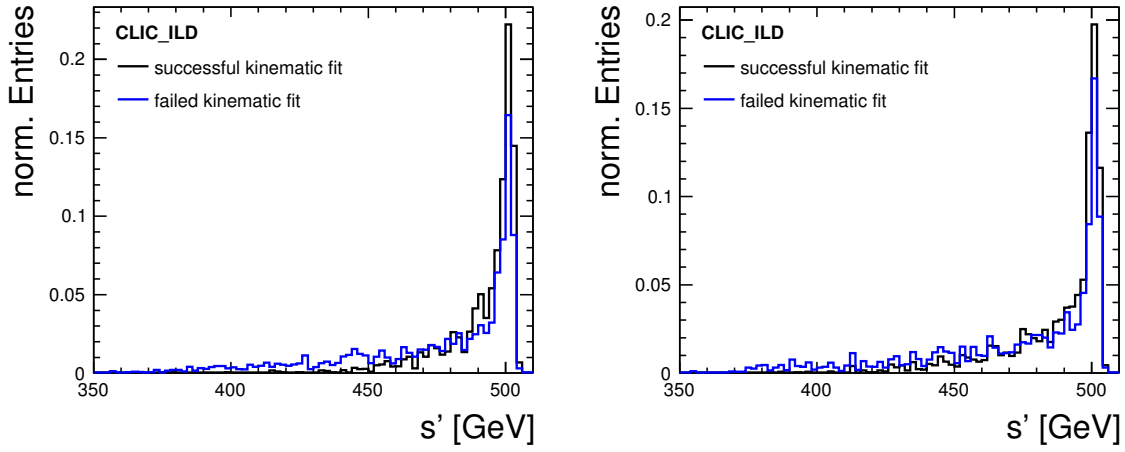

Figure 6.10: s' on generator level of the signal events for the 6 jet event sample (*left*) and the 4 jet event sample (*right*). The relation between an unsuccessful kinematic fit and large beamstrahlung is more evident for 6 jet events. In the 4 jet event sample the energy conservation constraint can be applied due to inclusion of the neutrino (MarlinKinFit: NeutrinoFitObject) in the kinematic fit.

parameters, i.e. the energy and angular resolutions of the jets and leptons. Larger errors lead to larger allowed variations in the particle momenta and thus to a bigger fit margin. Since only the single jet energy resolution and not the combined jet energy resolution, which would include errors due to the jet clustering, was taken into account, a smaller fraction of events pass the step of the kinematic fit. The relatively low success rate of the kinematic fit reflects the orientation of the analysis towards precision measurements of the top quark mass, which is best performed in optimally reconstructed events.
Since the kinematic fit places stringent constraints on the overall event topology, it also performs a powerful rejection of non-$t\bar{t}$ background. A large fraction of events from the considered background samples fail the fit, as summarized in Table 6.5.

6.3.6 Background Rejection

In addition to the rejection of physics background by the kinematic fit, further signal and background discrimination is needed to purify the signal. This is achieved by means of a binned likelihood technique [96] which combines several discrimination variables into one likelihood variable. For the two event classes j, *signal* and *background*, probability density functions $f^j(x_i)$ for each discriminating variable x_i were provided as input to the likelihood algorithm. The probability $p^j(x_i)$ for a given event to belong to event class j for a given value

Table 6.5: Background rejection efficiency of kinematic fit.

	Background rejection efficiency [%]	
$e^+e^- \rightarrow$	6 jet events	4 jet events
$q\bar{q}$	97.0	97.3
WW	94.6	85.7
ZZ	94.1	94.0
WWZ	13.1	25.2

of the discriminating variables x_i is given by

$$p^j(x_i) = \frac{f^j(x_i)}{\sum_k f^k(x_i)},$$

where k runs over all event classes.
The final likelihood for an event belonging to the signal event class, labeled with S, combining the probabilities of the individual discrimination variables, is given by

$$L_S = \frac{\prod_i p^{\mathrm{S}}(x_i)}{\sum_k \prod_i p^k(x_i)},$$

with i running over all discrimination variables and k over all event classes.
The chosen discrimination variables, shown in Figure 6.11, are:

- Highest b-tag value
- Second highest b-tag value
- Number of particles in the event
- Reconstructed W_1 boson and W_2 boson mass
- Difference between the reconstructed top quark masses without kinematic fit
- Sphericity, which is a measure for the roundness of an event[3]
- $\mathrm{d_{cut}}$, which is a variable provided by the jet clustering algorithm. The $\mathrm{d_{cut}}$ value used in this analysis, determines for each event the maximal particle distance, defined in Equation 6.2, for which n jets are found compared to $n-1$ jets, which would result in larger values of $\mathrm{d_{cut}}$. Thus, this variable is a measure of how likely it is to cluster a given event into the fixed number of n jets.

[3]The sphericity is given by $S = \frac{3}{2}(\lambda_1^2 + \lambda_2^2)$, where λ_1 and λ_2 are the eigenvalues of the sphericity tensor $S_{ij} = \sum_k P_{ki}P_{kj}$ $(i,j = x,y)$ formed by summing over the transverse jet momenta.

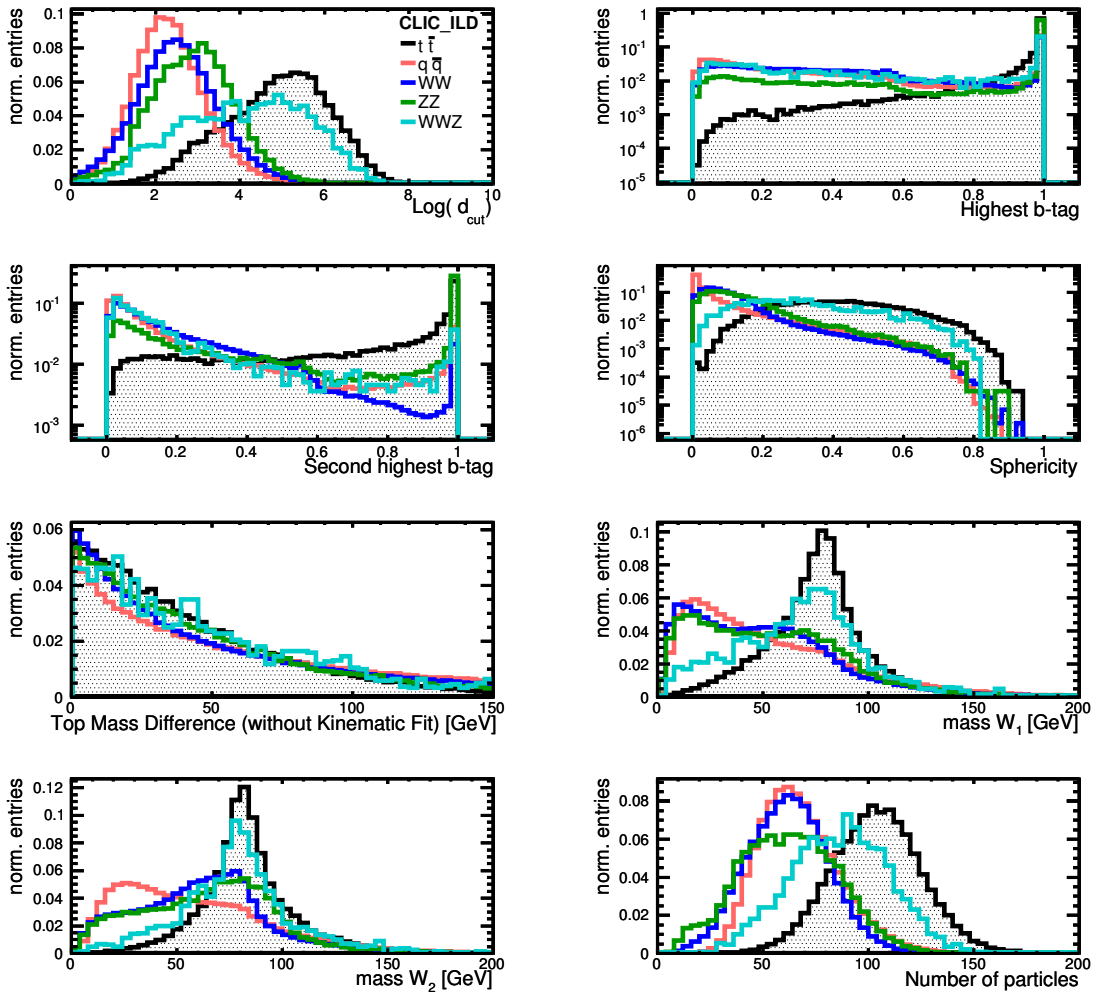

Figure 6.11: Distribution of the input variables of the background rejection. The black lines represent the signal, the other colored lines represent the background. All distributions are normalized.

At the time of the finalization of the analysis for the CLIC CDR, the fully simulated event samples were not sufficient to provide two independent data sets for the determination of the probability density functions for the likelihood calculation and for the final analysis. To avoid a bias from using signal and background events, both for the determination of the probability density functions and in the analysis, only events with an unsuccessful kinematic fit were used in the probability density function determination, resulting in statistical independence of training and analysis samples. Since the events with unsuccessful fits have somewhat different (less signal-like) characteristics than the ones passing the fit, this procedure is expected to result in a slightly decreased background rejection efficiency. To quantify this, the analysis

Table 6.6: Signal and background rejection efficiency of the likelihood technique for the event sample passing the kinematic fit.

	Signal efficiency	Background rejection efficiency
4 jet channel	93.5 %	98.0 %
6 jet channel	94.4 %	96.7 %

was repeated by using all events (with and without successful kinematic fit) for the probability density function determination. A decrease in background rejection efficiency of less than 0.5 % was observed for the case of statistically independent probability density function determination from events failing the kinematic fit, comparing to the use of all available events. This demonstrates that the approach chosen in the analysis is viable, and does not lead to a significant degradation of the results.

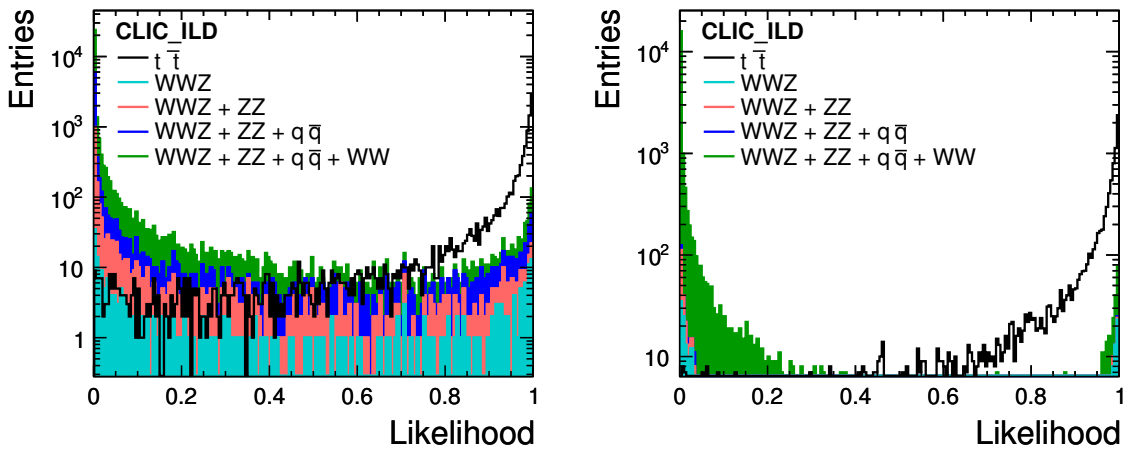

Figure 6.12: Likelihood for physics processes to belong to the signal events class for 6 jet events (*left*) and 4 jet events (*right*). A cut at a likelihood value of 0.6 was chosen to reject background events for the 6 jet and 4 jet event sample. The distributions of the different background processes are stacked on top of each other. The signal is not stacked.

The signal likelihood L_S for $t\bar{t}$ and background events passing the kinematic fit are shown in Figure 6.12 for 4 jet and 6 jets events. A cut on the signal likelihood L_S of 0.6 was chosen to reject background from signal events in the the 6 jet and the 4 jet sample. The resulting efficiencies for signal extraction and background rejection are summarized in Table 6.6.

6.3.7 Top Quark Mass and Width Measurement

The top mass and width was extracted using an unbinned likelihood fit of the final top mass distribution of events (signal and background) after kinematic fit and background rejection. The fit function consists of three components, which account for physics background, the detector resolution and the signal itself. The first two had to be determined in constrained fits prior to the fit of the final distribution, resulting in a three step approach to the mass fit:

1. Fit of the true background events only, to determine a background parameterization.
2. Fit of the true signal events only, to determine the detector resolution function on an independent event sample with approximately twice statistics (see Table 6.2).
3. Final fit of measured top mass distribution with true signal and background events, classified by the background rejection as events belonging to the signal class.

To parameterize the background, a threshold function was used, in which the threshold was fixed to $a = 100\,\text{GeV}$:

$$\text{bkg\_pdf} = (x-a)^b,$$

where x are the measured top mass values. For the bkg_pdf fit the parameter b was left free. The final parameters for the fitted background distribution can be found in Appendix C.3.
For the signal fit, the following PDF was used:

$$\begin{aligned}\text{sig\_pdf} &= f \cdot \text{BreitWigner}(\text{m}_{\text{bw}}, \sigma_{\text{bw}}) \otimes (\text{Gauss1} + \text{Gauss2} + \text{Gauss3}) \\ &\quad + (1-f) \cdot \text{GaussTail}\end{aligned}$$

This fit consists of two main components, a signal part described by a Breit-Wigner function convolved with a detector resolution function implemented by the sum of three Gaussians, and a background part, labeled *GaussTail*, to account for the high-mass tail, observed in the signal distribution at masses around 230 GeV. *GaussTail* is a Gaussian, which mean and width were left free in the fit. The mean value of the Breit-Wigner function is given by m_{bw}, and the corresponding width by σ_{bw}. The high-mass tail in the mass distribution is caused by kinematic reflections in the kinematic fit, originating from the fitting of miss-reconstructed events, where jets were incorrectly assigned. The relative fraction of the two components is described by the factor f.
The detector resolution component of the signal part is described by

$$\begin{aligned}\text{Gauss1} + \text{Gauss2} + \text{Gauss3} &= (f1 \cdot \text{Gauss1}(\text{x}, \text{m1}, \text{s1})) + \\ &\quad (f2 \cdot \text{Gauss2}(\text{x}, \text{m2}, \text{s2})) + \\ &\quad ((1.0 - f1 - f2) \cdot \text{Gauss3}(\text{x}, \text{m3}, \text{s3})),\end{aligned}$$

where the notation Gauss(x, mean, width) is used and $f1$ and $f2$ are the fractions of the Gaussians in the sum. This function does not only represent the detector resolution, but also

accounts for systematic effects introduced by the analysis chain and by the pick-up of $\gamma\gamma \rightarrow$ hadrons background.
For the fit of the true signal distribution, to determine the resolution function, a statistically independent event sample was used. The mean and width for the Breit-Wigner component were fixed to the generator values of $m_{\mathrm{bw}} = 174.0\,\mathrm{GeV}$ and $\sigma_{\mathrm{bw}} = 1.37\,\mathrm{GeV}$. All parameters of the Gaussian sum were left free. The resulting final parameters of the fit are listed in Appendix C.3.

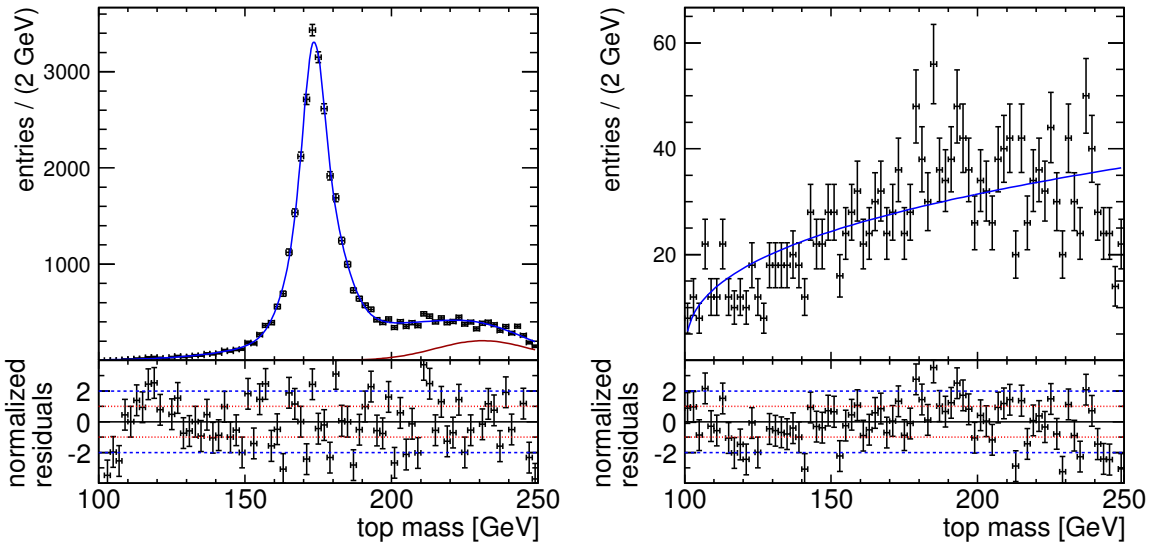

Figure 6.13: Pure signal distribution (*left*) and pure background distribution (*right*) for the 6 jet events are indicated by the black points with error bars. The blue line indicates the signal fit of the sig_pdf. The red line indicates the fit of the GaussTail, which is part of the signal fit.

Figures 6.13 and 6.14 show the fits to the signal only and background only distributions, for the fully-hadronic and the semi-leptonic event sample, respectively.
The final fit function for the top mass distribution, containing signal and background events, is given by the sum of the signal and background functions,

$$\mathrm{pdf} = \mathrm{y}_{\mathrm{Signal}} \cdot \mathrm{sig\_pdf} + \mathrm{y}_{\mathrm{Background}} \cdot \mathrm{bkg\_pdf},$$

where y_{Signal} and $y_{\mathrm{Background}}$ describe the signal and background yield, respectively. In the final fit, fixed values for the Gaussians of pdf_bkg and pdf_sig were used, leaving only $m_{\mathrm{bw}}, \sigma_{\mathrm{bw}}$, y_{Signal} and $y_{\mathrm{Background}}$ as free parameters.
The fit was performed independently for the fully-hadronic and for the semi-leptonic events and is shown in Figure 6.15.
The resulting top mass is

$$m_{\mathrm{top}} = 174.07\,\mathrm{GeV} \pm 0.08\,\mathrm{GeV}$$

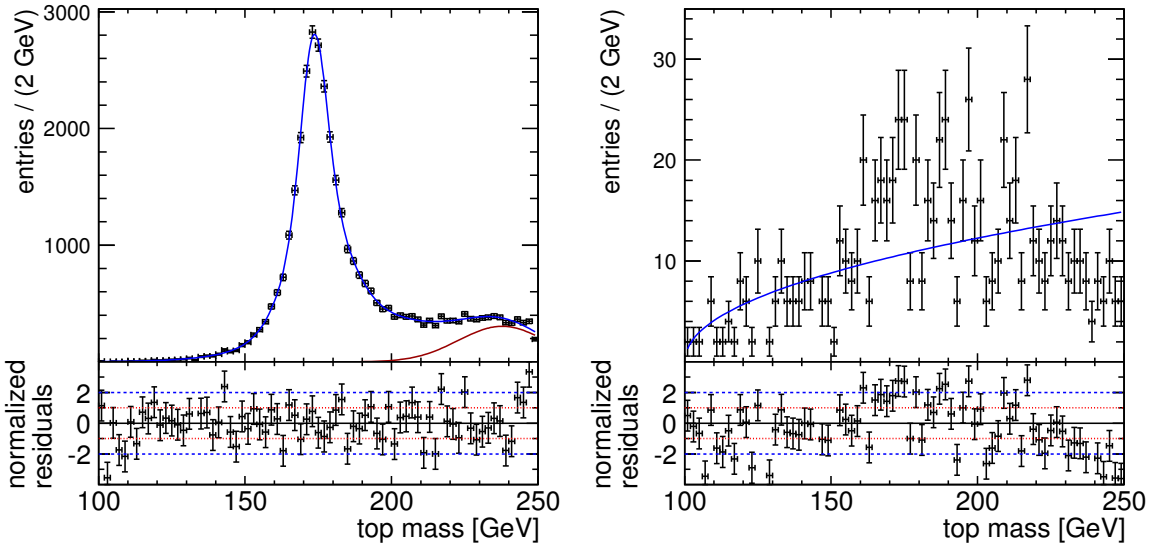

Figure 6.14: Pure signal distribution (*left*) and pure background distribution (*right*) for the 4 jet events are indicated by the black points with error bars. The blue line indicates the signal fit of the sig_pdf. The red line indicates the fit of the GaussTail, which is part of the signal fit.

for the fully-hadronic sample, and

$$m_{\text{top}} = 174.28\,\text{GeV} \pm 0.09\,\text{GeV}$$

for the semi-leptonic sample. The generated top mass was 174 GeV, thus the fully-hadronic mass is in excellent agreement with the input value, while the semi-leptonic measurement differs by three standard deviations. This deviation is most likely due to uncertainties of the detector resolution function, which was determined from a statistically independent sample of approximately two times the integrated luminosity compared to the signal sample. For the top mass measurement presented in the ILC Letter of Intent, although using a different fit function, a second $t\bar{t}$ sample of 20 times integrated luminosity as the signal sample was generated. This was not possible for the CLIC CDR.
To study a possible bias, from using the same input values as for the data sample, the parameter adjustment was also performed on a sample with a mass of 175 GeV and a width of 1.5 GeV. The corresponding figures and results are discussed further in Appendix C.5 and have lead to results consistent with the ones presented here. This shows that the generator mass in the fit training sample does not lead to significant bias in the results. Consistent results were also obtained with a different fit function, as used in the ILD Letter of Intent, as discussed in Appendix C.4.
The determination of the top quark width is more challenging, and depends strongly on the used data sample for the fit adjustment and on the choice of the fit function, in particular in

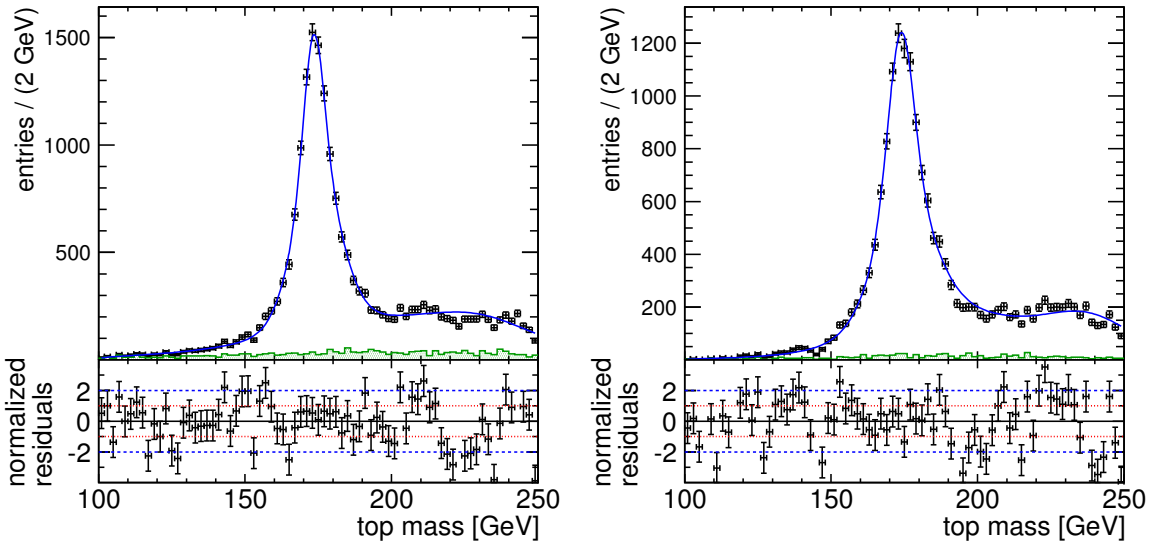

Figure 6.15: Final top mass distribution for 6 jet events (*left*) and 4 jet events (*right*). Black points with error bars indicates simulated data classified at signal events. The green hatched histogram stands for physical background. The blue line indicates the fit of the top mass distribution.

the semi-leptonic case. For the fully-hadronic sample, a width of

$$\sigma_{\text{top}} = 1.33\,\text{GeV} \pm 0.21\,\text{GeV}$$

was obtained, to be compared with a generator level value of 1.37 GeV. For the semi-leptonic sample, a width of

$$\sigma_{\text{top}} = 1.55\,\text{GeV} \pm 0.26\,\text{GeV}$$

was found, also in good agreement with the generator value.
For the ILC top study in the Letter of Intent statistical errors for the top quark mass of 110 MeV and 140 MeV were determined for the fully-hadronic and semi-leptonic channel, respectively. The statistical errors of the width were estimated to 70 MeV and 90 MeV for the two event classes. It should be noted that the size of this errors values are partially due to the different fit function and range used in the two studies. This is further discussed in Appendix C.4, followed by a detailed cut-flow table of the different analysis steps. However, this study shows that the top mass can be determined at a 500 GeV CLIC machine with comparable statistical precision to the resolutions obtained for ILC in the ILD Letter of Intent in both the fully-hadronic and semi-leptonic decay channels, despite the more challenging experimental environment at CLIC.

6.4 Summary

The mass of the top quark is one of the key parameters of the Standard Model, and provides sensitivity to new physics. The presented study, using full simulations including machine and physics backgrounds, carried out in the framework of the CLIC CDR, has shown that a 500 GeV linear e^+e^--collider based on CLIC technology is an excellent tool for precision top quark measurements. The machine induced $\gamma\gamma \to$ hadrons background could be controlled by a combination of timing and p_T cuts and by a suitable choice of the jet clustering algorithm. Precise reconstruction of the event kinematics was achieved by means of a kinematic fit, which also served to control the energy uncertainty due to the beam energy spectrum and contributed to the rejection of non-$t\bar{t}$ background. With an integrated luminosity of 100 fb^{-1}, a statistical error of 80 MeV was achieved in the fully-hadronic decay channel, and a precision of 90 MeV was achieved in the semi-leptonic channel. This precision is comparable to that expected for the ILC, despite the more challenging experimental environment at CLIC.

For possible further studies of the analysis, for example the estimation of a systematic error, different points can be addressed. First of all the systematic error due to the particle flow reconstruction would have to be determined. Furthermore particularly important for this analysis would be to have a large enough set of signal events available. In this analysis the training of the flavor tagging neural network and the binned likelihood regression training had to be done with non perfect events samples. In case of the flavor tagging an event sample like $e^+e^- \to Z/\gamma^* \to q\bar{q}$ would be preferred. This would need to have a large amount of statistics in order to guarantee a successful b-tagging. In case of the regression method a statistically independent signal sample would be necessary. Both cases would reduce an impact on the systematic error.
The control signal sample, used in the final top quark mass distribution fit, of approximately two times higher statistics was only produced and thus available for these analysis at the very last stage. A control sample with much higher statistics, as in the study for the ILC, would be necessary to fully study possible biases in the final top quark mass fit.
Another issue is the jet clustering. Different algorithms have been tested, primarily to reduce the $\gamma\gamma \to$ hadrons background further. Also the goodness of the jet clustering was tried to be estimated but no numbers were quoted in this thesis. Stating the goodness of a jet clustering algorithm would first require to classify which conditions have to be fulfilled for an event to be clustered correctly. For example it has to be defined how well quark and jet directions and energies have to match. Also it has to be stated if the jet clustering failed if only one jet is not correctly clustered or if all jets are not correctly clustered. For the systematic error and in case of the used k_t jet clustering algorithm it should also be studied how much a wrong energy sharing between jets affects the results and how much not counted energy. This is related to the estimated error of the jet energy in the kinematic fit.
The kinematic fit could be improved if it would be possible to include the reduced center-of-

mass-energy distribution (s') into the kinematic fit and thus require only a soft instead of a hard energy conservation constraint according to the distribution. So far this is not possible with the used software.

Chapter 7

Conclusions and Outlook

This thesis discussed studies to improve the energy reconstruction and resolution of hadronic calorimeters used at a future e^+e^--collider. In addition, an analysis of top pair production for the estimation of top quark properties at such a collider was presented.

A future linear e^+e^--collider can follow up studies and searches of the currently running LHC. Due to novel reconstruction techniques and detectors especially designed for such a reconstruction, analyses can be performed with very high precision. The CALICE collaboration develops highly granular calorimeters for the operation in a detector at such a future e^+e^--machine. Different machine technologies with different design center-of-mass energies exist, the two main ones are ILC and CLIC. The detector concepts for both accelerators are designed to have an event reconstruction based on a particle flow technique. Particle flow is a novel approach to calorimetry with which it is possible to reconstruct the four-vectors of all particles in each event. The calorimeters' high granularity is essential for the particle separation in this approach and hence for an excellent performance of the reconstruction method. Thus, the calorimeters have two main purposes: the traditional energy measurement and the distinct separation of individual particles within high energy jets.

High granularity can be used for the particle separation and to improve the energy reconstruction. All CALICE calorimeters are non-compensating sampling calorimeters, i.e. the detector response to electrons and hadrons differs. The development and performance of three software compensation techniques to improve the hadronic energy reconstruction and thus the energy resolution of a calorimeter with analog readout, were presented in this thesis. To reach an equalization of electromagnetic and hadronic detector response in hadronic cascades, the three approaches make use of the calorimeters' fine granularity, since it allows a deeper insight into the composition of a hadronic event. In the local software compensation technique this was achieved by weighting the individual cell energies, depending on their energy density. The global software compensation techniques were either based on a weighting of the complete shower energy, regulated by the shower energy density, or on the use of a neural network.
Weight factors of all three software compensation techniques were extracted from simulated data. For the local and global technique based on the energy density, weights were also extracted from test beam data. In all cases a weight application was performed on simulated and test beam data. The obtained correlation between reconstructed and beam energy was discussed as well as the resulting energy resolutions. As the most important result it can be

concluded that all approaches can be applied successfully to test beam and simulated data. For test beam data an energy resolution improvement of approximately 20 % was achieved in case of the local software compensation method. A global weighting of the shower energy resulted in approximately 17 % energy resolution improvement of test beam data and an approximately 22 % better energy resolution was gained due to the use of a neural network, compared to a reconstruction without software compensation.
The decision which technique is to be chosen for the application in the future should not only be based on the size of the energy resolution improvement. The neural network approach achieved the best value of the energy resolution, but the methods based on energy density were less resource extensive. The local energy density weighting technique exploited the calorimeter's granularity more and gave a larger energy resolution improvement than the global one. However, only the global energy density weighting technique achieved a constant improvement over the full energy range to which it was applied.
Furthermore, it was shown that parameters for the application of software compensation can be derived from Monte Carlo simulation data. Two physics lists for the simulation in Geant4, which are modeling the hadronic cascades in the simulation, were used, namely QGSP_BERT and FTF_BIC. The two sets of simulated data with the physics lists differed in their performance of reproducing the characteristics of test beam data. A better description of the initial energy resolution was obtained using simulated data with the physics list QGSP_BERT. Simulated data with the physics list FTF_BIC on the other hand, describe better the initial reconstructed energy of test beam data.
The average energy resolution improvement of test beam data using software compensation was very similar for weights extracted from simulated data with both hadronic models. Concerning the difference between reconstructed and beam energy, simulated data with the physics list FTF_BIC gave slightly better results than weights which were extracted from simulated data with the physics list QGSP_BERT. Thus, the physics list FTF_BIC is favored for the use in software compensation techniques.
In addition, the results using software compensation of simulated data itself were compared. In nearly all cases a larger energy resolution improvement was achieved for simulated data compared to test beam data. The largest energy resolution improvement for all methods was achieved for simulated data with the physics list FTF_BIC. The overall spread of the difference between reconstructed and beam energy was larger for simulated data than for test beam data. However, the reduction of that spread using software compensation was similar for test beam and simulated data.
Due to the ongoing comparison of different variables of test beam and simulated data not only by the CALICE collaboration and the following adjustment of the hadronic model parameters by the developers of the physics list, a constant physics list improvement is expected. The presented software compensation techniques will gain from such an improvement, for example if the differences in the energy resolution of simulated and test beam data will be reduced.

The analog hadronic calorimeter, presented in the first part of this thesis, is a prototype for the hadronic calorimeter of an ILC detector and, with a different absorber material (tungsten instead of steel), also for the hadronic calorimeter of a CLIC detector. It was shown that the detector response to electromagnetic and hadronic particles differed by approximately 30 % for the ILC hadronic calorimeter model. For the CLIC hadronic calorimeter the response to both particles types was nearly equal. Thus, the performance of the local software compensation technique was studied in simulations of the complete detector design ILD of ILC. The technique was implemented into the particle flow reconstruction software and the results for single hadron and typical jet events were compared to the reconstruction without software compensation. Software compensation improved the energy resolution of single hadron events, however, the effect in jet events was smaller, as expected due to the reduced influence of the energy resolution performance of the hadronic calorimeter in the particle flow reconstruction approach. It was shown that the effect of confusion, namely the mis-identification and -combination of tracks and calorimeter clusters to reconstructed particles, determined the success of the software compensation in improving the jet energy resolution. If the effect of confusion was not the dominant contribution to the overall energy resolution, a jet energy resolution improvement could be achieved. Otherwise the jet energy resolution was degraded.
If software compensation should be made available as a common option in the particle flow reconstruction software, several points should and need to be investigated more closely. For example, the weight extraction would need to be automatized for all possible simulation options like physics lists and detector models. Furthermore, the influence of the electromagnetic calorimeter should be investigated further and the handling of possible mis-reconstructed events could be improved to avoid an energy resolution degradation.

To quantify that CLIC is an excellent precision machine, several physics analyses were performed for the CLIC Conceptual Design Report. This was done especially in view of the more critical beam-induced background situation compared to ILC. One of these analyses, namely the determination of top quark properties from top pair production, was presented in this thesis. Since the analysis was performed at a center-of-mass energy of 500 GeV, it is directly comparable to the top pair production studies performed for the ILD Letter of Intent at the ILC. From the signal of $e^+e^- \to Z/\gamma^* \to t\bar{t}$ events the semi-leptonic and the fully-hadronic decay channels were used for the determination of the top quark mass and width.
Besides the signal sample the CLIC analysis considered Standard Model background processes. The event simulation followed a realistic description of the CLIC beam spectrum and events were overlaid with beam-induced $\gamma\gamma \to$ hadrons processes. These overlaid background processes had significant influence on the signal, as they largely increased the total reconstructed energy of an event. To reduce the beam-induced background, particles with similar characteristics as those from $\gamma\gamma \to$ hadron events were rejected using a combination

of timing and p_T cuts. The analysis aimed for a clean signal sample, which was achieved due to an almost negligible and flat background remaining in the final set of classified signal events. As a result, the top quark mass, generated at 174 GeV, was obtained to be $m_{top} = 174.07\,\text{GeV} \pm 0.08\,\text{GeV}$ for the fully-hadronic sample, and $m_{top} = 174.28\,\text{GeV} \pm 0.09\,\text{GeV}$ for the semi-leptonic sample. The top quark width was generated with 1.37 GeV and in the analysis estimated to $\sigma_{top} = 1.33\,\text{GeV} \pm 0.21\,\text{GeV}$ for the fully-hadronic sample and $\sigma_{top} = 1.55\,\text{GeV} \pm 0.26\,\text{GeV}$ for the semi-leptonic sample. The results are comparable with what was achieved for an analysis at the ILC.
Besides the statistical error estimation, on which this thesis focused, studies on the systematic error would further complete the analysis. One of the largest contributions to the systematic error is the jet energy scale, the uncertainty of which could be reduced by using the W bosons from the top quark decay.

Acknowledgements

First of all, I would like to thank my supervisior Dr. Frank Simon for giving me the opportunity to do this thesis, his guidance and continuous flow of ideas during my doctoral studies. Also, I want to thank my thesis referees Prof. Dr. Christian Kiesling and Prof. Dr. Jochen Schieck for agreeing to read my thesis.

During my studies, I got lots of help from a number of people of whom I would like to name a few: Angela Lucaci Timoce and Nils Feege who helped me with CALICE software and calibration issues. Peter Speckmayer for his neural network support, Stephane Poss for his patience during the rough time of the CLIC CDR analysis working phase, Jeremy Dalseno for his fitting expertise and John Marshall, whose PandoraPFA knowledge and help was very motivating. Also I would like to thank everyone who helped proofreading my thesis.

A big thanks goes to my office colleagues Lars Weuste and Christian Soldner, which I always could bother with questions. The whole ILC and Belle/Belle II group I would like to thank for enough coffee, sugar, milk and tea times, in which no Earl Grey was consumed.

During my breaks in the theory coffee room I enjoyed the funny conversations and discussion. Therefore, I would like to thank all regular attendances, like Ananda Landwehr, Patrick Kerner, Daniel Härtel and Clemens Kiessig.

Karim I would like to thank for his love, patience, and encouragement.
I would like to thank my mother and my sisters Gabriela, Christine and Sabine for their support. A special thanks would go to my father, who unfortunately cannot hear this anymore. I know he always believed in me, which was very important.

Danke.

Appendix A

Additional information for the energy resolution studies of CALICE pion data

A.1 Run selection

The following figures describe some of the quality checks which have been made for the run selection of the pion analysis. Figure A.1 shows the noise level for random trigger events without beam of the AHCAL. One run, which does not follow the temperature dependence of the mean noise level, was excluded from the analysis. In the analysis only hits with an energy deposition above the threshold of 0.5 MIP were considered. The AHCAL scintillators were read out with SiPMs, in which the thermal noise of the silicon increased with temperature. Thus, for higher temperature more noise hits have signals above the hit energy threshold.

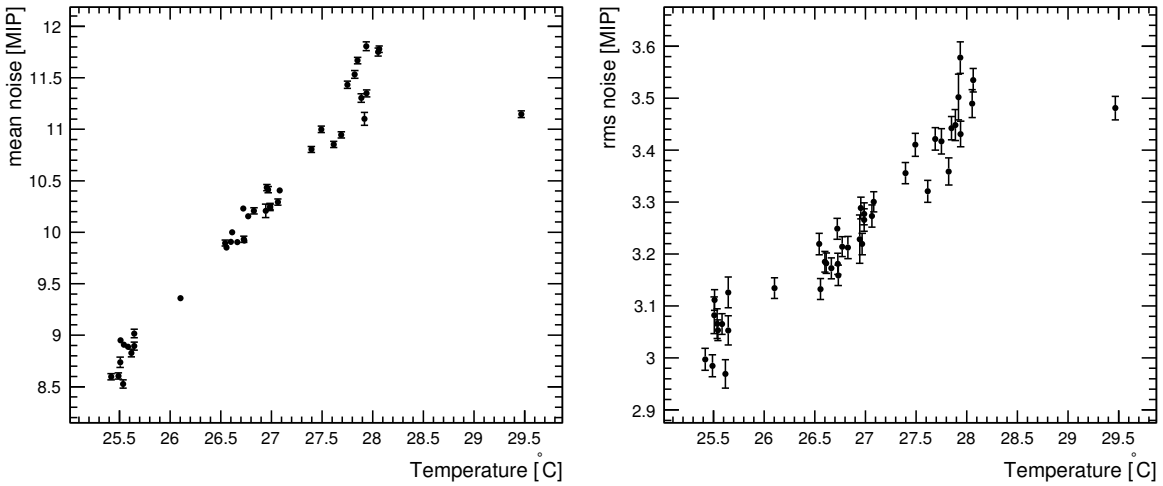

Figure A.1: Mean (*left*) and RMS (*right*) values of the noise in the AHCAL versus the temperature for the available pion runs. The noise was measured using random trigger events without beam. The run with the highest temperature was excluded from the further analysis (run number 330557).

Figure A.2 shows the noise level for random trigger events without beam for the TCMT. Since the absorber thickness before the last seven active TCMT layers is approximately five time

larger than of the ones in the first nine layers, these layers got a five times higher weight in the overall energy sum. The higher mean and RMS values of the noise distribution of the TMCT show that the TMCT is rather noisy. Converting this energy into the GeV scale led to a mean noise value of approximately 0.5 GeV, which is significant at low beam energies.

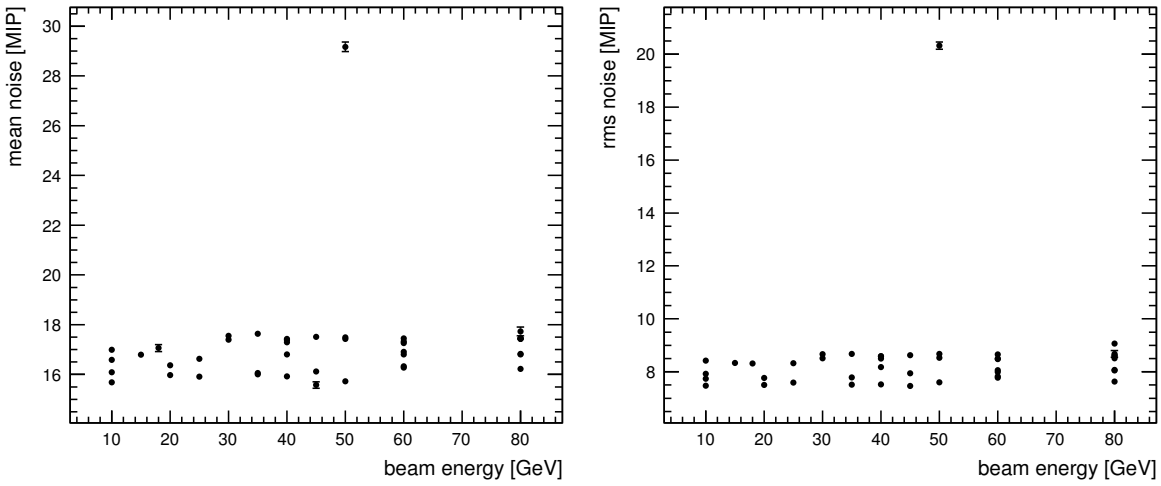

Figure A.2: Mean (*left*) and RMS (*right*) values of the noise in the TCMT versus the beam energy for the available pion runs. The noise was measured using random trigger events without beam. The run with the very high noise level (run number 331284) was excluded from the further analysis.

Figure A.3 shows a comparison of the longitudinal energy profiles for two runs. One has a particular noisy TCMT (layer numbers > 67) and was therefore excluded from the further analysis.

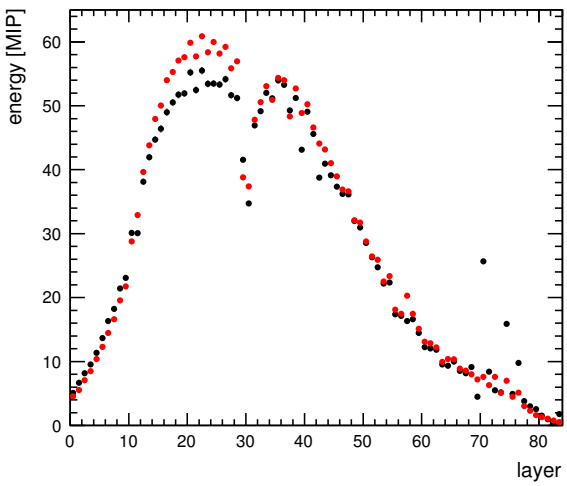

Figure A.3: Distribution of the energy measured in each calorimeter layer. Layers 0-29 refer to the ECAL, layer 30-67 to the AHCAL and layers 68-84 to the TCMT. Both distributions are for 50 GeV pion runs. The black markers show a run (run number 331284) with an extremely noisy TCMT, which was excluded from the further analysis.

A.2 Run list

The following two tables list the runs chosen for the pion analysis. Table A.1 lists the positively charged pion runs, Table A.2 the negatively charged pion runs. The table does not only include run number, beam energy, pion charge and Cherenkov trigger settings, but also the results of the event selection for each run. # fits refers to the number of fits, with a Gaussian, which had to be performed till an $\chi^2/\text{ndf} < 2$ was achieved in the fit. The starting range for the fit was $\pm$ 2 RMS around the mean value and was reduced by 0.2 RMS for each further fit. The definition of empty, bad, multi-particle (MP) and muon events were explained in Subsection 4.1.5. The label e^-/p refers to the percentage of events in which the Cherenkov trigger had a different flag than the one stated in the tables. During the run period in which the runs were taken, changes in the beam composition, quality and trigger threshold might have changed also for same beam energies, explaining the variation of electron, protons and muon contents.

Table A.1: List for the CALICE π^+ data runs used in the energy resolution analysis

run number	π charge	Cherenkov	Energy [GeV]	# fits	Empty [%]	Bad [%]	MP[%]	Muon [%]	p [%]
331340	+	on	30	1	0.043	0.95	0.34	30.03	41.02
331339	+	on	40	1	0.012	0.43	0.57	4.55	18.89
331338	+	on	40	1	0.011	0.42	0.56	4.56	18.67
331335	+	on	50	1	0.012	0.34	0.67	4.38	16.60
331334	+	on	60	1	0.008	0.40	0.82	3.77	21.47
331333	+	on	60	1	0.007	0.38	0.85	3.88	21.28
331324	+	on	80	1	0.006	0.35	1.14	2.74	33.68
331298	+	on	30	1	0.043	0.96	0.36	30.27	40.73
331282	+	on	60	1	0.006	0.41	0.86	3.63	21.27
331280	+	on	80	1	0.018	0.36	1.13	3.22	33.71

Table A.2: List for the CALICE π^- data runs used in the energy resolution analysis

Runnumber	π charge	Cherenkov	Energy	# fits	Empty [%]	Bad [%]	MP [%]	Muon [%]	e^- [%]
331664	-	off	60	1	0.006	2.69	1.41	3.77	0.00
331655	-	off	60	1	0.004	2.67	0.73	3.84	1.01
331654	-	off	80	1	0.005	2.73	0.92	3.58	5.27
331568	-	off	60	1	0.005	2.64	2.64	3.84	0.47
331567	-	off	80	1	0.003	2.74	1.02	3.46	5.23
331556	-	off	60	1	0.007	2.67	0.74	3.91	0.25
331554	-	off	80	2	0.005	2.71	0.95	3.63	4.31
330962	-	off	80	1	0.012	0.37	0.92	4.05	70.25
330960	-	off	35	1	0.003	1.06	0.82	17.64	3.32
330961	-	off	45	1	0.020	0.75	0.99	5.64	36.74
330850	-	off	10	1	3.047	20.71	0.12	6.32	31.36
330777	-	off	10	6	0.153	4.51	0.14	6.61	28.81
330771	-	off	20	1	0.013	8.06	0.42	6.06	36.00
330650	-	off	25	1	0.009	1.52	0.55	6.06	4.00
330649	-	off	20	3	0.011	1.79	0.42	6.62	0.64
330643	-	off	10	1	0.154	4.29	0.15	6.99	25.67
330560	-	off	40	1	0.007	0.69	0.93	4.84	0.03
330559	-	off	45	1	0.005	0.89	1.04	5.86	0.04
330558	-	off	50	1	0.005	0.54	1.10	4.66	0.24
330551	-	off	35	1	0.005	1.75	0.81	17.47	0.03
330551	-	off	45	1	0.009	0.85	1.05	5.76	0.03
330412	-	off	40	1	0.012	2.07	0.89	5.04	49.33
330392	-	off	80	1	0.007	0.33	1.79	3.50	26.10
330391	-	off	50	6	0.012	1.00	1.08	4.78	12.39
330390	-	off	40	1	0.004	1.76	0.89	5.05	2.32
330332	-	off	10	1	0.170	3.94	0.12	6.56	30.19
330328	-	off	15	1	0.056	4.21	0.25	6.65	19.78
330327	-	off	18	1	0.044	4.63	0.39	6.42	15.13
330325	-	off	25	1	0.014	4.02	0.55	5.79	13.26

A.3 Data set comparison

Figure A.4 shows the reconstructed energy and energy resolution for the single pion runs and the merged data sets. The merged sets were spit into events with even and odd event numbers to get two statistically independent data samples. All data sets are in agreement with each other, justifying the merging and splitting.

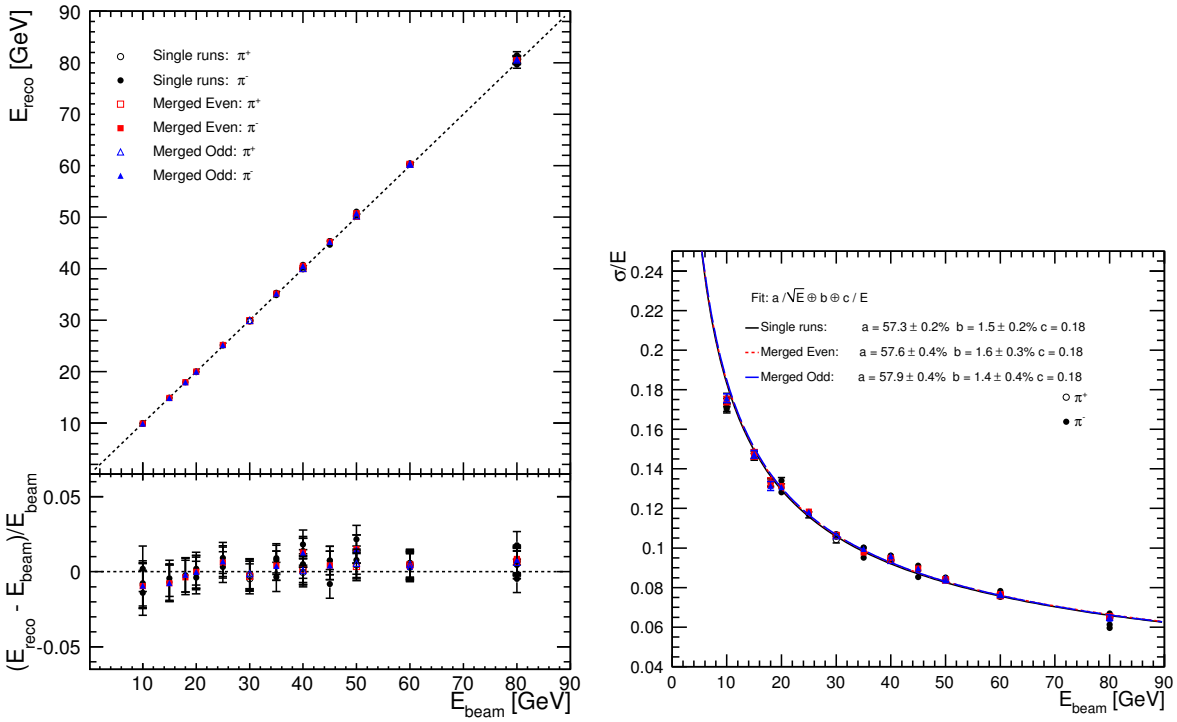

Figure A.4: Initial reconstructed energy and energy resolution comparison between the single test beam runs and the merged and in afterwards split runs at different beam energies.

Figure A.5 shows the reconstructed energy and energy resolution for the data set with even event numbers of both π^+ and π^- events. Due to the smaller available energy range of π^+ runs and for a better visibility of the different data sets of π^- events, they are not shown in Chapter 4.

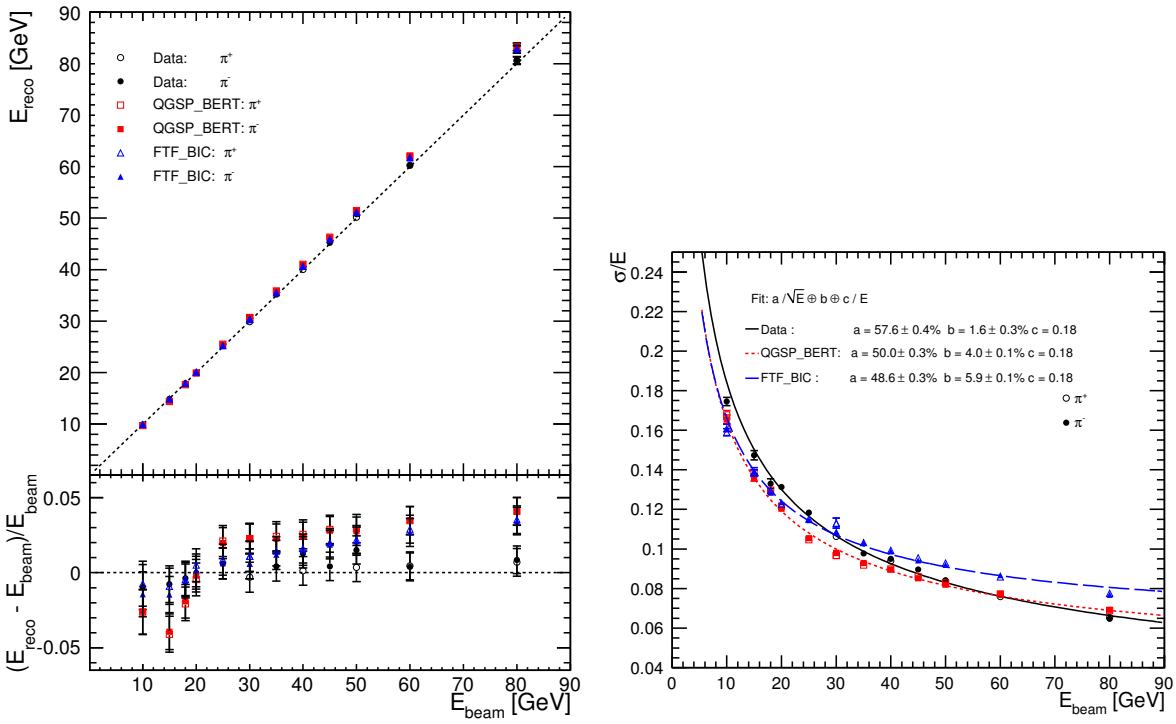

Figure A.5: Initial reconstructed energy and energy resolution of test beam data (black circles) and simulation of the physics list QGSP_BERT (red squares) and FTF_BIC (blue triangles) for merged π^+ and π^- runs.

A.4 Global software compensation using energy density dependent weights

The reconstructed energy of the test beam data using the global software compensation E_{reco} resulted in non-flat beam energy dependence, see Figure A.6. Therefore the reconstructed energy of test beam data was corrected using

$$E_{\text{corr}} = E_{\text{reco}} - (m \cdot E_{\text{reco}} + n).$$

The function $(m \cdot E_{\text{beam}} + n)$ is shown in figure A.6 illustrated by the black line. The corrected reconstructed values are shown in Subsection 4.4.4. Figure A.7 shows the energy resolution of the uncorrected software compensated energy.

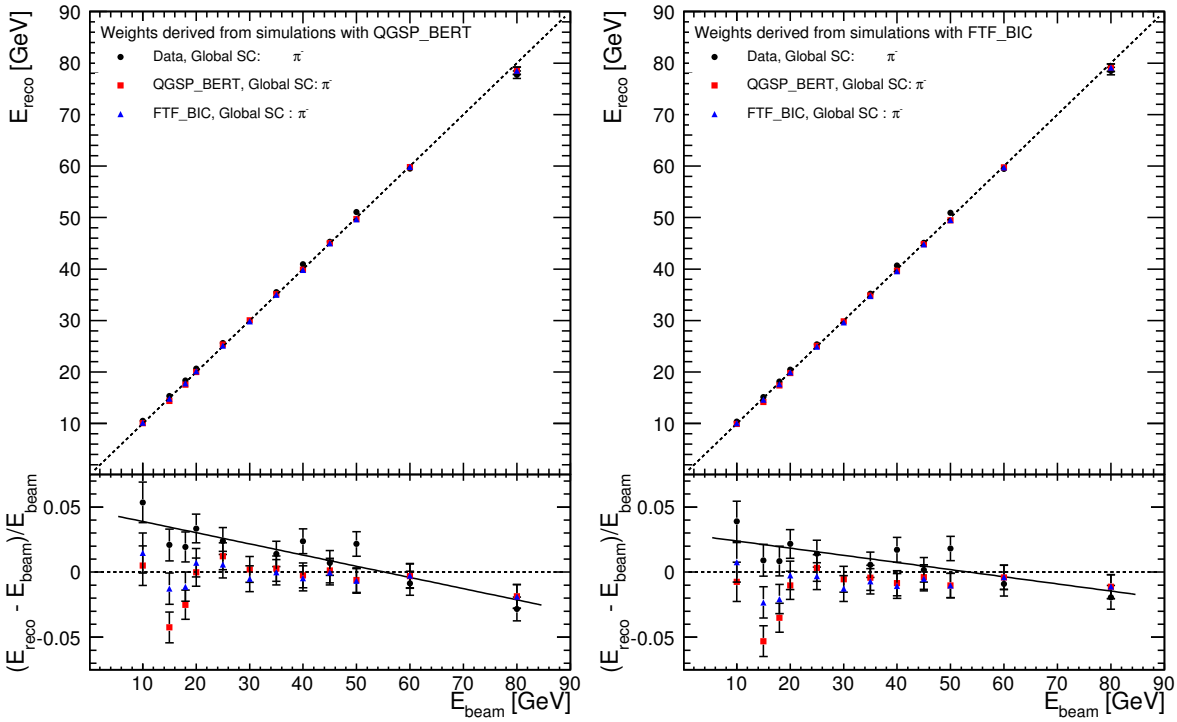

Figure A.6: Reconstructed energy of test beam data simulated data for the global software compensation technique based on energy density weighting for weight parameterizations using simulations with physics lists QGSP_BERT (*left*) and FTF_BIC (*right*). The linearity is distorted due differences in the initially reconstructed energy shown in Figure 4.13.

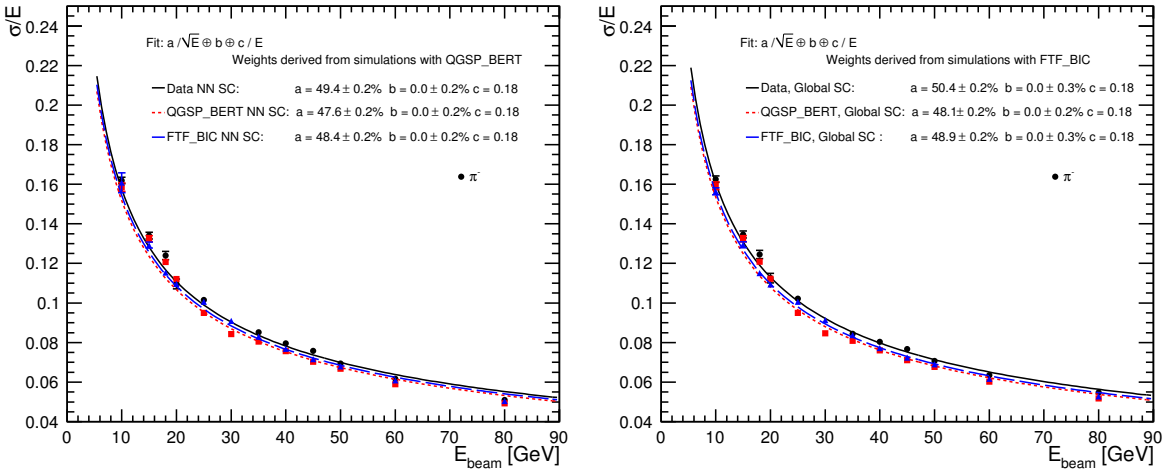

Figure A.7: Energy resolution of test beam and simulated data for the global software compensation technique based on energy density weighting for weight parameterizations using simulations with physics lists QGSP_BERT (*left*) and FTF_BIC (*right*) without the correction of test beam data.

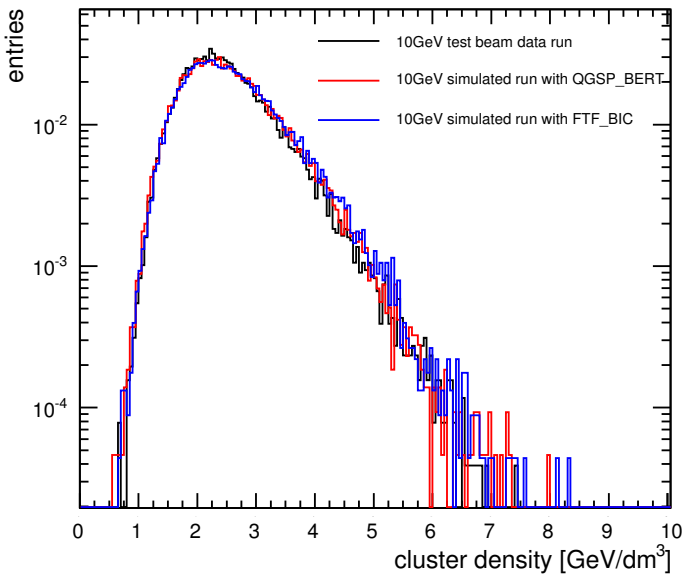

Figure A.8: Cluster energy density distributions for test beam data and simulated data with the physics lists QGSP_BERT and FTF_BIC. The pion energy was 10 GeV.

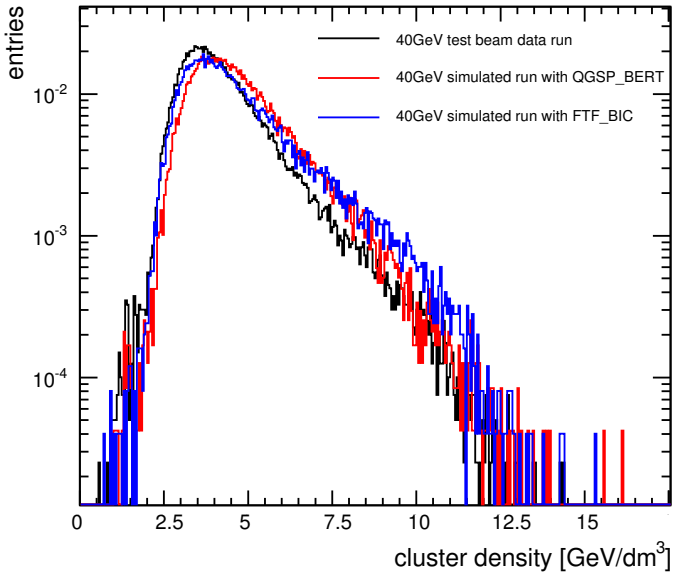

Figure A.9: Cluster energy density distributions for test beam data and simulated data with the physics lists QGSP_BERT and FTF_BIC. The pion energy was 40 GeV.

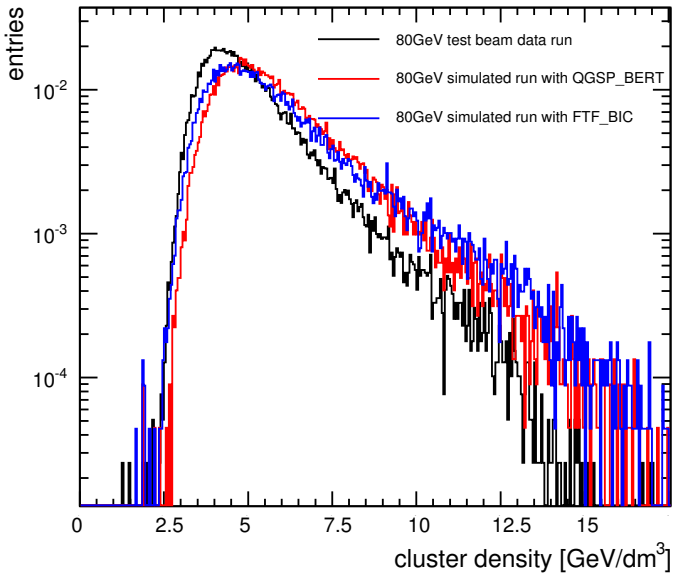

Figure A.10: Cluster energy density distributions for test beam data and simulated data with the physics lists QGSP_BERT and FTF_BIC. The pion energy was 80 GeV.

A.5 Global software compensation using a neural network

The reconstructed energy E_{reco} of the test beam data using the neural network resulted in a non-flat beam energy dependence, shown in Figure A.11. Therefore the reconstructed energy of test beam data was corrected using

$$E_{\text{corr}} = E_{\text{reco}} - (m \cdot E_{\text{reco}} + n).$$

The function $(m \cdot E_{\text{beam}} + n)$ is shown in figure A.11 by the black line. The corrected reconstructed values are shown in Subsection 4.4.5. Figure A.12 shows the energy resolution of the uncorrected software compensated energy.

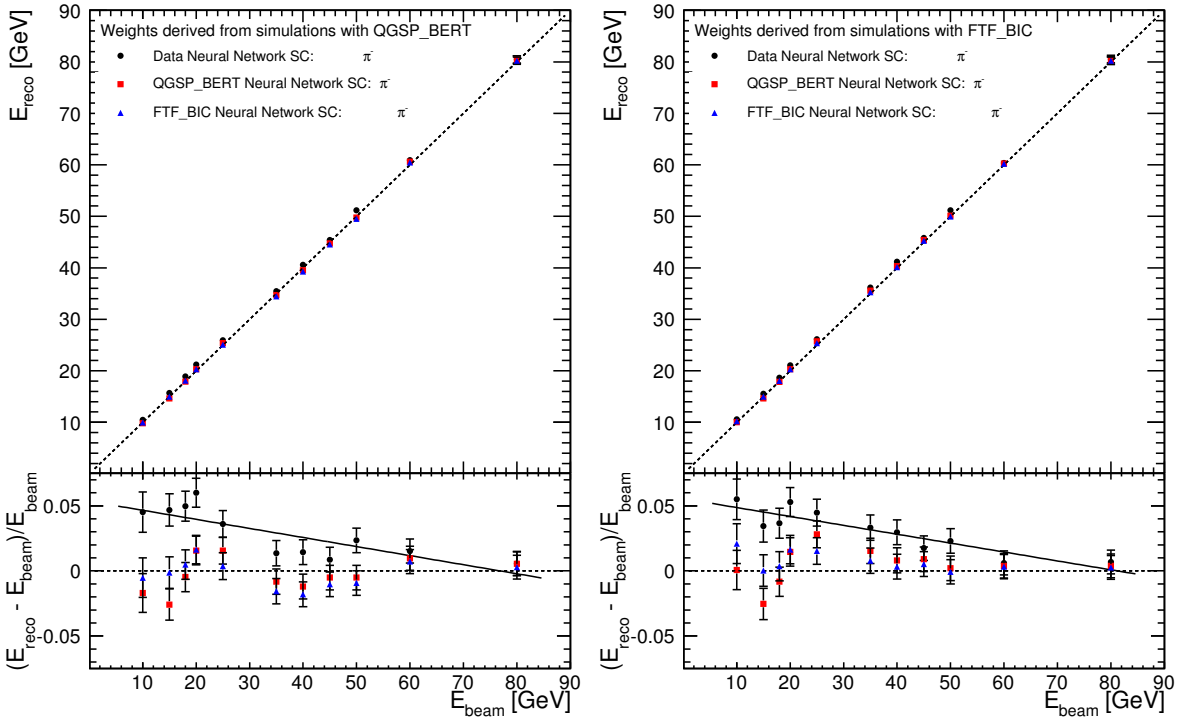

Figure A.11: Reconstructed energy of test beam and simulated data for the global software compensation based on a neural network approach using simulations with physics lists QGSP_BERT (*left*) and FTF_BIC (*right*). The linearity is distorted due differences in the initially reconstructed energy shown in Figure 4.13.

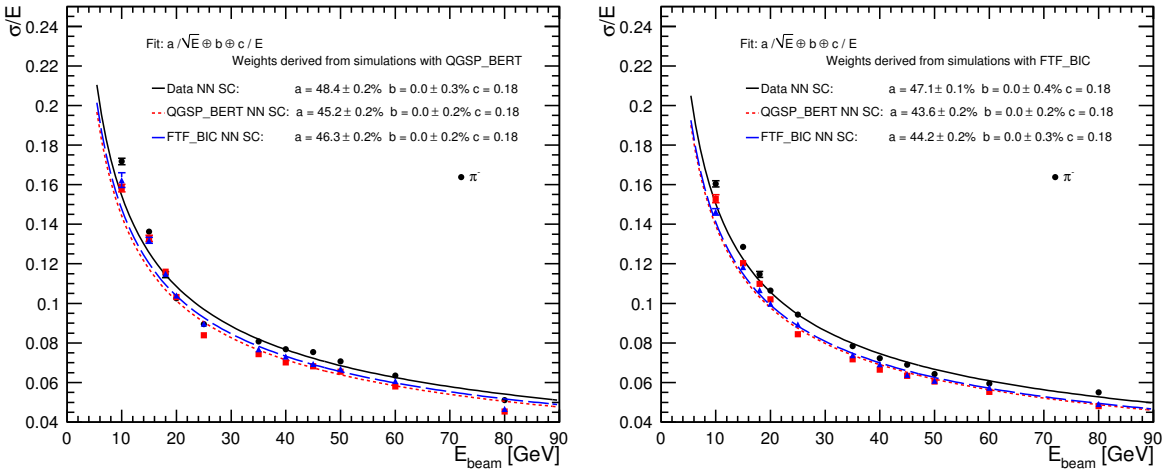

Figure A.12: Energy resolution of test beam data and simulated data for the global software compensation based on a neural network approach using simulations with physics lists QGSP_BERT (*left*) and FTF_BIC (*right*) without the correction of test beam data.

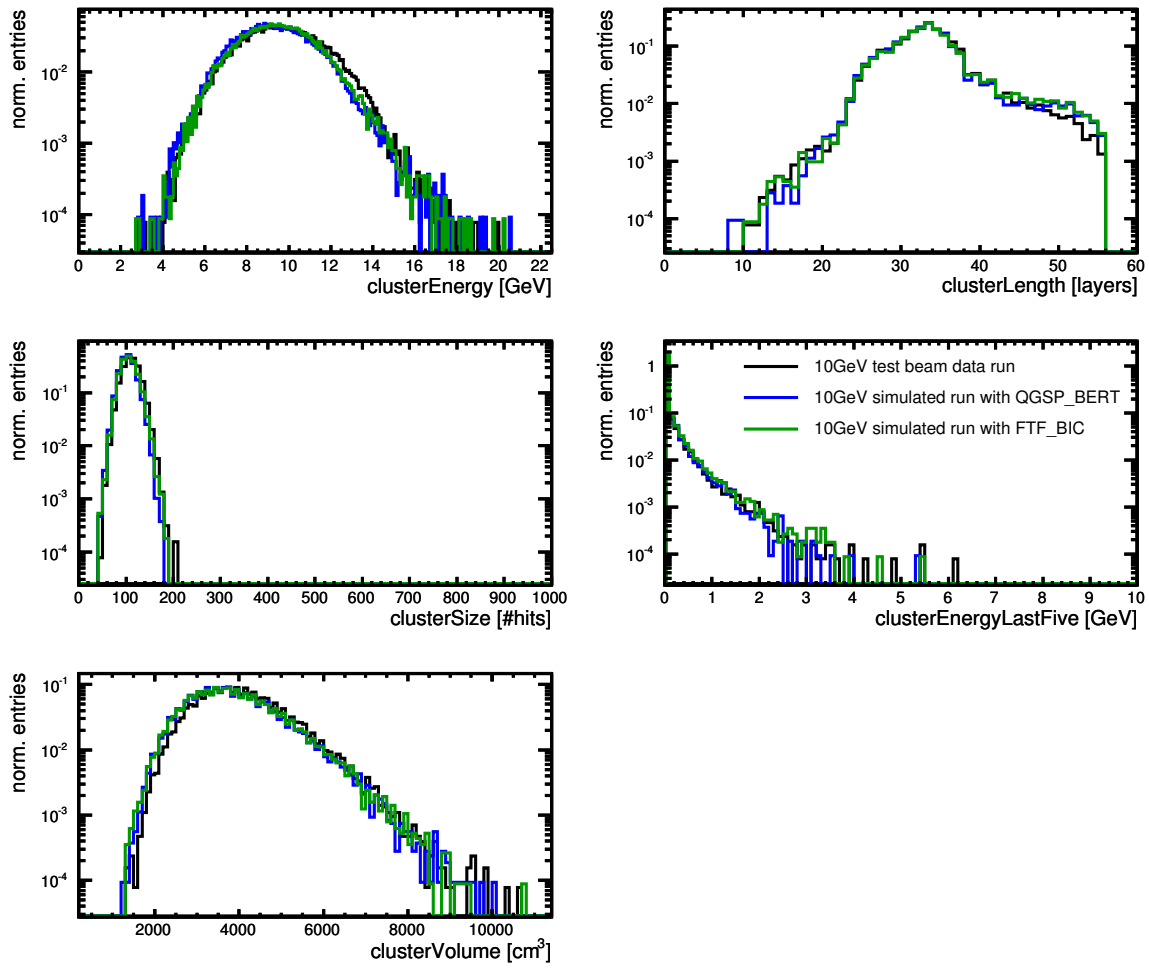

Figure A.13: Cluster variables distributions for test beam data and simulated data with the physics lists QGSP_BERT and FTF_BIC for particles with an energy of 10 GeV. At this energy simulated data shows a typically lower volume and lower reconstructed energy.

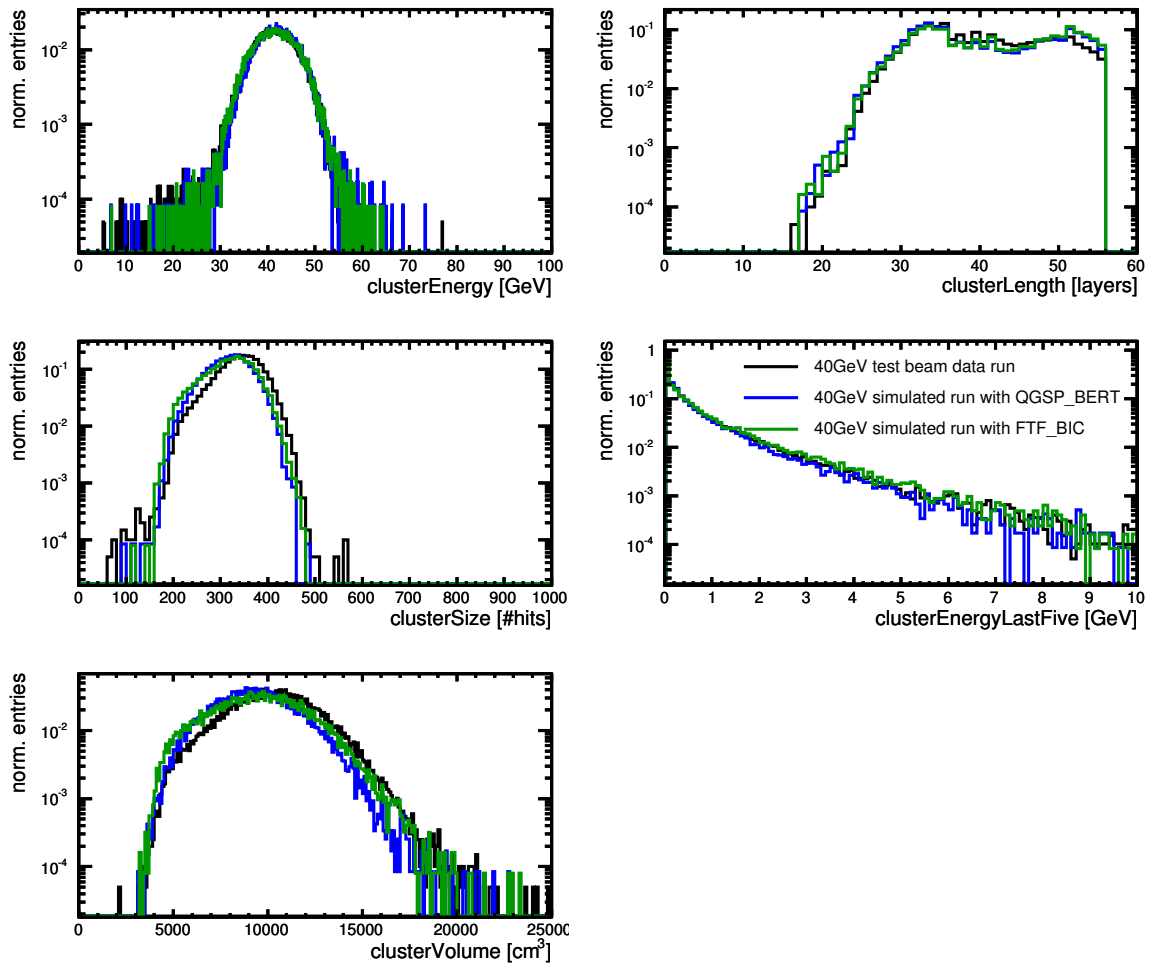

Figure A.14: Cluster variables distributions for test beam data and simulated data with the physics lists QGSP_BERT and FTF_BIC for particles with an energy of 40 GeV. At this energy simulated data shows a higher energy density due to a typically lower volume and higher reconstructed energy.

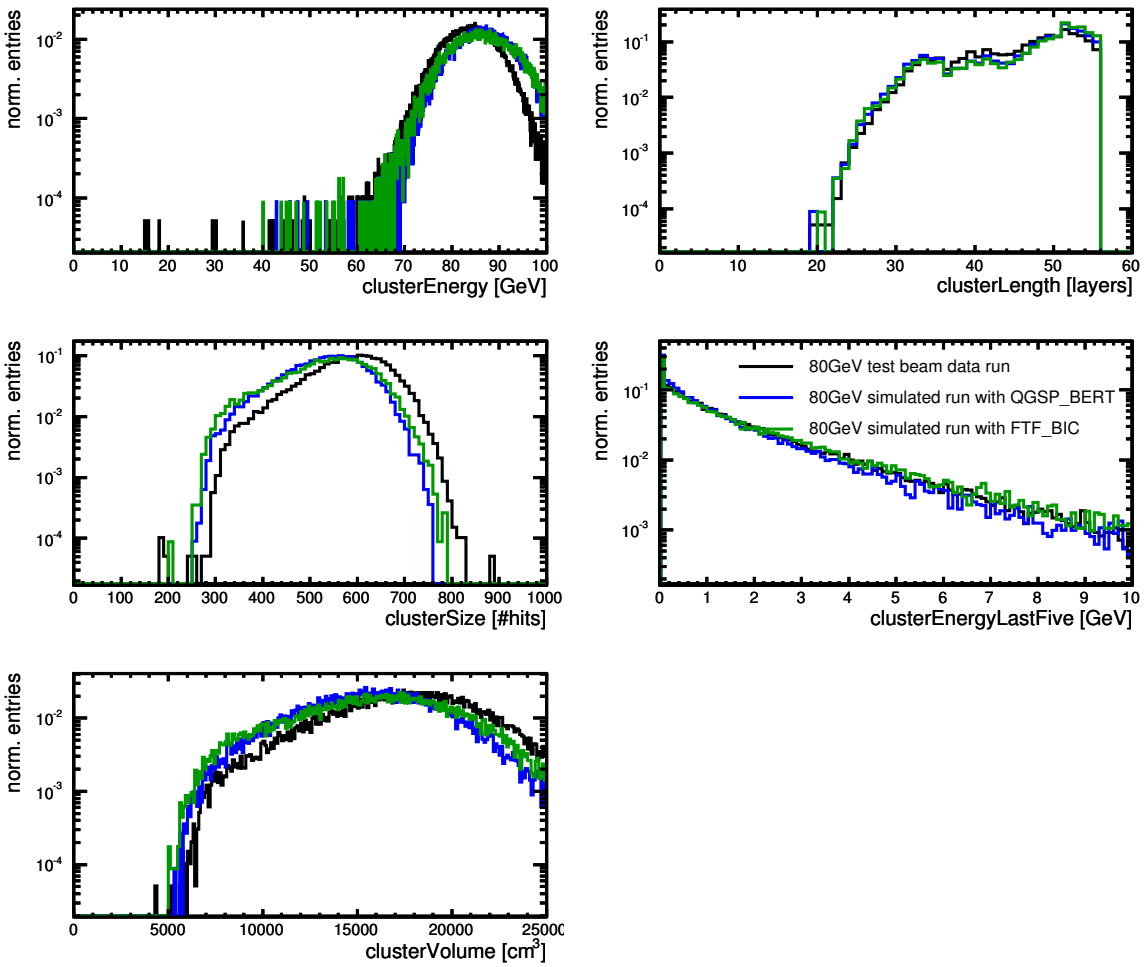

Figure A.15: Cluster variables distributions for test beam data and simulated data with the physics lists QGSP_BERT and FTF_BIC for particles with an energy of 80 GeV. At this energy simulated data shows a typically lower volume and lower reconstructed energy.

Appendix B

Additional information for software compensation in ILD

B.1 Software Compensation in the PandoraPFA framework

In this appendix section a more detailed description of the PandoraPFA algorithm, framework and possible user modifications are given. Since 2009 PandoraPFA has gone through an extensive redesign and reimplementation. During the redesign phase, the software was essentially rewritten from scratch, following modern programming standards. The PandoraPFA performance, described in [58], was recovered and new features were implemented [97]. The following information is based on the redesigned PandoraPFA package and its user applications[1].
For an easier understanding the main objects used in PandoraPFA are explained:

Hit/CaloHit is a calorimeter hit in the PandoraPFA framework. The following informations are associated to a hit, which are filled and different stages of the PandoraPFA algorithms: calibrated energy (MIP equivalent, electromagnetic and hadronic scale), position and normal vectors, absorber material in front of the cell, time of first energy deposition, layer, hit type, depending on calorimeter and detector region, surrounding energy. The different energy scales are kept for a hit until an algorithm classifies the final origin of a hit.

Tracks in the PandoraPFA framework are based and constructed from dedicated tracking algorithms for the tracking sub-detector, like the TPC and Vertex detectors. The used tracking algorithms are not part of PandoraPFA. Further information is associated to the tracks: 2-D impact parameters, Momentum, particle mass, charge sign, start track state, end track state.

Clusters are groups of calorimeter hits, which are collected with cluster algorithms, which are part of the PandoraPFA framework. Clusters contain the following information: list of constituent CaloHits, MIP fraction, electromagnetic and hadronic energy measure, initial direction, current direction, energy-weighted centroid, shower max layer, list of associated tracks.

[1] The code can be found at http://svnsrv.desy.de/viewvc/PandoraPFANew/

PFO is the short notation of a Particle Flow Object. A PFO is the final created object of charged or uncharged particle. The following informations are associated to PFOs: PDG code, charge sign, mass, energy, momentum, list of tracks, list of clusters. Uncharged PFOs have an empty track list.

The defined objects are used in the different PandoraPFA algorithm steps, which are explained in the following:

The particle flow algorithm PandoraPFA: The idea of PandoraPFA was given in Section 2.5, which is to reconstruct the four-vectors of all particles in each event. The particle energies are measured with the sub-detector system or with a combination of these sub-detector systems, which gives the best estimate. The starting point of PandoraPFA are tracks and CaloHits.
With track selection and topology algorithms track topologies, such as kinks and decays of neutral particles, are identified. In the calorimeters isolated hits, based on their distance to other hits, are removed for the first clustering stage.
The main clustering algorithm is based on a forward projective cone method and works from innermost to outermost layer of the electromagnetic and hadronic calorimeter. Cluster seeds are the projections of reconstructed tracks on the front face of the electromagnetic calorimeter. In the algorithm, calorimeter hits are either added to a cluster or are identified as seeds for new clusters. The cluster algorithm is designed in a way that it rather splits true clusters than to collect hits from independent energy deposits. Thus, it is more likely to end up with many small clusters that originally belonged to energy depositions of one particle than to have few large clusters that are the energy depositions of many particles. Therefore an algorithm to merge clusters is performed on the basis of topological signatures in the high granular calorimeters.
In the following a statistical reclustering is performed if an inconsistent pairing between track and cluster(s) are identified. The reclustering algorithm calculates the goodness of the track and cluster pairing, performs a clustering with changed parameters and/or another clustering algorithm, calculates the figure of merit for the consistency of the track to new cluster association, repeats the previous two stages if necessary and chooses the best pairing. The reclustering algorithm is especially important for high center-of-mass energies of multiple tracks are associated to a single cluster. For example if two tracks point to a single cluster with an energy higher than both track energies, the reclustering algorithm tries to split the cluster in an appropriate way. Also, if a single track points to a single cluster with higher energy, the reclustering algorithm checks if the cluster has to be split to a cluster belonging to the track and a cluster belong to a neutral particle, which has no associated track. Another example is, if a track energy is associated to a cluster with a much higher energy. Then the algorithm looks for a further cluster nearby and merges the clusters if necessary.
Photons are identified with a special clustering algorithm, which disables the track

seeds, in combination with shower profile based algorithms. One of the final steps is the removal of identified neutral clusters, which are, in fact fragments of charged particle hadronic showers. The final step is the so called particle flow object creation, i.e. the creation of fully reconstructed particles. A particle flow object contains the full four moments and a list of associated tracks and clusters.

The PandoraPFA framework: The particle flow algorithm PandoraPFA is a standalone framework, which could be used in principal for any high energy 4π detector. It was developed and tuned for the ILD and the CLIC_ILD detector geometries. The framework is connected to the specific data structures and detector geometries via a user application (in case if ILC: MarlinPandora). This user application converts the input (calorimeter hits, tracker hits, tracks and the detector geometry) to a format usable by PandoraPFA. Parts of the created objects were explained at the beginning of this section. Once the user has passed all necessary track, hit and geometry information to the client application, PandoraPFA can be treated as a black box with its default settings. The main feature of the PandoraPFA redesign is the user possibility to make well controlled changes to the default PandoraPFA settings, for example by switching off specific algorithms or by changing algorithm parameters. It is also possible to implement user algorithms via the client application MarlinPandora without changing the PandoraPFA code.

Default hadronic energy correction algorithms: Several energy correction algorithms already exist in the PandoraPFA framework and all help to correct the hadronic energy of a cluster. These corrections functions are called within the framework, so that actions in the reclustering step may cause a further application of one of these functions.

User hadronic energy correction algorithms: A user can develop own energy correction functions. Such a correction can be applied like the default energy correction functions within the framework. If not specified different such a correction is applied to all hadronic clusters. Since the final PFO energy of charged hadrons is mostly estimated from the track and not from the cluster information, there is no direct impact on this particles. But such a correction may change the behavior of the track-cluster associations algorithms. Since it is not decided at every step if a cluster belongs to the energy deposition of a charged or uncharged particle such a energy correction function should either be applied on very specific cluster types or should work for all types of clusters.

Another possibility is to apply a cluster energy correction function after the main part of PandoraPFA is done. At this stage PFOs are formed and a cluster energy correction only needs to be applied to the neutral hadrons, since for charged hadrons the energy estimate is taken from the track information.

Determination of software compensation weights: As explained above a user energy cor-

rection function, such as software compensation, can be added to PandoraPFA in different ways. Weights for a software compensation algorithm, which are applied to clusters after the main PFO creation, will affect the energy determination of neutral hadrons only. Therefore they should be determined from such particles, thus mainly neutrons and neutral kaons. A software compensation technique inside the PandoraPFA framework itself will act on all types of hadronic clusters, therefore weights should be determined from charged and uncharged hadrons, or, as a first approximation, only from charged particles, since they carry the majority of the energy in typical events.

B.2 Changes to the default settings of PandoraPFA

In the default settings of MarlinPandora[2] the maximum allowed hit energy in the hadronic calorimeter is 1 GeV. This creates a saturation or compensation of hadronic clusters. All hits of a cluster, which is classified as a hadronic one, are scaled down to one. The resulting saturation in the energy response is shown in Figure B.1. Furthermore, the energy resolution is deteriorated for such a settings. For a software compensation algorithm to work, the full range of energy densities and therefore hit energies needs to be accessible. Therefore the maximal hadronic hit energy in the hadronic calorimeter was set to 10000 GeV, which is far above a realistic maximum hit energy in the hadronic calorimeter. The reconstructed energy no longer saturates for high energies and the energy resolution shows the expected particle energy dependence. All comparisons of energy resolutions for single particles are therefore done with a settings of `<parameter name="MaxHCalHitHadronicEnergy" type="float">10000.</parameter>`[3], to clearly see the differences in single particle energy resolution over the full energy range. Instead, the results for the jet energy resolution with software compensation techniques are compared with the default PandoraPFA settings, i.e. the maximum hadronic hit energy in the hadronic calorimeter is set to one. PandoraPFA is tuned for a best result with the default settings, thus any modifications needs to be compared to the default.

[2] MarlinPandora is the user application which connects PandoraPFA which the ILC input/output framework LCIO

[3] Steering file flag

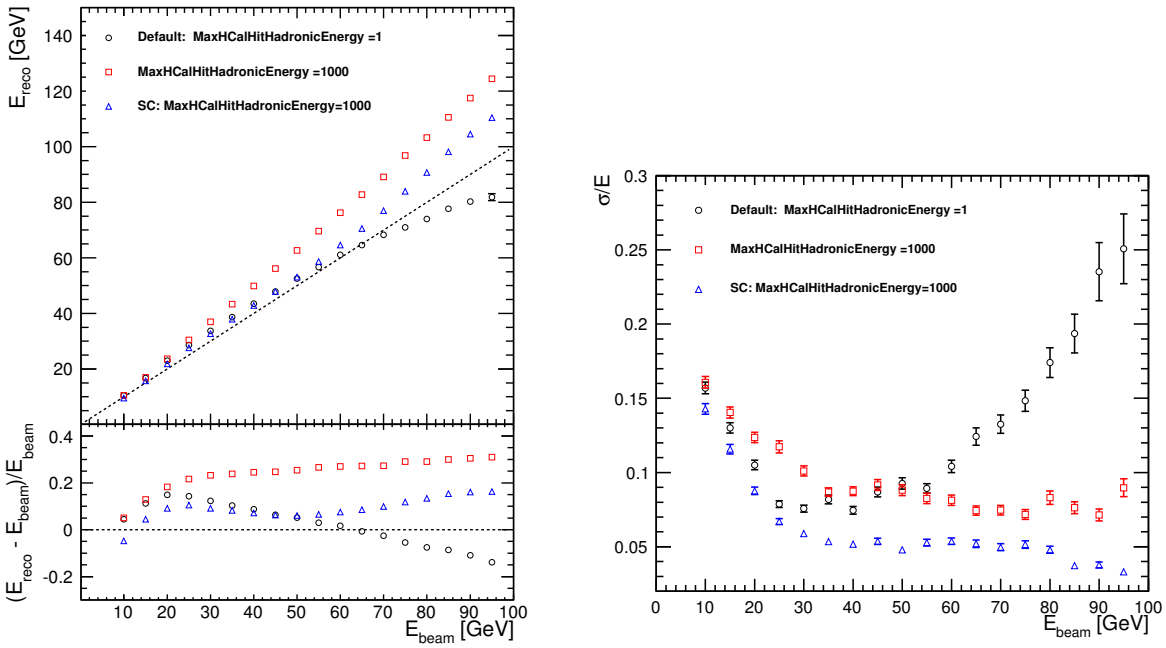

Figure B.1: Reconstructed energy (*left*) and energy resolution (*right*) for single neutral particles in the ILD detector. The open black circles show the default reconstruction behavior of PandoraPFA. Due to the constraint that a single hadronic hit can maximal have the energy of 1 GeV the relative difference between reconstructed and initial particle energy decreases with increasing particle energy and the energy resolution gets significantly degraded. Without this constraint, i.e. with a very high maximal hadronic hit energy threshold, the expected energy resolution behavior of the calorimeter is restored as shown by the open red squares. The difference between reconstructed and initial particle energy is relatively flat above 30 GeV. However, the particles are reconstructed to too high energies, due to the use of wrong calibration values with the change of settings. Invoking software compensation, shown by the open blue triangles, helps to improve the energy reconstruction and energy resolution.

B.3 Software of ILD reconstruction

ILCSoftware version	v01-11
Mokka	mokka-07-06-p02
Geant4	9.3.p02
Marlin	v01-00
MarlinReco	v00-20
MarlinPandora	v00-05
PandoraPFA	v00-06
PandoraAnalysis	v00-02
gear	v00-07
lcio	v01-51-02

Table B.1: Software version used for the ILD event reconstruction.

Appendix C

Additional information for the top mass analysis

C.1 Flavor Tagging Input Variables

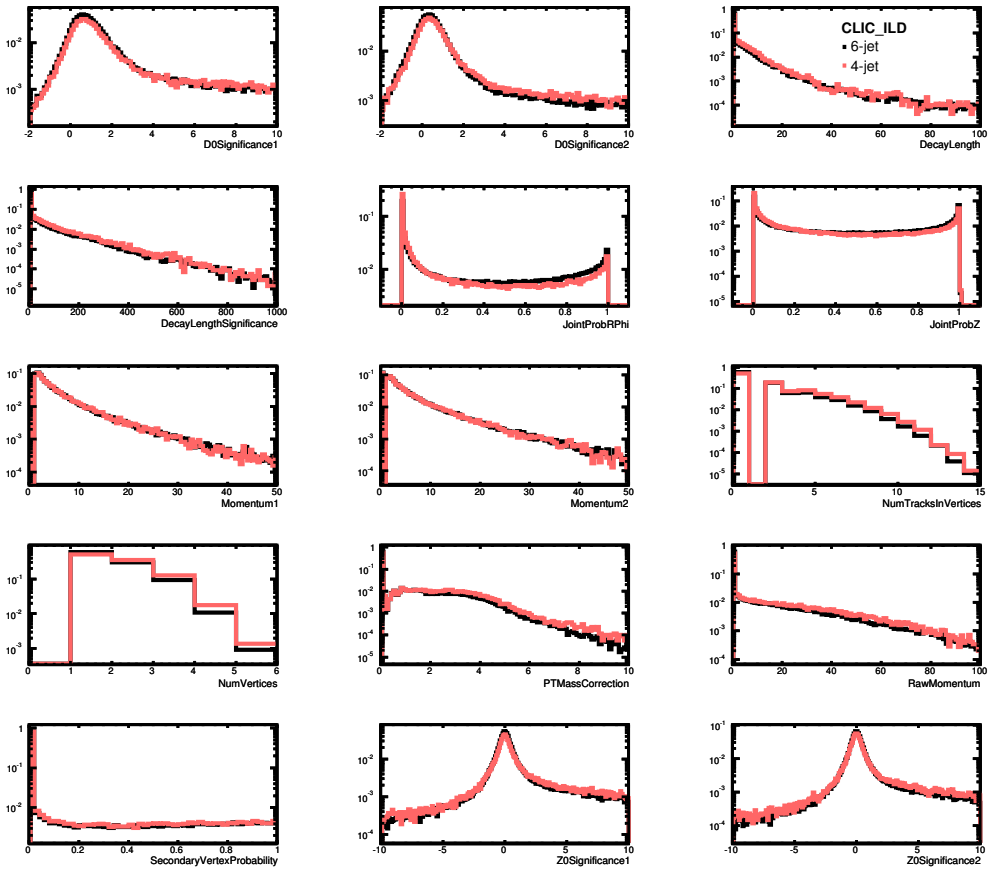

Figure C.1: Input variabls of the flavour tagging algorithms.

Table C.1: Names and description of the input variables for the neural network of the LCFI Flavor Tagging package

D0 Significance 1	The two most significant tracks in the $r-\varphi$ plane are found for each jet. Impact parameter significance of first vertex track.
D0 Significance 2	The two most significant tracks in the $r-\varphi$ plane are found for each jet. Impact parameter significance of second vertex track.
Decay Length	The distance from the primary vertex to the furthest secondary or tertiary vertex.
Decay Length Significance	The distance from the primary vertex to the furthest secondary or tertiary vertex, divided by its measurement error.
JointProbRPhi	Probability that all the tracks of the given jet come from the primary vertex in the $r-\varphi$ plane.
Joint ProbZ	Probability that all the tracks of the given jet come from the primary vertex in the z direction.
Momentum 1	The two most significant tracks in the $r-\varphi$ plane are found for each jet. Momentum of first vertex track.
Momentum 2	The two most significant tracks in the $r-\varphi$ plane are found for each jet. Momentum of second vertex track.
Number Track in Vertices	Number of tracks in all non primary vertices.
Number of Vertices	Number of vertices found in the given jet.
PT Mass Correlation	The p_{T} corrected vertex invariant mass. It is the most powerful variable to distinguish between b and c quarks.
Raw Momentum	Vertex momentum.
Secondary Vertex Significance	Probability that all tracks in the secondary vertex are consistent with being generated at the same vertex.
Z0 Significance 1	The two most significant tracks in the are found for each jet. Impact parameter significance z direction of first vertex track.
Z0 Significance 2	The two most significant tracks in the are found for each jet. Impact parameter significance z direction of second vertex track.

C.2 Lepton and Jet angle and energy resolution

The energy and angular resolutions of leptons and jets were studied by comparing the reconstructed objects to the generator level values. In the case of jets, the comparison was made with respect to quarks. Here, a jet was associated to one specific quark if it was closest to that particular jet, and it was required that this procedure led to unique assignments of all jets and leptons in the event to generator-level particles. This unique assignment was successful for 58% of all fully-hadronic events and for 65% of all semi-leptonic events. These numbers can also be taken as an indication of the success of the jet clustering, and put the failure rates of the kinematic fit (often due to reconstruction issues) into perspective.
The angular resolution of the leptons and jets, as well as the energy resolution of the leptons (averaged for electrons and muons for simplicity) were used as parameters for the kinematic fit. The significant overlap between jets in the dense multi-jet environment of $t\bar{t}$ events results in a degradation of the single jet energy resolution. However, since the mis-reconstruction of the jets in an event are correlated, this resolution does not correctly reflect the effect on the invariant mass resolution, and thus can not be used as parameter in the kinematic fit. Instead, the single jet resolution for di-jet events was used.

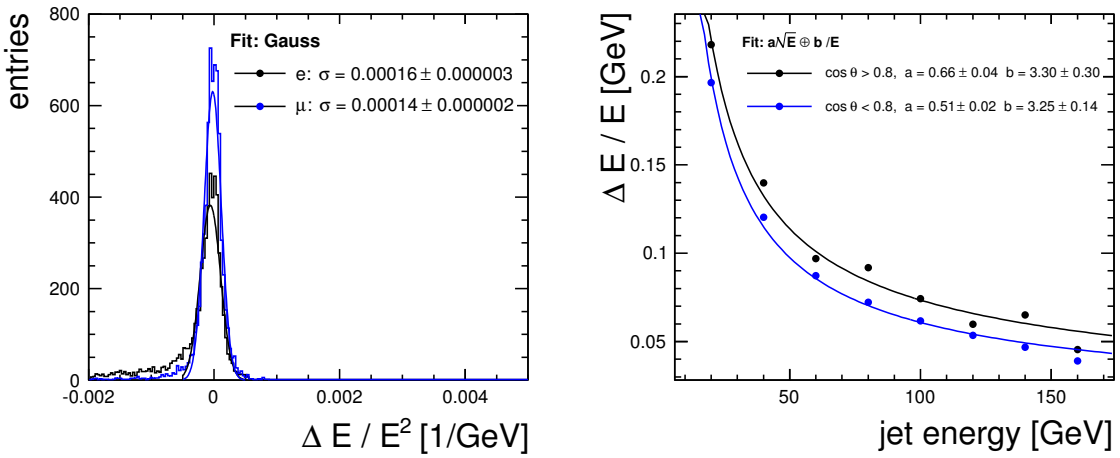

Figure C.2: Energy resolution of leptons (*left*) and jets (*right*). An error function of $\sigma_E = 1.5 \cdot 10^{-4} \cdot E_l$ was chosen for for types leptons.

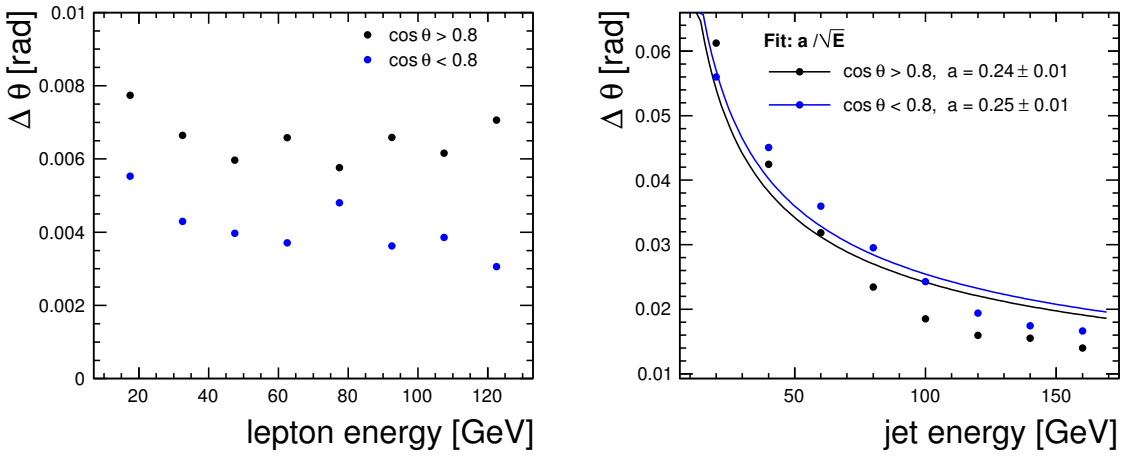

Figure C.3: Angular resolution of θ for leptons and jets. An error of $\sigma_\theta = 5\,\text{mrad}$ was chosen for for types leptons.

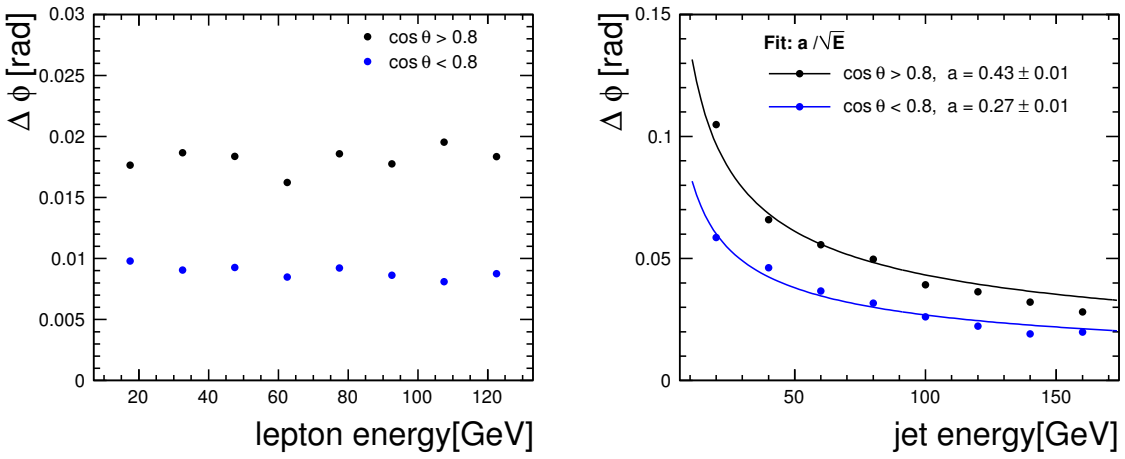

Figure C.4: Angular resolution of ϕ for leptons and jets. An error of $\sigma_\phi = 15\,\text{mrad}$ was chosen for for types leptons.

C.3 PDF parameters

A complete list of the parameters of the final mass fit.
Background pdf:

- $p_0 = 100$, fixed
- $p_1 = 0.37 \pm 0.03$

for the 6-jet event sample and

- $p_0 = 100$, fixed
- $p_1 = 0.48 \pm 0.05$

for the 4-jet event sample.
Signal pdf:

- $m_1 = -0.61 \pm 0.10,\ \ s_1 = 3.11 \pm 0.26$
- $m_2 = 1.19 \pm 0.23,\ \ s_2 = 2.44 \pm 0.11$
- $m_3 = 21.45 \pm 3.46,\ \ s_3 = 4.01 \pm 0.28$
- $f_1 = 0.20 \pm 0.04,\ \ f_2 = 0.43 \pm 0.03$
- $m_{tail} = 231.14 \pm 1.60,\ \ s_{tail} = 16.00 \pm 2.06$

for the 6-jet event sample and

- $m_1 = -0.47 \pm 0.11,\ \ s_1 = 4.04 \pm 0.20$
- $m_2 = 1.46 \pm 0.29,\ \ s_2 = 2.36 \pm 0.10$
- $m_3 = 16.06 \pm 3.28,\ \ s_3 = 2.60 \pm 0.14$
- $f_1 = 0.28 \pm 0.03,\ \ f_2 = 0.36 \pm 0.02$
- $m_{tail} = 237.74 \pm 1.03,\ \ s_{tail} = 14.84 \pm 1.18$

for the 4-jet event sample.

C.4 Comparision with ILD LoI results

For the comparison of the $t\bar{t}$ analysis at CLIC, presented in this thesis, with the one at ILC, presented in the ILD LoI [88], the results were used and compared in Figure C.5. Both studies correspond to an integrated luminosity of $100\,\mathrm{fb}^{-1}$. The distributions show that in the case of a full-hadronic top event decay ($t\bar{t} \to bq\bar{q}bq\bar{q}$) the CLIC_CDR results gives a slightly narrower and higher peak of the top quark mass with similar statistics, showing comparable overall efficiency. Also the non-$t\bar{t}$ background is lower in the CLIC case. For the semi-leptonic decay channel ($t\bar{t} \to bq\bar{q}bl\nu_l$) the peak is nearly twice as high, but also broader than the ILD LoI top mass peak. The physics background is comparable. The most likely reason for this difference is the introduction of a neutrino fit object in MarlinKinFit as explained section 6.3.5, which results in a higher success rate of the fit. However, the more difficult beam background and beam energy conditions at CLIC result in an increased uncertainty of the neutrino energy.

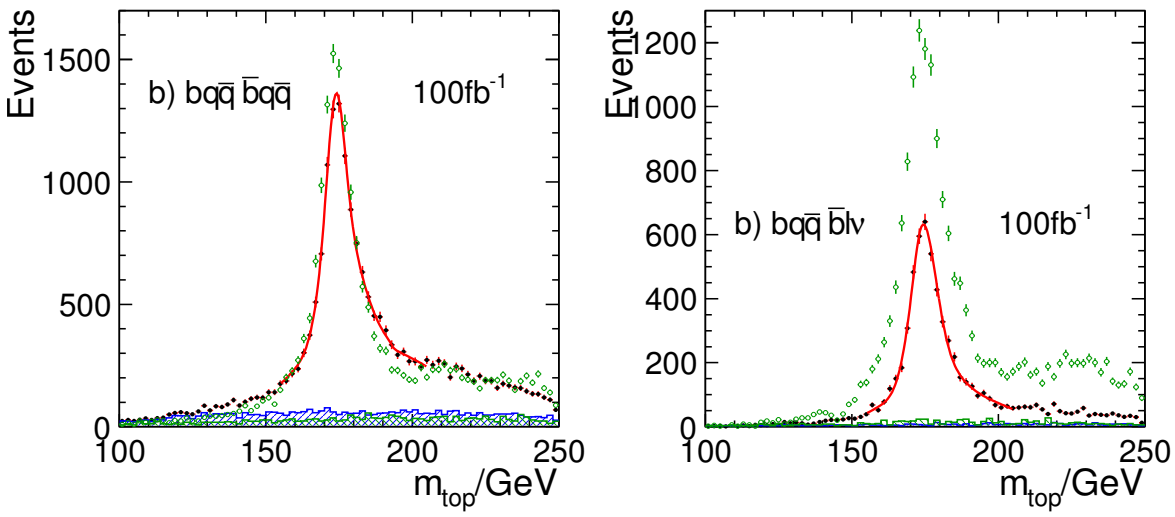

Figure C.5: Comparision with the results of the ILD LoI.
The black points show the top mass distribution obtained for the $t\bar{t}$ analysis of the ILD_LoI. The blue histogram shows the physics background of the distribution and the red line represents the final fit. The green points and the green histogram show the top mass distribution and the physics background respectively for the CLIC_CDR analysis.

To study if the final fit is the only reason for the difference between generator top mass and width and final CLIC CDR results, the fit used in the ILD LoI was tested as well. The ILD LoI fit is a binned χ^2 fit of tree steps:

1. Fit of physical background events only with a polynomial of order 2.

2. Fit of signal events only with a convolution of a Breit-Wigner and a detector resolution function. For the detector resolution function an asymmetric double Gaussian was chosen. The parameters of the Breit-Wigner were fixed to the generator values of top mass and width of the used sample. For the LoI a high statistics sample corresponding to an integrated luminosity of $2.8\,\mathrm{ab}^{-1}$ was used. For this study a statistically independent signal sample corresponding to $200\,\mathrm{fb}^{-1}$ was used.

3. The third step was the fit of the final top mass distribution with a combination of signal and background fit. In the final fit all parameters defining the shapes of the combinatorial background, physical background and detector resolution function, have been fixed to the fit results of the first two steps. The only free parameters in this fit were therefore the top mass, width and the overall normalization.

The results are shown in Figure C.6 for the fully-hadronic (left) and semi-leptonic (right) event channels. For this Figure C.6 the training samples of signal only events were generated with a top mass of 174.0 GeV and a top width of 1.37 GeV. In Figure C.7 the results are shown for the full-hadronic (left) and semi-leptonic (right) event channels using a training sample with generated top mass of 175.0 GeV and width of 1.5 GeV. The obtained values using the LoI fit for the top mass determination are generally 0.5 % smaller than for the fit described in Subsection 6.3.7 and thus are not compatible with a generated top mass of 174 GeV, which used in the final signal sample. The size of the top mass statistical error is approximately the same. Since nearly the same values for the top mass are obtained independent of the generated top mass used in the events for the signal only fit (trainings sample), indicated that no bias from the training samples exists. Concerning the obtained top width the LoI fit results in much smaller values of the fit error. This size of these errors seem to be underestimated in view of the fitted result. The disadvantage of this fit is definitely the smaller fit range.

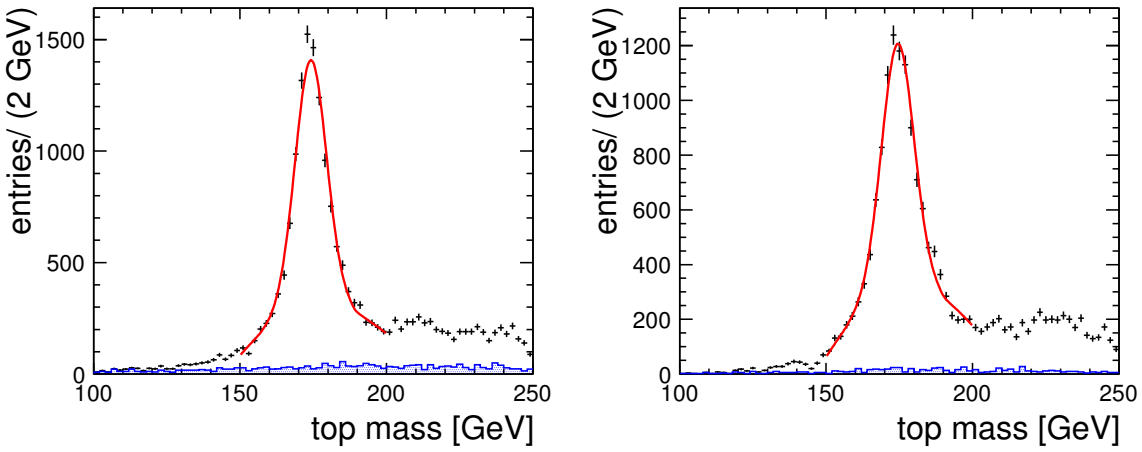

Figure C.6: CLIC top mass distribution (black points) and physics background distribution (blue histogram) with top mass peak fit (red line) obtained with the same fit function used in the ILD_LoI. The signal only fit of step two was done with an event sample of generator top mass of 174.0 GeV and width of 1.37 GeV.
Results for the full-hadronic event sample (*left*): $m_{top} = 173.18\,\text{GeV} \pm 0.10\,\text{GeV}, \sigma_{top} = 1.56\,\text{GeV} \pm 0.07\,\text{GeV}$.
Results for the semi-leptonic event sample (*right*): $m_{top} = 173.50\,\text{GeV} \pm 0.08\,\text{GeV}, \sigma_{top} = 1.65\,\text{GeV} \pm 0.08\,\text{GeV}$.

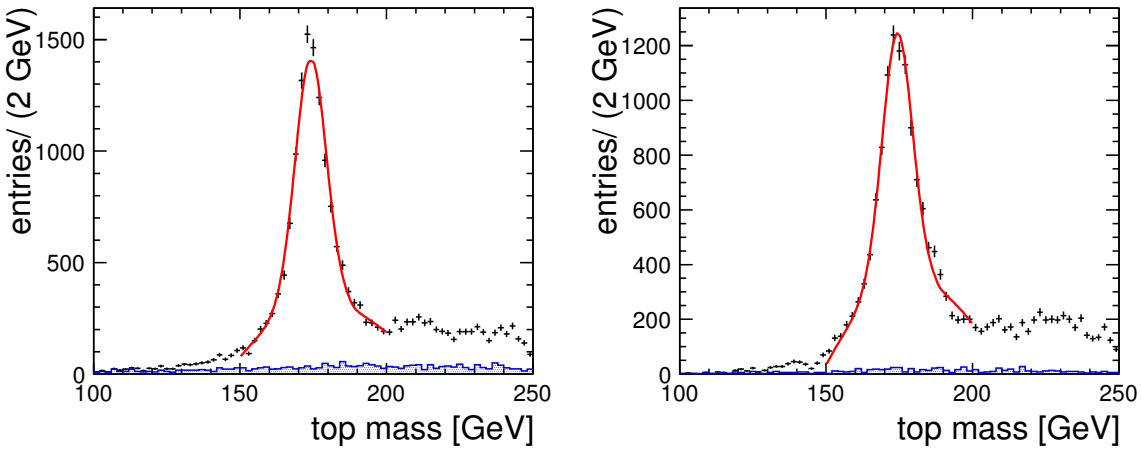

Figure C.7: CLIC top mass distribution (black points) and physics background distribution (blue histogram) with top mass peak fit (red line) obtained with the same fit function used in the ILD_LoI. The signal only fit of step two was done with an event sample of generator top mass of 175.0 GeV and width of 1.5 GeV.
Results for the full-hadronic event sample (*left*): $m_{top} = 173.15\,\text{GeV} \pm 0.08\,\text{GeV}, \sigma_{top} = 1.73\,\text{GeV} \pm 0.08\,\text{GeV}$.
Results for the semi-leptonic event sample (*right*): $m_{top} = 173.33\,\text{GeV} \pm 0.11\,\text{GeV}, \sigma_{top} = 1.55\,\text{GeV} \pm 0.07\,\text{GeV}$.

C.5 Test of the final fit using different event samples

To study the stability of the fit two tests were carried out: Training the fit with a sample with a higher mass, and exchanging training and data sample. In the former case, consistent results with the final fit in the note were obtained, suggesting that no bias from the mass of the training sample exists. In the latter case, opposite shifts in mass were observed as expected. showing reproducible and stable performance of the fit.

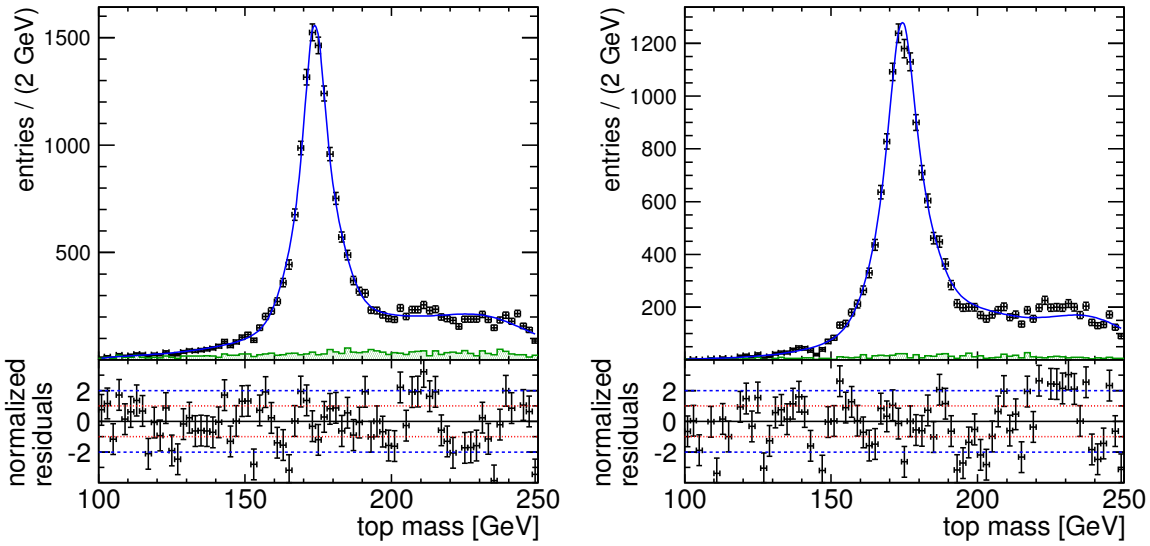

Figure C.8: Final CLIC top mass distribution fitted with pdf described in 6.3.7. For the fit training sample a sample was used with a generated top mass of 175.0 GeV and width of 1.5 GeV. Results for the final full-hadronic sample: $m_{top} = 173.96\,\text{GeV} \pm 0.07\,\text{GeV}, \sigma_{top} = 0.66\,\text{GeV} \pm 0.23\,\text{GeV}$.
Results for the final semi-leptonic sample: $m_{top} = 174.28\,\text{GeV} \pm 0.09\,\text{GeV}, \sigma_{top} = 1.77\,\text{GeV} \pm 0.25\,\text{GeV}$

C.6 Cut Flow Table

The overall signal reconstruction efficiency, combining kinematic fit success rate and rejection with the likelihood technique achieved in the present analysis is comparable to the ILD LoI analysis in the fully-hadronic channel, and even exceeds it in the semi-leptonic channel. The numbers of accepted events in the different analysis branches at various steps in the analysis are summarized in Table C.2. The overall selection efficiency for true fully-hadronic top pair decays in the 6-jet branch was 35%, and the overall efficiency for true semi-leptonic top pair decays in the 4-jet branch was 56%.

$\gamma\gamma \rightarrow$ hadron events overlaid				
	Signal		Background	
Analysis step	6 jet sample	4 jet sample	6 jet sample	4 jet sample
	52780		1014000	
Lepton Finder	30973 (23305 true)	18617 (13619 true)	733421	241672
Kinematic Fit	8701	8230	30718	19776
Background Rejection	8217	7691	1018	400

Table C.2: Summary of the cut flow of the analysis.

Bibliography

[1] A. Salam, "Weak and Electromagnetic Interactions,". Originally printed in *Svartholm: Elementary Particle Theory, Proceedings Of The Nobel Symposium Held 1968 At Lerum, Sweden*, Stockholm 1968, 367-377.

[2] S. L. Glashow, "Partial Symmetries of Weak Interactions," *Nucl. Phys.* **22** (1961) 579–588.

[3] S. Weinberg, "A Model of Leptons," *Phys. Rev. Lett.* **19** (1967) 1264–1266.

[4] P. W. Higgs, "Broken symmetries, massless particles and gauge fields," *Phys.Lett.* **12** (1964) 132–133.

[5] P. W. Higgs, "Spontaneous Symmetry Breakdown without Massless Bosons," *Phys.Rev.* **145** (1966) 1156–1163.

[6] F. Englert and R. Brout, "Broken Symmetry and the Mass of Gauge Vector Mesons," *Phys.Rev.Lett.* **13** (1964) 321–322.

[7] G. Guralnik, C. Hagen, and T. Kibble, "Global Conservation Laws and Massless Particles," *Phys.Rev.Lett.* **13** (1964) 585–587.

[8] T. Kibble, "Symmetry breaking in nonAbelian gauge theories," *Phys.Rev.* **155** (1967) 1554–1561.

[9] S. Dawson, "Introduction to electroweak symmetry breaking," `arXiv:hep-ph/9901280`.

[10] L. Evans and P. Bryant, "Lhc machine," *Journal of Instrumentation* **3** no. 08, (2008) S08001. `http://stacks.iop.org/1748-0221/3/i=08/a=S08001`.

[11] **ATLAS** Collaboration, G. Aad *et al.*, "Expected Performance of the ATLAS Experiment - Detector, Trigger and Physics," `arXiv:0901.0512 [hep-ex]`.

[12] **CMS** Collaboration, G. L. Bayatian *et al.*, "CMS physics: Technical design report,". CERN-LHCC-2006-001.

[13] S. P. Martin, "A Supersymmetry Primer," `arXiv:hep-ph/9709356`.

[14] H. Goldberg, "Constraint on the Photino Mass from Cosmology," *Phys.Rev.Lett.* **50** (1983) 1419.

[15] J. R. Ellis, J. Hagelin, D. V. Nanopoulos, K. A. Olive, and M. Srednicki, "Supersymmetric Relics from the Big Bang," *Nucl.Phys.* **B238** (1984) 453–476.

[16] H. P. Nilles, "Supersymmetry, Supergravity and Particle Physics," *Phys. Rept.* **110** (1984) 1–162.

[17] H. E. Haber and G. L. Kane, "The Search for Supersymmetry: Probing Physics Beyond the Standard Model," *Phys. Rept.* **117** (1985) 75–263.

[18] M. Fukugita and T. Yanagida, "Baryogenesis Without Grand Unification," *Phys. Lett.* **B174** (1986) 45.

[19] **Super-Kamiokande** Collaboration, Y. Fukuda *et al.*, "Measurements of the solar neutrino flux from Super-Kamiokande's first 300 days," *Phys.Rev.Lett.* **81** (1998) 1158–1162, arXiv:hep-ex/9805021 [hep-ex].

[20] B. T. Cleveland, T. Daily, J. Raymond Davis, J. R. Distel, K. Lande, C. K. Lee, P. S. Wildenhain, and J. Ullman, "Measurement of the solar electron neutrino flux with the homestake chlorine detector," *The Astrophysical Journal* **496** no. 1, (1998) 505. http://stacks.iop.org/0004-637X/496/i=1/a=505.

[21] N. Seiberg, "Naturalness Versus Supersymmetric Non-renormalization Theorems," *Phys. Lett.* **B318** (1993) 469–475, arXiv:hep-ph/9309335.

[22] M. Dine, "The strong CP problem," arXiv:hep-ph/0011376.

[23] C. A. Baker *et al.*, "Improved experimental limit on the electric dipole moment of the neutron," *Phys. Rev. Lett.* **97** (Sep, 2006) 131801. http://link.aps.org/doi/10.1103/PhysRevLett.97.131801.

[24] S. Weinberg, "Implications of dynamical symmetry breaking," *Phys. Rev. D* **13** (Feb, 1976) 974–996. http://link.aps.org/doi/10.1103/PhysRevD.13.974.

[25] S. Weinberg, "Implications of dynamical symmetry breaking: An addendum," *Phys. Rev. D* **19** (Feb, 1979) 1277–1280. http://link.aps.org/doi/10.1103/PhysRevD.19.1277.

[26] L. Susskind, "Dynamics of spontaneous symmetry breaking in the weinberg-salam theory," *Phys. Rev. D* **20** (Nov, 1979) 2619–2625. http://link.aps.org/doi/10.1103/PhysRevD.20.2619.

[27] E. Gildener, "Gauge-symmetry hierarchies," *Phys. Rev. D* **14** (Sep, 1976) 1667–1672. http://link.aps.org/doi/10.1103/PhysRevD.14.1667.

[28] S. Weinberg, "The cosmological constant problem," *Rev. Mod. Phys.* **61** (Jan, 1989) 1–23. http://link.aps.org/doi/10.1103/RevModPhys.61.1.

[29] **WMAP** Collaboration, E. Komatsu *et al.*, "Seven-Year Wilkinson Microwave Anisotropy Probe (WMAP) Observations: Cosmological Interpretation," *Astrophys.J.Suppl.* **192** (2011) 18, arXiv:1001.4538 [astro-ph.CO].

[30] V. Rubakov, "Large and infinite extra dimensions: An Introduction," *Phys.Usp.* **44** (2001) 871–893, arXiv:hep-ph/0104152 [hep-ph].

[31] M. B. Green, J. H. Schwarz, and E. Witten, *Superstring Theory. Vol. 1: Introduction. Vol. 2: Loop Amplitudes, Anomalies & Phenomenology*. WILEY-VCH Verlag, 1988.

[32] M. Kobayashi and T. Maskawa, "CP Violation in the Renormalizable Theory of Weak Interaction," *Prog.Theor.Phys.* **49** (1973) 652–657.

[33] **CDF** Collaboration, "Observation of top quark production in $\overline{p}p$ collisions with the collider detector at fermilab," *Phys. Rev. Lett.* **74** (Apr, 1995) 2626–2631. http://link.aps.org/doi/10.1103/PhysRevLett.74.2626.

[34] **D0** Collaboration, "Search for high mass top quark production in $p\overline{p}$ collisions at $\sqrt{s} =$ 1.8 tev," *Phys. Rev. Lett.* **74** (March, 1995) 2422–2426. http://link.aps.org/doi/10.1103/PhysRevLett.74.2422.

[35] **ATLAS** Collaboration, G. Aad *et al.*, "Measurement of the top quark pair production cross section in pp collisions at sqrt(s) = 7 TeV in dilepton final states with ATLAS," arXiv:1108.3699 [hep-ex].

[36] V. Khachatryan *et al.*, "First measurement of the cross section for top-quark pair production in protonproton collisions at," *Physics Letters B* **695** no. 5, (2011) 424 – 443. http://www.sciencedirect.com/science/article/pii/S037026931001333X.

[37] S. Heinemeyer, W. Hollik, and G. Weiglein, "Electroweak precision observables in the minimal supersymmetric standard model," *Phys.Rept.* **425** (2006) 265–368, arXiv:hep-ph/0412214 [hep-ph].

[38] H. T. Edwards, "The Tevatron Energy Doubler: A Superconducting Accelerator," *Annual Review of Nuclear and Particle Science* **35** (1985) 605–660.

[39] K. Chetyrkin and M. Steinhauser, "The Relation between the MS-bar and the on-shell quark mass at order alpha(s)**3," *Nucl.Phys.* **B573** (2000) 617–651, arXiv:hep-ph/9911434 [hep-ph].

[40] A. H. Hoang *et al.*, "Top-antitop pair production close to threshold: Synopsis of recent NNLO results," *Eur. Phys. J. direct* **C2** (2000) 1, arXiv:hep-ph/0001286.

[41] S. Fleming, A. H. Hoang, S. Mantry, and I. W. Stewart, "Jets from massive unstable particles: Top-mass determination," *Phys.Rev.* **D77** (2008) 074010, arXiv:hep-ph/0703207 [hep-ph].

[42] G. Weiglein, "Electroweak physics at the ILC," *J.Phys.Conf.Ser.* **110** (2008) 042033, arXiv:0711.3003 [hep-ph].

[43] F. Jegerlehner, "Precision measurements of sigma(hadronic) for alpha(eff)(E) at ILC energies and (g-2)(mu)," *Nucl.Phys.Proc.Suppl.* **162** (2006) 22–32, arXiv:hep-ph/0608329 [hep-ph].

[44] http://user.web.cern.ch/public/en/research/LEP-en.html. LEP- Large Electron Positron collider.

[45] http://www.magnet.fsu.edu/. National High Magnetic Field Laboratory.

[46] http://www.fnal.gov/pub/muon_collider/. Muon Collider at Fermilab.

[47] http://mice.iit.edu/. Muon Ionization Cooling Experiment.

[48] A. Caldwell, K. Lotov, A. Pukhov, and F. Simon, "Proton-driven plasma-wakefield acceleration," *Nat Phys.* . http://dx.doi.org/10.1038/nphys1248.

[49] Gianotti, F. for the ATLAS collaboration, "ATLAS Higgs Search." CERN Seminar, December, 2011. https://atlas.web.cern.ch/Atlas/GROUPS/PHYSICS/CONFNOTES/ATLAS-CONF-2011-163/.

[50] Tonelli, G. for the CMS collaboration, "CMS Higgs Search." CERN Seminar, December, 2011. https://cms-docdb.cern.ch/cgi-bin/PublicDocDB/ShowDocument?docid=5709.

[51] "CLIC Conceptual Design Report," 2011. http://lcd.web.cern.ch/LCD/CDR/CDR.html.

[52] R. Brinkmann, (ed.) *et al.*, "TESLA: The superconducting electron positron linear collider with an integrated X-ray laser laboratory. Technical design report. Pt. 2: The accelerator,". DESY-01-011.

[53] **ILC** Collaboration, E. . Brau, James *et al.*, "ILC Reference Design Report Volume 1 - Executive Summary," arXiv:0712.1950 [physics.acc-ph].

[54] The ILD Concept Group, "The International Large Detector: Letter of Intent," arXiv:1006.3396 [hep-ex].

[55] E. Aihara, H., E. Burrows, P., E. Oreglia, M., E. Berger, V. Guarino, *et al.*, "SiD Letter of Intent," `arXiv:0911.0006 [physics.ins-det]`. Letter of Intent for SiD detector concept presented to ILC IDAG.

[56] C. Soldner, "Scintillator Tile Uniformity Studies for a Highly Granular Hadron Calorimeter," 2009. MPP-2009-213.

[57] D. Dannheim and A. Sailer, "Beam-induced Backgrounds in the CLIC Detectors." Lcd-note-2011-021, 2011.

[58] M. A. Thomson, "Particle Flow Calorimetry and the PandoraPFA Algorithm," *Nucl. Instrum. Meth.* **A611** (2009) 25–40, `arXiv:0907.3577 [physics.ins-det]`.

[59] W. R. Leo, *Techniques for nuclear and particle physics experiments: A how to approach*. 2 edition ed., 1994.

[60] R. Wigmans, *Calorimetry Energy Measuremenr in Particle Physics*. Oxford University Press, 2000.

[61] **Particle Data Group** Collaboration, K. Nakamura *et al.*, "Review of particle physics," *J.Phys.G* **G37** (2010) 075021.

[62] Erwin and Hilger, "The zeus uranium-scintillator calorimeter for hera," *Nuclear Instruments and Methods in Physics Research Section A: Accelerators, Spectrometers, Detectors and Associated Equipment* **257** no. 3, (1987) 488 – 498. `http://www.sciencedirect.com/science/article/pii/0168900287909521`.

[63] S. Agostinelli *et al.*, "Geant4 a simulation toolkit," *Nuclear Instruments and Methods in Physics Research Section A: Accelerators, Spectrometers, Detectors and Associated Equipment* **506** no. 3, (2003) 250 – 303. `http://www.sciencedirect.com/science/article/pii/S0168900203013688`.

[64] J. Allison *et al.*, "Geant4 developments and applications," *Nuclear Science, IEEE Transactions on* **53** no. 1, (Feb., 2006) 270 –278.

[65] J. Apostolakis, G. Folger, V. Grichine, A. Howard, V. Ivanchenko, M. Kosov, A. Ribon, V. Uzhinsky, and D. H. Wright, "Geant4 physics lists for hep," in *Nuclear Science Symposium Conference Record, 2008. NSS '08. IEEE*, pp. 833 –836. Oct., 2008.

[66] B. Lutz, *Hadron Showers in a Highly Granular Calorimeter*. PhD thesis, Universität Hamburg, 2010.

[67] G. Bondarenko *et al.*, "Limited Geiger-mode microcell silicon photodiode: New results," *Nucl. Instrum. Meth.* **A442** (2000) 187–192.

[68] N. Feege, "Silicon Photomultipliers: Properties and Application in a Highly Granular Calorimeter.". ISSN 1435-8085.

[69] http://polzope.in2p3.fr:8081/MOKKA/. Mokka homepage.

[70] A. I. Lucaci-Timoce, "Description of the analog hcal prototype in mokka," tech. rep., 2009. www.desy.de/~lucaci/Others/hcalTBeam.pdf.

[71] **CALICE** Collaboration, C. Adloff *et al.*, "Response of the CALICE Si-W Electromagnetic Calorimeter Physics Prototype to Electrons," *J. Phys. Conf. Ser.* **160** (2009) 012065, arXiv:0811.2354 [physics.ins-det].

[72] M. Chadeeva, "Hadron Selection Processor for software compensation study," 2011. Talk on Analysis Meeting .

[73] **CALICE** Collaboration, C. Adloff, J. Blaha, J. Blaising, C. Drancourt, *et al.*, "Electromagnetic response of a highly granular hadronic calorimeter," *JINST* **6** (2011) P04003, arXiv:1012.4343 [physics.ins-det].

[74] I. Marchesini, "Shower Leakage in a Highly Granular Calorimeter." CALICE Analysis note CAN-029, 2011.

[75] K. Seidel and F. Simon, "Initial Study of Hadronic Energy Resolution in the Analog HCAL and the Complete CALICE Setup." CALICE Analysis note CAN-015, 2009.

[76] A. Hoecker, P. Speckmayer, J. Stelzer, J. Therhaag, E. von Toerne, and H. Voss, "TMVA: Toolkit for Multivariate Data Analysis," *PoS* **ACAT** (2007) 040, arXiv:physics/0703039.

[77] V. Andreev, K. Borras, D. Kröcker, I. Melzer-Pellmann, M. Stein, P. Schleper, "Energy Weighting for the Upgrade of the Hadronic Calorimeter of CMS.".

[78] K.-J. Grahn, A. Kiryunin, G. Pospelov and the ATLAS Calorimeter group, "Tests of Local Hadron Calibration Approaches in ATLAS Combined Beam Tests," *Journal of Physics: Conference Series* **293** no. 1, (2011) 012032. http://stacks.iop.org/1742-6596/293/i=1/a=012032.

[79] A. Lenz, U. Nierste, J. Charles, S. Descotes-Genon, A. Jantsch, *et al.*, "Anatomy of New Physics in $B-\bar{B}$ mixing," *Phys.Rev.* **D83** (2011) 036004, arXiv:1008.1593 [hep-ph].

[80] Tevatron Electroweak Working Group and the CDF and D0 Collaborations, "Combination of CDF and DO results on the mass of the top quark using up to 5.8 fb-1 of data," *arXiv:1107.5225* (2011) , arXiv:1107.5255 [hep-ex].

[81] ATLAS Collaboration, "Measurement of the top-quark mass from 2011 atlas data using the template method," *ATLAS-CONF-2011-120* (2011) .

[82] CMS Collaboration, "Measurement of the top quark mass in the l+jets channel," *CMS PAS TOP-10-009* (2011) .

[83] D. Dannheim, "Incoherent pairs and $\gamma\gamma \to$ hadrons at 500 GeV and 3 TeV." Talk at the CLIC Working Group 6 Meeting, 17.05.2011.

[84] A. Munnich and A. Sailer, "The CLIC ILD CDR Geometry for the CDR Monte Carlo Mass Production," *LCD-Note-2011-002* (2011) .

[85] Website: `http://projects.hepforge.org/whizard/`. WHIZARD.

[86] Website: `http://home.thep.lu.se/~torbjorn/Pythia.html`. PYTHIA.

[87] A. Lucaci-Timoce and P. Schade, "Description of the signal and background event mixing as implemented in the Marlin processor OverlayTiming," *LCD-Note-2011-006* (2011) .

[88] The ILD Concept Group, "International Large Detector - Letter of Intent," *DESY 2009/87, Fermilab PUB-09-682-E, KEK Report 2009-6LCD-Note-2011-002* (2010) .

[89] A. Moll, "Top pair production at the ILC," 2008. MPP-2008-161.

[90] M. Cacciari and G. Salam, "Dispelling the N3 myth for the Kt jet-finder," *Phys. Lett.* (2006) . B641 [hep-ph/0512210].

[91] Website: `http://www-pnp.physics.ox.ac.uk/~hillert/VP/LCFIVertex-v00-01/`. LCFI Vertex package.

[92] D. J. Jackson and C. Didcot, "A topological vertex reconstruction algorithm for hadronic jets," *Nucl.Instrum.Meth.* **388** (1997) 24–7.

[93] R. Hawkings, "Vertex detector and flovour tagging studies for the tesla linear collider." LC-PHSM-2000-021-TESLA, 2000.

[94] Website: `http://ilcsoft.desy.de/MarlinReco/current/doc/html/kinfit.html`. MarlinKinFit.

[95] J. Marshall, A. Münnich, and M. A. Thomson, "PFA: Particle Flow Performance at CLIC," *LCD-Note-2011-028* (2011) .

[96] OPAL Collaboration, "Search of the Standard Model Higgs Boson in e^+e^- collisions at $\sqrt{s} = 161$ - 172GeV," *Eur.Phys.Jour.* (1998) . C 1, 425.

[97] J. Marshall, "Current status of PandoraPFA." Talk at the LCWS2011, 2011.

List of Figures

List of Tables